



AD A103887

THE UNIVERSITY OF CHICAGO  
LIBRARY  
540 EAST 57TH STREET  
CHICAGO, ILL. 60637

THE UNIVERSITY OF CHICAGO  
LIBRARY

540 EAST 57TH STREET  
CHICAGO, ILL. 60637

MASSACHUSETTS INSTITUTE OF TECHNOLOGY  
LINCOLN LABORATORY

⑥ SOLID STATE RESEARCH, 1981-1

⑨ QUARTERLY TECHNICAL SUMMARY REPORT

⑪ 15 Feb 81

Accession For	
NTIS GRA&I	<input checked="" type="checkbox"/>
DTIC TAB	<input type="checkbox"/>
Unannounced	<input type="checkbox"/>
Justification	
By _____	
Distribution/	
Availability Codes	
Dist	Avail and/or Special
A	

1 NOV 1980 - 31 JAN 1981

⑫ 80

ISSUED 17 JUNE 1981

⑬ F19628-90-C-0002

⑭ Allen W. McWhorter

Approved for public release; distribution unlimited.

⑮ 496

LEXINGTON

MASSACHUSETTS

AIR FORCE 9 July 1981-600

⑯ ESC

⑰ TR-91-1

DTIC ELECTE  
SEP 8 1981  
S D

207650

D

ME

## ABSTRACT

This report covers in detail the solid state research work of the Solid State Division at Lincoln Laboratory for the period 1 November 1980 through 31 January 1981. The topics covered are Solid State Device Research, Quantum Electronics, Materials Research, Microelectronics, and Analog Device Technology. Funding is primarily provided by the Air Force, with additional support provided by the Army, DARPA, Navy, NASA, and DoE.

## CONTENTS

Abstract	iii
Introduction	vii
Reports on Solid State Research	x
Organization	xvii
I. SOLID STATE DEVICE RESEARCH	1
A. Optical Properties of Proton-Bombarded InP and GaInAsP	1
B. Optical Absorption in HgCdTe	5
C. Chemical Etching of Cleaved Facets of the GaInAsP/InP Double Heterostructure	7
D. Substrate Transfer Technique for LPE Growth	10
II. QUANTUM ELECTRONICS	13
A. Effect of Turbulence-Induced Correlation on LIDAR Measurement Errors	13
B. Ni:MgO Laser: High Average Power and Tuning Properties	15
C. Laser Photochemical Microalloying for Etching of Aluminum Thin Films	18
D. Measurement of Adsorbed Molecular Films by Reflectometry	20
III. MATERIALS RESEARCH	23
A. Lateral Epitaxy by Seeded Solidification for Growth of Single-Crystal Si Films on Insulators	23
B. Heteroepitaxy of Vacuum-Evaporated Ge Films on Single-Crystal Si	26
C. Characterization of Heteroepitaxial $Ge_{1-x}Si_x$ Films Produced by Transient Melting	31
IV. MICROELECTRONICS	35
A. Charge-Coupled Devices: SAW Time-Integrating Correlator with CCD Readout	35
B. Charge-Coupled Devices: Imagers	37
C. Cooled Low-Noise GaAs Monolithic Mixers at 110 GHz	40
D. A Model for the Lateral Epitaxial Overgrowth of Silicon on SiO <sub>2</sub>	41
E. Properties of W-GaAs Schottky Barriers After High-Temperature Anneal	43
F. Shallow PtSi-Si Schottky-Barrier Contacts Formed by a New Technique	48
V. ANALOG DEVICE TECHNOLOGY	53
A. MNOS/CCD Nonvolatile Analog Memory	53
B. High-Performance Elastic Convolver with Parabolic Horns	56

## INTRODUCTION

### I. SOLID STATE DEVICE RESEARCH

The spectral dependence of the optical absorption introduced in InP and GaInAsP by proton bombardment has been measured as a function of dose. The induced absorption, which increases nearly linearly with dose, extends well beyond the band edge and decreases approximately exponentially with wavelength over a broad range. A short 420°C anneal reduces this bombardment-induced absorption by more than a factor of 10.

The optical absorption coefficient corresponding to electronic transitions between the valence and conduction bands in HgCdTe has been measured at photon energies well above the energy gap. Excellent agreement with the Kane theory was found using a matrix element  $P = 7.5 \times 10^{-8}$  eV-cm. At a photon energy  $hc/\lambda$  about 1.2 times the HgCdTe gap energy  $E_g$ , the absorption coefficient is equal to  $3/\lambda$  for  $0.02 < E_g < 0.4$  eV.

A study has been made of the etching technique used to delineate the active GaInAsP layer in GaInAsP/InP double-heterostructure lasers. It was found that careful control of etch solution composition and etch time was necessary to obtain accurate measurement of active layer thickness.

A new method has been demonstrated for the prevention of thermal etching or decomposition of InP substrates prior to liquid-phase-epitaxial (LPE) growth. With this method, the substrate is stored in the growth tube at room temperature during the pregrowth bake and then is transferred to the LPE slider shortly before growth. This method allows both high-purity ( $n \approx 1 \times 10^{15} \text{ cm}^{-3}$ ) and excellent surface morphology to be simultaneously and reproducibly obtained for both InP and GaInAsP LPE-grown layers.

### II. QUANTUM ELECTRONICS

The temporal correlation and measurement error of a dual-laser differential-absorption LIDAR (DIAL) system has been measured and compared with theory. Also, the improvement in measurement accuracy of a dual-laser DIAL compared with a single-laser DIAL system has been determined.

A CW Ni:MgO laser has been operated with up to 10.3 W of  $\text{TEM}_{00}$ -mode output power, and tuning has been demonstrated near 1.31 and 1.38  $\mu\text{m}$  over small-wavelength regions.

A technique has been devised in order to perform the disconnect function in micro-electronic circuits: regions of thin aluminum interconnects are first microalloyed with Zn atoms using a laser photochemical-heating technique, and then the alloyed regions are etched away with a mild acetic acid solution.

In order to characterize thin molecular films adsorbed onto insulators and semiconductors, a reflectometry technique has been developed in which the adsorbent is prepared as a thin, almost antireflecting layer on some appropriate substrate. The large fractional change in reflectivity thus obtainable provides a convenient diagnostic tool for laser photochemical processing.

### III. MATERIALS RESEARCH

A new method, named the LESS technique (lateral epitaxy by seeded solidification), has been used to grow single-crystal Si films over insulating layers on single-crystal Si substrates. After narrow stripes have been opened in the insulating layer to expose the substrate, an amorphous or polycrystalline Si film is deposited over the entire surface, and graphite strip heaters are employed for zone melting the film. By means of this technique, continuous single-crystal Si films have been obtained over SiO<sub>2</sub> layers with stripe openings spaced 50 or 500 μm apart, and single-crystal growth extending as far as 4 mm over Si<sub>3</sub>N<sub>4</sub> has been observed.

A one-step technique has been developed for preparing heteroepitaxial Ge films of good crystal quality by deposition of vacuum-evaporated Ge on heated Si single-crystal substrates. Such Ge films, the best of which were obtained by deposition on <100> Si substrates heated to 550°C, are of interest as potential substrates for the chemical-vapor deposition of GaAs films for shallow-homojunction solar cells.

The crystal quality of heteroepitaxial Ge<sub>1-x</sub>Si<sub>x</sub> films produced by transient heating of Ge-coated Si substrates has been studied by using transmission electron microscopy and <sup>4</sup>He<sup>+</sup> ion channeling. The results obtained by the two techniques, which are in good agreement, reveal a high density of misfit dislocations near the alloy-Si interface, with a much lower density of inclined dislocations propagating up toward the surface.

### IV. MICROELECTRONICS

The performance of a time-integrating correlator in which the multiplication and integration of many samples of two wideband surface-acoustic-wave (SAW) inputs take place in a charge-coupled device (CCD) has been evaluated for the correlation of 20-MHz-bandwidth spread-spectrum signals buried in band-limited Gaussian noise. By using a second CCD chip as an analog delay line to permit cancellation of fixed-pattern noise, a signal-processing gain in excess of 30 dB and a dynamic range of 48 dB have been achieved.

Three focal-plane mosaics consisting of five 100- × 400-element CCD imager chips mounted on a hybrid substrate have been assembled with the positional accuracy required by an advanced moving-target-indicator sensor system used in the GEODSS (Ground-based Electro-Optical Deep Space Surveillance) program.

A GaAs monolithic-integrated-circuit mixer module, which has a double-sideband (DSB) mixer noise temperature of 339 K and a conversion loss of 3.8 dB at 110 GHz when operated at 300 K, has been evaluated at 77 K. The cooled mixer module has a DSB noise temperature of 50 K, the lowest reported for mixers at 110 GHz, and a conversion loss of 4.5 dB.

The lateral growth of single-crystal silicon over the edge of a thin SiO<sub>2</sub> bar structure on a single-crystal silicon substrate using the reduction of silane in hydrogen has been investigated. Lateral-to-vertical growth ratios much greater than 1 have been achieved for appropriate growth conditions. The observed growth phenomena can be explained in terms of the differences of the lateral and vertical partial pressure gradients of the silane gas.

The resistivity of tungsten films deposited on GaAs has been found to decrease with increasing annealing temperature and to reach a minimum value 3.5 times the theoretical lower limit for an annealing temperature of 750°C. For anneals above 750°C, the resistivity increases because of a reaction between tungsten and GaAs. The barrier heights for annealed W-GaAs Schottky barriers are comparable to the barrier heights obtained for Ti-W Schottky barriers on GaAs, and are greater than those for any other metal annealed at these temperatures on GaAs.

Shallow PtSi-Si Schottky-barrier contacts have been formed by heat treatment at 500°C of structures prepared by vacuum deposition of thin alternating Pt and Si layers on n-type (100) Si substrates. This new technique permits the formation of shallow contacts without placing any limitations on the thickness of the PtSi layer. The characteristics of diodes formed by this process are superior to those of conventional diodes formed by heat treatment of structures prepared by depositing a single Pt layer on Si.

## V. ANALOG DEVICE TECHNOLOGY

A hybrid MNOS/CCD circuit has been fabricated which is capable of nonvolatile storage and subsequent nondestructive readout of sampled analog data. A linear dynamic range of 34 dB has been measured 10 min. after writing. After storage times of 100 h, stored signals are attenuated to 60 percent of their initial amplitude but with no loss of linearity. This device provides direct long-term storage of analog data and avoids the need for analog-to-digital conversion and digital memory.

An improved 4-ary elastic convolver has been demonstrated which incorporates a parabolic-horn acoustic beamwidth compressor for high efficiency, a dual-track configuration with orthogonal transducers for self-convolution suppression, and narrow metal-film waveguides for low phase distortion. The time-bandwidth product of this convolver is 930, the self-convolution suppression exceeds 45 dB over the entire passband, and the phase distortion is less than ±35°. This low-cost, compact device can provide programmable matched filtering of minimum-shift-keyed wideband spread-spectrum signals within 0.5 dB of ideal performance.

REPORTS ON SOLID STATE RESEARCH

15 November 1980 through 15 February 1981

PUBLISHED REPORTS

Journal Articles

<u>JA No.</u>			
4972	Liquid-Phase Epitaxy	J. J. Hsieh	Chapter 6 in <u>Handbook on Semiconductors</u> , Vol. 3, edited by S. P. Keller (North-Holland, Amsterdam, 1980), pp. 415-497
5053	Spectral Intensities of the 4- $\mu\text{m}$ $\nu_1 + \nu_3$ Combination Band of $\text{SO}_2$	A. S. Pine M. Dang-Nhu*	J. Mol. Spectrosc. <u>84</u> , 132 (1980)
5076	Formation of the XeBr Exciplex by Xe- $\text{Br}_2(\text{D}')$ Collisions	D. J. Ehrlich R. M. Osgood, Jr.	J. Chem. Phys. <u>73</u> , 3038 (1980)
5083	Laser Microphotochemistry for Use in Solid-State Electronics	D. J. Ehrlich R. M. Osgood, Jr. T. F. Deutsch	IEEE J. Quantum Electron. <u>QE-16</u> , 1233 (1980)
5084	Laser Sources and Detectors for Guided Wave Optical Signal Processing	I. Melngailis	Opt. Eng. <u>19</u> , 941 (1980)
5088	Energy-Dependent Electron-Energy-Loss Spectroscopy: Application to the Surface and Bulk Electronic Structure of MgO	V. E. Henrich* G. Dresselhaus* H. J. Zeiger	Phys. Rev. B <u>22</u> , 4764 (1980)
5120	Avalanche Multiplication and Noise Characteristics of Low-Dark-Current GaInAsP/InP Avalanche Photodetectors	V. Diadiuk S. H. Groves C. E. Hurwitz	Appl. Phys. Lett. <u>37</u> , 807 (1980)
5123	Orientational and Electronic Contributions to the Third-Order Susceptibilities of Cryogenic Liquids	H. Kildal S. R. J. Brueck	J. Chem. Phys. <u>73</u> , 4951 (1980)
5127	Heteroepitaxy of $\text{Ge}_{1-x}\text{Si}_x$ on Si by Transient Heating of Ge-Coated Si Substrates	J. C. C. Fan R. P. Gale F. M. Davis G. H. Foley	Appl. Phys. Lett. <u>37</u> , 1024 (1980)

\* Author not at Lincoln Laboratory.

JA No.

- |      |   |   |   |
|------|---|---|---|
| 5135 | High-Performance Quasi-Optical GaAs Monolithic Mixer at 110 GHz                       | B. J. Clifton<br>G. D. Alley<br>R. A. Murphy<br>I. H. Mroczkowski   | IEEE Trans. Electron Devices <u>ED-28</u> , 155 (1981)  |
| 5136 | Submillimeter Heterodyne Detection of Interstellar Carbon Monoxide at 434 Micrometers | H. R. Fetterman<br>G. A. Koepf*<br>P. F. Goldsmith*<br>B. J. Clifton<br>D. Buhl*<br>N. R. Erickson*<br>D. D. Peck<br>N. McAvoy*<br>P. E. Tannenwald | Science <u>211</u> , 580 (1981)   |
| 5167 | Spectral Characteristics of External-Cavity Controlled Semiconductor Lasers           | M. W. Fleming<br>A. Mooradian   | IEEE J. Quantum Electron. <u>QE-17</u> , 44 (1981)  |
| 5171 | Transferable Single-Crystal Semiconductor Films                                       | C. O. Bozler  | In <u>Physics News in 1980</u> , P. F. Schewe, Ed. (American Institute of Physics, New York, 1980), pp. 39-40 |
| 5178 | Laser Microchemistry: Applications in Semiconductor Processing                        | T. F. Deutsch<br>R. M. Osgood, Jr.<br>D. J. Ehrlich   | In <u>Physics News in 1980</u> , P. F. Schewe, Ed. (American Institute of Physics, New York, 1980), pp. 70-71 |
| 5180 | $\nu_3$ Vibrational Ladder of SF <sub>6</sub>   | C. W. Patterson*<br>B. J. Krohn*<br>A. S. Pine  | Opt. Lett. <u>6</u> , 39 (1981)   |

\* \* \* \* \*

UNPUBLISHED REPORTS

Journal Articles

JA No.

- |      |   |  |                            |
|------|---|--|----------------------------|
| 5145 | Laser Induced Dielectric Breakdown in Cryogenic Liquids   | S. R. J. Brueck<br>H. Kildal   | Accepted by J. Appl. Phys. |
| 5154 | Thermal Expansion of NdP <sub>5</sub> O <sub>14</sub>   | W. E. Barch<br>S. R. Chinn<br>W. K. Zwicker*                         | Accepted by J. Appl. Phys. |
| 5156 | High Resolution Double Resonance Spectroscopy of $2\nu_3 \leftarrow \nu_3$ Transitions in SF <sub>6</sub> | C. W. Patterson*<br>R. S. McDowell*<br>P. F. Moulton<br>A. Mooradian | Accepted by Opt. Lett.     |

---

\* Author not at Lincoln Laboratory.

JA No.

5159	Detection of the $J = 6 \rightarrow 5$ Transition of Carbon Monoxide	P. F. Goldsmith* N. R. Erickson* H. R. Fetterman B. J. Clifton D. D. Peck P. E. Tannenwald G. A. Koepf* D. Buhl* N. McAvoy*	Accepted by <i>Astrophys. J.</i>
5160	Transmission Electron Microscopy and Ion Channeling Studies of Heteroepitaxial $\text{Ge}_{1-x}\text{Si}_x$ Films Produced by Transient Heating	B-Y. Tsaur J. C. C. Fan T. T. Sheng*	Accepted by <i>Appl. Phys. Lett.</i>
5164	Lateral Epitaxy by Seeded Solidification for Growth of Single-Crystal Si Films on Insulators	J. C. C. Fan M. W. Geis B-Y. Tsaur	Accepted by <i>Appl. Phys. Lett.</i>
5165	UV Photolysis of Van der Waals Molecular Films	D. J. Ehrlich R. M. Osgood, Jr.	Accepted by <i>Chem. Phys. Lett.</i>
5168	Anodic Dissolution Technique for Preparing Large Area GaAs Samples for Transmission Electron Microscopy	J. P. Salerno J. C. C. Fan R. P. Gale	Accepted by <i>J. Electrochem. Soc.</i>
5170	Solid-Phase Heteroepitaxy of Ge on $\langle 100 \rangle$ Si	B-Y. Tsaur J. C. C. Fan R. P. Gale	Accepted by <i>Appl. Phys. Lett.</i>
5173	Intracavity Loss Modulation of GaInAsP Diode Lasers	D. Z. Tsang J. N. Walpole S. H. Groves J. J. Hsieh J. P. Donnelly	Accepted by <i>Appl. Phys. Lett.</i>
5177	Laser Photochemical Microalloying for Etching of Aluminum Thin Films	D. J. Ehrlich R. M. Osgood, Jr. T. F. Deutsch	Accepted by <i>Appl. Phys. Lett.</i>
5179	Explosive Crystallization of Amorphous Germanium	H. J. Leamy* W. L. Brown* G. K. Celler* G. Foti* G. H. Gilmer* J. C. C. Fan	Accepted by <i>Appl. Phys. Lett.</i>
5191	Fundamental Line Broadening of Single Mode (GaAl)As Diode Lasers	M. W. Fleming A. Mooradian	Accepted by <i>Appl. Phys. Lett.</i>
5192	On the Use of $\text{AsH}_3$ in the MBE Growth of GaAs	A. R. Calawa	Accepted by <i>Appl. Phys. Lett.</i>

\* Author not at Lincoln Laboratory.

JA No.

5201 Low Loss GaAs Optical Waveguides Formed by Lateral Epitaxial Growth over Oxide  
 F. J. Leonberger  
 C. O. Bozler  
 R. W. McClelland  
 I. Melngailis

Accepted by Appl. Phys. Lett.

Meeting Speeches\*

MS No.

4779D Beam Annealing of Ion-Implanted GaAs and InP  
 J. C. C. Fan  
 R. L. Chapman  
 J. P. Donnelly  
 G. W. Turner  
 C. O. Bozler

5427 Optical Measurement of Phase Boundary Dynamics During Laser Crystallization of Amorphous Ge Films  
 R. L. Chapman  
 J. C. C. Fan  
 H. J. Zeiger  
 R. P. Gale

5428 TEM Investigation of the Microstructure in Laser-Crystallized Ge Films  
 R. P. Gale  
 J. C. C. Fan  
 R. L. Chapman  
 H. J. Zeiger

5429 Scanning Cathodoluminescence Microscopy of Grain Boundaries in GaAs  
 J. P. Salerno  
 R. P. Gale  
 J. C. C. Fan  
 J. Vaughan†

5461 Origins of High Spatial Resolution in Photochemical, Direct-Write Laser Processing  
 D. J. Ehrlich  
 T. F. Deutsch  
 R. M. Osgood, Jr.

5538A Lateral Epitaxy by Seeded Solidification for Growth of Single-Crystal Si Films on Insulators  
 J. C. C. Fan  
 M. W. Geis  
 B-Y. Tsaur

5596 Explosive Crystallization of Amorphous Germanium Films  
 H. J. Leamy†  
 W. L. Brown†  
 G. K. Celler†  
 G. Foti†  
 G. H. Gilmer†  
 J. C. C. Fan

5127B Recent Advances in High-Efficiency Low-Cost GaAs Solar Cells  
 J. C. C. Fan  
 C. O. Bozler  
 R. P. Gale  
 R. W. McClelland  
 R. L. Chapman  
 G. W. Turner

5538 Lateral Epitaxy by Seeded Solidification for Growth of Single-Crystal Si Films on Insulators  
 J. C. C. Fan  
 M. W. Geis  
 B-Y. Tsaur

Materials Research Society  
 Mtg., Boston, 16-21 November 1980

IEEE Intl. Electron Devices  
 Mtg., Washington, DC,  
 8-10 December 1980

\* Titles of Meeting Speeches are listed for information only. No copies are available for distribution.

† Author not at Lincoln Laboratory.

<u>MS No.</u>			
5145A	The Permeable Base Transistor	C. O. Bozler	Seminar, University of Illinois, Champaign/Urbana, 6 November 1980
5152B	Laser Induced Photochemical Reactions for Electronic Device Fabrication	D. J. Ehrlich T. F. Deutsch R. M. Osgood, Jr.	Seminar, M.I.T., 10 February 1981
5232A	Tunable Solid-State Ultraviolet Lasers	D. J. Ehrlich P. F. Moulton R. M. Osgood, Jr.	} LASERS '80, New Orleans, Louisiana, 15-19 December 1980
5379A	Resonance-Line Lasers and Their Applications	R. M. Osgood, Jr. D. J. Ehrlich T. F. Deutsch G. C. Turk* J. E. Travis*	
5477	Tunable Transition-Metal Lasers	P. F. Moulton A. Mooradian	
5264C	Recent Advances in Tunable Lasers	A. Mooradian	Seminar, Goddard Space Flight Center, Greenbelt, Maryland, 26 January 1981
5354	A TDI CCD Hybrid Sensor Mosaic for Satellite Surveillance	B. E. Burke W. H. McGonagle R. W. Mountain D. J. Silversmith	} GOMAC '80, Houston, Texas, 19-21 November 1980
5355	A High Speed Digitally Programmable CCD Transversal Filter	A. M. Chiang B. E. Burke	
5411A	Applications of Microstructures in Physics and Chemistry	D. C. Flanders	Microstructures Seminar, State University of New York, Albany, 2 December 1980
5433	Electromagnetic Long-Line Effects in SAW Convolver	E. L. Adler	} 1980 Ultrasonics Symposium, Boston, 3-7 November 1980
5434	The Effect of Acoustic Dispersion and Attenuation on SAW Convolver Performance	E. L. Adler J. H. Cafarella	
5435	Attenuating Thin Films for SAW Devices	A. C. Anderson V. S. Dolat	
5436	Self-Aligning SAW Chirp-Fourier-Transform System	D. R. Arsenault V. S. Dolat	

\* Author not at Lincoln Laboratory.

MS No.

5437	LiNbO <sub>3</sub> -Surface-Acoustic-Wave-Edge-Bonded Transducers on ST Quartz and <001> -Cut GaAs	D. E. Oates R. A. Becker	
5438	Temperature-Stable RAC	D. E. Oates D. M. Boroson	
5439	An Acoustoelectric Burst-Waveform Processor	S. A. Reible I. Yao	
5440	Nonlinear Coupled-Mode Interactions of Surface Acoustic Waves	N. P. Vlannes A. Bers	1980 Ultrasonics Symposium, Boston, 3-7 November 1980
5441	High Performance Elastic Convolver with Parabolic Horns	I. Yao	
5448	Hybrid Convolver/Binary Signal Processor Achieves High Processing Gain	R. P. Baker J. H. Cafarella	
5449	The Impact of Convolver Characteristics on System Performance	E. Stern	
5489	A Closed-Form Analysis of Reflective-Array Gratings	P. V. Wright H. A. Haus*	
5457	Recent Experimental Results on Permeable Base Transistors	G. D. Alley C. O. Bozler D. C. Flanders R. A. Murphy W. T. Lindley	IEDM '80, Washington, DC, 8-10 December 1980
5498B	On the MBE Growth of High Purity GaAs	A. R. Calawa	American Vacuum Society Mtg., Waltham, Massachu- setts, 14 January 1981
5529	High-Speed Electrooptical Signal Processing Devices	F. J. Leonberger	Boston Section IEEE Chapter on Quantum Electronics, GTE, Waltham, Massachu- setts, 18 November 1980
5538B, C, D, E	Preparation of Thin Single-Crystal Films on Insulators	J. C. C. Fan	Xerox Corporation Colloq., Webster, New York, 20 Jan- uary 1981; Seminar, Stan- ford University, California, 9 February 1981; Seminar, University of California, Berkeley, 11 February 1981; Seminar, University of Cal- ifornia, Los Angeles, 13 February 1981
5551	Optical Techniques for Signal Processing	R. C. Williamson	Electrooptics/Laser '80, Boston, 19 November 1980

\* Author not at Lincoln Laboratory.

MS No.

- |            |  |                               |   |
|------------|--|-------------------------------|---|
| 5556       | Surface-Acoustic-Wave Signal-Processing Devices                | R. W. Ralston                 | Seminar on Solid-State Physics, Yale University, 16 January 1981  |
| 5557, A, B | Transition-Metal Ion in Tunable Lasers                         | P. F. Moulton<br>A. Mooradian | Topical Meeting on Infrared Lasers, Los Angeles, California, 4 December 1980; Seminar, IBM, San Jose, California, 5 December 1980; Seminar, Purdue University, 8 December 1980  |
| 5558       | Electron Beam Testing and Restructuring of Integrated Circuits | D. C. Shaver                  | Second Caltech Conf. on VLSI, Pasadena, California, 19-21 January 1981  |
| 5576       | Surface-Acoustic-Wave Signal Processing in a Digital Age       | R. C. Williamson              | University of Maine, Orono, 18 November 1980; John Carroll University, Cleveland, Ohio, 9 December 1980; Penn. State University and Central Pennsylvania IEEE, State College, 10 December 1980; Washington Section IEEE, Washington, DC, 21 January 1981; Los Angeles Section IEEE, Irvine, California, 27 January 1981 |

## ORGANIZATION

### SOLID STATE DIVISION

A. L. McWhorter, *Head*  
I. Melngailis, *Associate Head*  
J. F. Goodwin, *Assistant*

R. H. Rediker, *Senior Staff*  
P. E. Tannenwald, *Senior Staff*

### QUANTUM ELECTRONICS

A. Mooradian, *Leader*  
P. L. Kelley, *Associate Leader*

Barch, W. E.	Fetterman, H. R.
Belanger, L. J.	Goodhue, W. D.*
Blumberg, W. A. M.	Hancock, R. C.
Brueck, S. R. J.	Killinger, D.
Burke, J. W.	Menyuk, N.
Bushee, J. F.	Moulton, P. F.
Clahasy, C.*	Osgood, R. M.
Coulombe, M. J.	Parker, C. D.
Daneu, V.	Peck, D. D.
DeFeo, W. E.	Pine, A. S.
Deutsch, T. F.	Sullivan, D. J.
Ehrlich, D. J.	Welford, D.
Feldman, B.	

### ELECTRONIC MATERIALS

A. J. Strauss, *Leader*  
J. C. C. Fan, *Assistant Leader*  
J. G. Mavroides, *Senior Staff*  
H. J. Zeiger, *Senior Staff*

Anderson, C. H., Jr.	Krohn, L., Jr.
Button, M. J.	Mastromattei, E. L.
Chapman, R. L.	Nitishin, P. M.
Davis, F. M.	Owens, E. B.
Delaney, E. J.	Palm, B. J.
Fahey, R. E.	Pantano, J. V.
Finn, M. C.	Salerno, J. P.*
Foley, G. H.	Tracy, D. M.
Gale, R. P.	Tsaur, B-Y.
Iseler, G. W.	Turner, G. W.
Kolesar, D. E.	Vohl, P.

### APPLIED PHYSICS

R. C. Williamson, *Leader*  
C. E. Hurwitz, *Associate Leader*  
T. C. Harman, *Senior Staff*  
R. H. Kingston, *Senior Staff*

Armiento, C. A.*	Lattes, A.*
Galawa, A. R.	Leonberger, F. J.
Carter, F. B.	Liau, Z. L.
DeMeo, N. L.	Lind, T. A.
Diadiuk, V.	McBride, W. F.
Donnelly, J. P.	Paladino, A. E.
Ferrante, G. A.	Plonko, M. C.
Foyt, A. G.	Spears, D. L.
Groves, S. H.	Tsang, D. Z.*
Hovey, D. L.	Walpole, J. N.

### ANALOG DEVICE TECHNOLOGY

E. Stern, *Leader*  
J. H. Cafarella, *Assistant Leader*  
R. W. Ralston, *Assistant Leader*

Anderson, A. C.	Kernan, W. C.
Arsenault, D. R.	Leung, I.
Baker, R. P.	Lowney, S. D.
Becker, R. A.	Lynch, J. T.
Behrmann, G. J.	Oates, D. E.
Brogan, W. T.	Reible, S. A.
Dolat, V. S.	Slattery, R. L.
Fischer, J. H.	Withers, R. S.
Flynn, G. T.	Yao, I.
Holtham, J. H.	

### MICROELECTRONICS

W. T. Lindley, *Leader*  
F. J. Bachner, *Associate Leader*  
R. A. Murphy, *Assistant Leader*

Alley, G. D.	Felton, B. J.	Melngailis, J.†
Bozler, C. O.	Flanders, D. C.	Mountain, R. W.
Burke, B. E.	Geis, M. W.	Nichols, K. H.
Cabral, S. M.	Goeloe, G. T.*	Piacentini, W. J.
Chiang, A. M.	Gray, R. V.	Piehler, B. H.
Chu, A.	Hansell, G. L.*	Rabe, S.
Clifton, B. J.	Hawryluk, A. M.*	Rathman, D. D.
Daniels, P. J.	Lincoln, G. A., Jr.	Shaver, D. C.‡
DeGraff, P. D.	Lyszczarz, T. M.	Silversmith, D. J.
Durant, G. L.	Macropoulos, W.	Smythe, D. L.
Economou, N. P.	Mahoney, L. J.	Vigilante, J. L.
Efremow, N.	McClelland, R. W.	Wilde, R. E.
Elta, M. E.	McGonagle, W. H.	

\* Research Assistant

† Part Time

‡ Staff Associate

## I. SOLID STATE DEVICE RESEARCH

### A. OPTICAL PROPERTIES OF PROTON-BOMBARDED InP AND GaInAsP

Proton bombardment has been used to modify the electrical and optical properties of GaAs in many types of electrooptical and microwave devices.<sup>1</sup> In general, bombardment is used to create high-resistivity layers in both n- and p-type GaAs; however, the bombardment also induces an increase in optical absorption near the GaAs band edge,<sup>2,3</sup> an effect which may be detrimental for some electrooptical devices, particularly lasers. For many applications, a post-bombardment anneal can be used to achieve a compromise between resistivity and optical attenuation.<sup>2,3</sup>

The effects of proton bombardment in InP (Ref. 4) differ somewhat from those in GaAs. Very high resistivity is obtained only in p-type material and only for a narrow range of proton dose, the magnitude of which scales with the initial concentration in the InP. For sufficiently large doses, both n- and p-type InP become only moderately high resistivity n-type material. Nevertheless, proton bombardment in InP can be used effectively for some applications, including the production of current-confining regions in stripe-geometry GaInAsP/InP diode lasers.<sup>5</sup>

In order to optimize the design of these lasers, as well as to effectively utilize bombardment in other InP-based electrooptical devices, it is desirable to know more about the optical properties of proton-bombarded layers. We report here a study of the spectral and dose dependence of the proton-induced optical attenuation in both InP and GaInAsP ( $\lambda_g \sim 1.1 \mu\text{m}$ ), and describe the effect of an anneal at moderate temperature which strongly reduces the induced attenuation. The results of these measurements are qualitatively consistent with those for GaAs.

The wafer used for these measurements consisted of a p-type InP substrate with an n-type InP buffer layer and an n-type GaInAsP layer, both grown by liquid phase epitaxy (LPE). The substrate was Cd-doped and had a hole concentration of about  $10^{17} \text{ cm}^{-3}$ . The 5- $\mu\text{m}$ -thick buffer layer, which was not intentionally doped, had an electron concentration of about  $10^{17} \text{ cm}^{-3}$ , as did the quaternary layer, which had a composition of  $\text{Ga}_{0.17}\text{In}_{0.83}\text{As}_{0.4}\text{P}_{0.6}$  ( $\lambda_g \sim 1.1 \mu\text{m}$ ) and a thickness of 3.5  $\mu\text{m}$ . The back surface of the wafer was polished and the wafer was then cut in half. The GaInAsP epitaxial layer was chemically removed from one of the halves both to permit measurement of the InP absorption and to serve as a reference transmission to deduce the GaInAsP absorption.

For the proton bombardment and the optical transmission measurements, the two samples were mounted over holes on a common mounting plate. The samples were bombarded with a multiple-energy dose of protons to obtain nearly uniform damage throughout a 3- $\mu\text{m}$ -thick bombarded layer.<sup>4</sup> A room-temperature bombardment schedule of  $N$  protons/ $\text{cm}^2$  at 300 keV, 0.5  $N$  at 200 keV, and 0.33  $N$  at 100 keV was used for several values of  $N$  in the range  $3 \times 10^{13} \text{ cm}^{-2} \leq N \leq 3 \times 10^{15} \text{ cm}^{-2}$ . After each bombardment (i.e., change in  $N$ ), the transmission of the samples was measured in a commercial dual-beam spectrophotometer over the wavelength range 0.8 to 2.4  $\mu\text{m}$ . The absolute transmission was determined in each case by a preliminary 100-percent transmission determination utilizing two additional mounting plates, each with holes identical to the ones in the plate on which the samples were mounted. One of these plates was left in the reference channel for the sample measurement. The accuracy of the transmission measurements with this technique is believed to be  $\pm 1$  percent.

The attenuation coefficients  $\alpha_1$  and  $\alpha_2$  of the InP and the quaternary layer, respectively, prior to bombardment were calculated from standard expressions for optical transmission. For

these calculations, values for the reflectivity of the materials as a function of wavelength were calculated from the values of refraction index reported in the literature,<sup>6,7</sup> and the small reflection at the InP/GaInAsP interface was neglected. The band-edge attenuation vs wavelength for unbombarded InP and GaInAsP is shown in Fig. I-1(a) and I-1(b), respectively. In Fig. I-1(a), additional data from the review paper by Seraphin and Bennett<sup>6</sup> are shown for comparison. Our

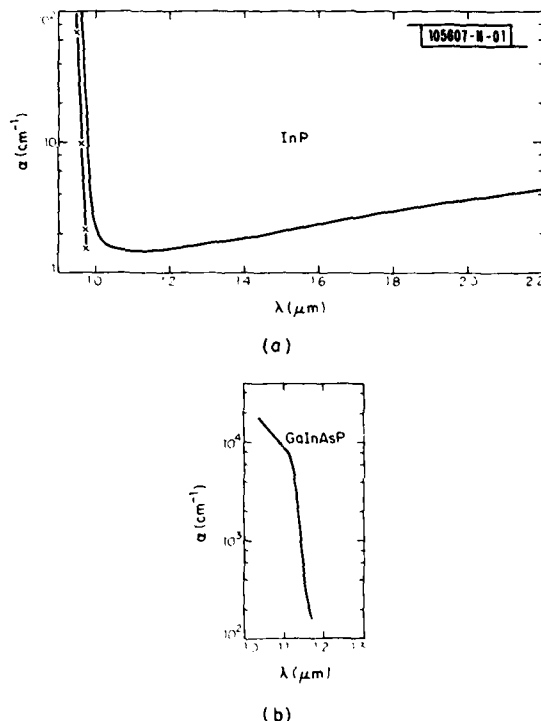


Fig. I-1. Measured absorption vs wavelength for unbombarded (a) InP and (b)  $\text{Ga}_{0.17}\text{In}_{0.83}\text{As}_{0.4}\text{P}_{0.6}$ . The data denoted by "X" in (a) are taken from Ref. 6.

absorption edge is shifted to a longer wavelength than theirs by approximately  $130 \text{ \AA}$ . The reasons for this discrepancy are not completely understood, although possible differences in sample temperature could account for most of the difference. In our case, the sample was heated to about  $30^\circ\text{C}$  above room temperature because, in the spectrometer used, all the spectral components of the source light were continuously incident on the sample. The small ( $\alpha < 2 \text{ cm}^{-1}$ ) attenuation in the 1- to 1.3- $\mu\text{m}$  range is characteristic of low-concentration p-type InP (Ref. 8).

For the quaternary data, it is interesting to note the change in slope of  $\alpha$  vs  $\lambda$  at  $\lambda \approx 1.11 \mu\text{m}$ . A similar effect occurs in InP near the bandgap ( $\lambda_g = 0.92 \mu\text{m}$ ) (Ref. 6) and in other II-V compounds,<sup>9</sup> and it seems reasonable to conclude that the bandgap of this quaternary is about  $1.11 \mu\text{m}$ . This contrasts with a value of  $1.14 \mu\text{m}$  deduced by taking the bandgap to be the point where the transmission drops to 50 percent of  $T_{\text{max}}$ , which is another common method of determining the bandgap.

After proton bombardment, we must add to the attenuation exponents in the conventional transmission expressions a term  $\int \Delta\alpha(x)dx \sim \Delta\alpha L$ , where  $L \sim 3 \mu\text{m}$ , the damage depth, and

$\Delta\alpha$  is the average damage-induced attenuation coefficient. [ $\Delta\alpha(x)$  should be approximately constant with depth for our case of a nearly uniform damage profile.] Using the prebombardment values of  $\alpha_1$  and  $\alpha_2$  and the post-bombardment transmission, we can then solve for  $\Delta\alpha L$ , assuming the change in reflectivity due to the bombardment is negligible. It should be noted (see Fig. I-1) that values of  $\alpha$  up to a factor of 100 times higher can be measured for the thin GaInAsP layer than for the InP sample.

The spectral dependence of  $\Delta\alpha L$  for InP and GaInAsP is shown in Fig. I-2(a) and (b), respectively, with the normalized proton dose as parameter. The reduction of the data to obtain these

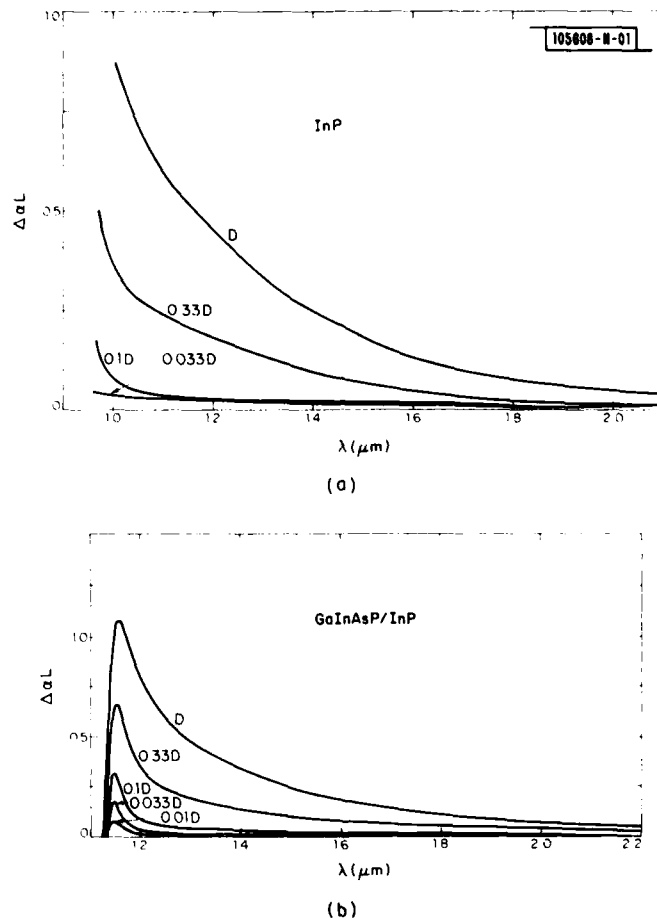


Fig. I-2. Measured bombardment-induced attenuation exponent  $\Delta\alpha L$  vs wavelength with total proton dose as parameter for (a) InP and (b)  $\text{Ga}_{0.17}\text{In}_{0.83}\text{As}_{0.4}\text{P}_{0.6}$ . The curves are labelled with respect to a reference dose  $D$ , defined in the text for each case.

curves was computer assisted. The proton doses were normalized to  $D$ , which is the total dose using the implant schedule discussed above with  $N = 3 \times 10^{15} \text{ cm}^{-2}$ . As shown in Fig. I-2(a), there is substantial attenuation at  $\lambda = 1.3 \mu\text{m}$ , a common lasing wavelength, for doses greater than  $0.33 D$ . The minimum resolvable change in attenuation for InP,  $\Delta\alpha L \sim 2 \times 10^{-2}$ , corresponds to an  $\sim 1$ -percent change in transmission, the instrument accuracy, out of  $\sim 50$  percent

total transmission. This degree of uncertainty could account for possible errors in the tails of the 0.1 D and 0.033 D curves.

The data for GaInAsP [Fig. I-2(b)] show similar behavior to those for InP, with induced attenuation extending well beyond the band edge and with values of  $\Delta\alpha \sim 3 \times 10^3 \text{ cm}^{-1}$  near the band gap. An interesting aspect is the maximum in  $\Delta\alpha L$  at a wavelength of  $\sim 1.15 \mu\text{m}$ . If the curve were continued to short enough wavelengths, the values of  $\Delta\alpha L$  would go negative at the band gap due to a decrease in the absorption coefficient above the band edge. These data are not plotted here due to the scatter in the results between the various bombardments. However, the effect is consistent with that seen experimentally and theoretically for other induced band-edge absorption mechanisms such as electroabsorption<sup>10</sup> (Franz-Keldysh effect). This dramatic wavelength variation in induced absorption is not measurable on the InP samples, or in previously reported GaAs studies, because the large band-edge absorption of the relatively thick substrates totally masks the changes.

The bombardment-induced absorption is replotted on a semi-log scale in Fig. I-3(a) and -3(b) for the InP and the GaInAsP samples, respectively. These curves show more clearly that the

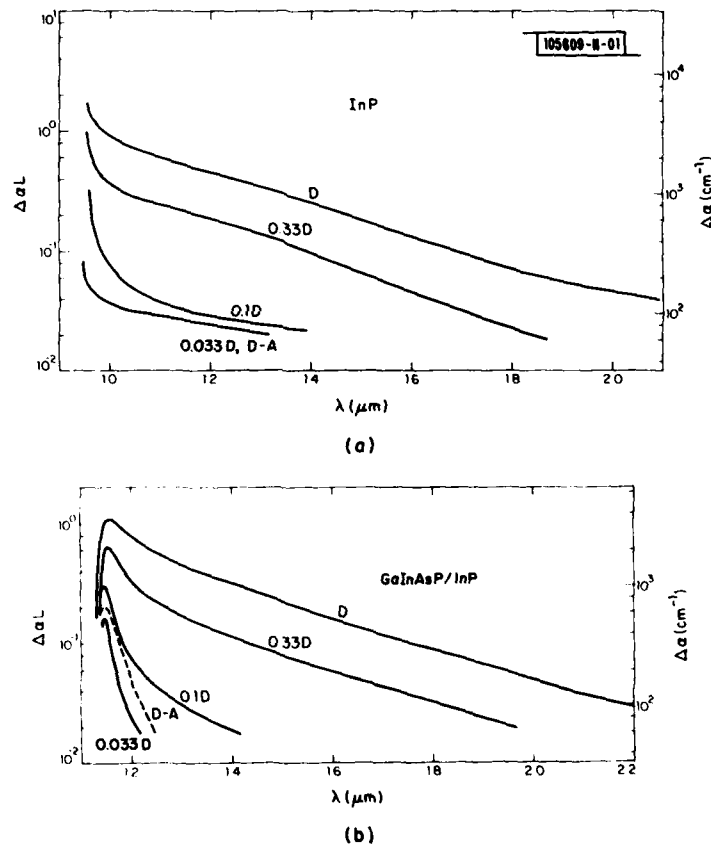


Fig. I-3. Semi-log plot of measured bombardment-induced attenuation exponent  $\Delta\alpha L$  and uniform attenuation coefficient  $\Delta\alpha$  vs wavelength with proton dose as parameter for (a) InP and (b)  $\text{Ga}_{0.17}\text{In}_{0.83}\text{As}_{0.4}\text{P}_{0.6}$ . The reference dose D is defined in the text. Also shown in each case is a curve "D-A" indicating attenuation following bombardment of dose D and a 5-min.  $420^\circ\text{C}$  anneal described in the text.

induced attenuation is exponentially dependent on wavelength. At doses of D and 0.33 D, one can model the attenuation as  $\Delta\alpha \sim e^{-A\lambda}$  with  $A = 3.1 \mu\text{m}^{-1}$  at wavelengths  $\lambda > \lambda_g + 0.2 \mu\text{m}$  for both materials. An approximately linear dose dependence is also evident for wavelengths within  $\sim 0.1 \mu\text{m}$  of the band gap for both cases. For longer wavelengths, it is difficult to scale values of  $\Delta\alpha L$  for doses from 0.1 and 0.33 D due to the limited measurement accuracy. However, between the doses of D and 0.33 D, the change in  $\Delta\alpha L$  is about a factor of 3 over a broad wavelength range.

The effect of a modest anneal on reducing  $\Delta\alpha$  is shown in Fig. 1-3(a) and (b) by the curve labelled "D-A." This corresponds to annealing the sample bombarded with total dose D at 420°C for 5 min. in a  $\text{H}_2$  atmosphere. As can be seen, the attenuation is reduced by more than a factor of 10, to a level for the InP sample comparable to a bombardment of 0.033 D and for the GaInAsP sample comparable to a dose of approximately 0.05 D. This anneal corresponds to the heat treatment typically used for alloying ohmic contacts in our fabrication of proton-defined stripe-geometry lasers.<sup>5</sup> It is therefore significant that this heat treatment greatly reduces  $\Delta\alpha$  in the InP at a typical quaternary laser wavelength of 1.3  $\mu\text{m}$ . These results suggest that one should be able to optimize the proton dose and anneal of GaInAsP diode lasers to maintain current confinement and minimize optical attenuation as has been done in GaAs.<sup>2</sup>

A comparison of the data for  $\Delta\alpha$  vs dose and wavelength obtained in this work with that for GaAs<sup>2,3</sup> indicates qualitative agreement. It is difficult to compare exactly the amount of proton-induced absorption at a given dose in the two materials because only single-energy protons were used in the GaAs work. Nevertheless, it appears that the attenuating exponent  $\Delta\alpha L$  in InP and in the quaternary alloy is  $\sim 60$  percent of the corresponding value in GaAs. We have also found that GaAs tends to exhibit an exponential wavelength dependence  $\Delta\alpha \sim e^{A\lambda}$ , but with  $A = 2.2 \mu\text{m}^{-1}$  (Ref. 11).

F. J. Leonberger      Z. L. Liao  
 J. N. Walpole        G. W. Iseler  
 J. P. Donnelly

## B. OPTICAL ABSORPTION IN HgCdTe

The optical absorption coefficient corresponding to electronic transitions between the valence and conduction band in narrow-energy-gap HgCdTe has been measured at photon energies well above the energy gap. This represents the first accurate measurements of this material parameter, which is very important in the design of HgCdTe infrared detectors. Excellent agreement with the Kane theory was found using a matrix element  $P = 7.5 \times 10^{-8} \text{ eV}\cdot\text{cm}$ , which is 20% smaller than previously used by Blue.<sup>12</sup> At a wavelength  $\lambda$  corresponding to a photon energy about 1.2 times the HgCdTe gap energy  $E_g$ , the absorption coefficient  $\alpha$  is equal to  $3/\lambda$  for  $0.02 \text{ eV} < E_g < 0.4 \text{ eV}$ .

The measurements were carried out on ultrathin foils of single-crystal HgCdTe prepared by carefully lapping and chemical-mechanical polishing each surface with a bromine-methanol solution in a manner similar to the techniques used in commercial HgCdTe photoconductor fabrication. The 3- x 5-mm foils were floated off the polishing fixture onto a gold-coated sapphire platelet with a 1-mm-dia. hole drilled through the center and were held down with vacuum grease. The sapphire platelets were attached to the cold finger of a closed-cycle cooler, and transmission measurements were carried out over the 3- to 36- $\mu\text{m}$  spectral region using a CsBr prism monochromator and a Ge:Zn detector. The optical flux from the monochromator was less than  $0.1 \text{ mW}/\text{cm}^2$ , considerably below the 300 K background level. After the measurements were

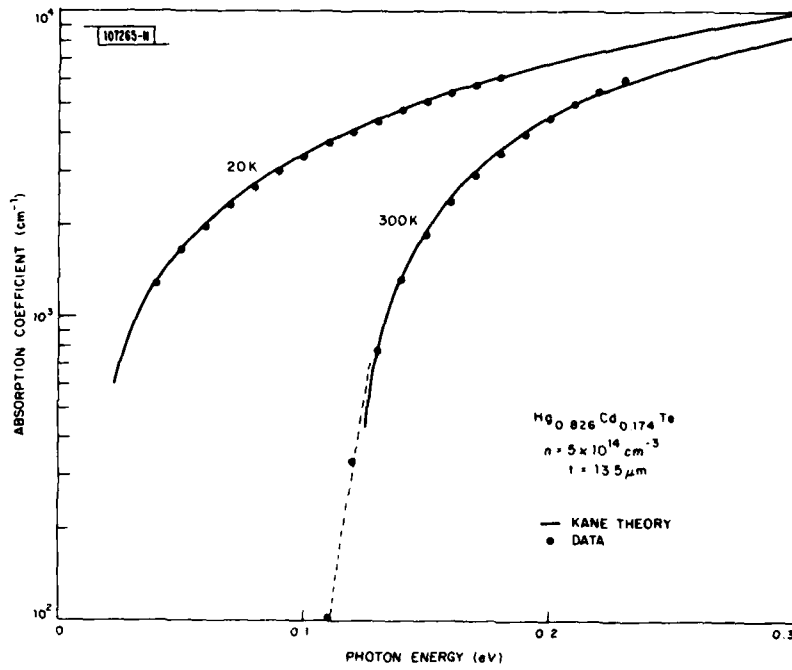


Fig. I-4. Optical absorption coefficient as a function of photon energy for  $\text{Hg}_{0.826}\text{Cd}_{0.174}\text{Te}$  at 300 and 20 K.

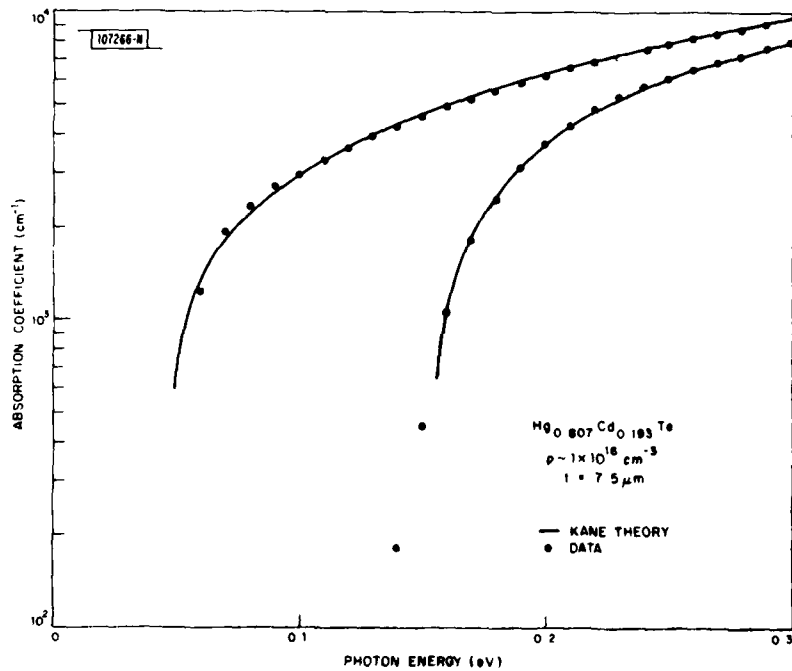


Fig. I-5. Optical absorption coefficient as a function of photon energy for  $\text{Hg}_{0.807}\text{Cd}_{0.193}\text{Te}$  at 300 and 20 K.

completed at various temperatures from 15 to 300 K, the foils were broken in order to determine their thickness, which ranged from 4 to 25  $\mu\text{m}$ .

Interference effects were quite evident near the transmission edge, indicating a relatively uniform foil thickness  $t$  over the 1-mm-dia. area. A curve drawn through the center of gravity of the oscillations in a transmission vs photon energy plot was used to compensate for the effects of interference. Over the region of primary interest,  $\alpha t > 1$  (i.e.,  $\alpha > 1000 \text{ cm}^{-1}$ ), these oscillations were weak and insignificant. The small volume of material probed in the measurement insured a relatively uniform alloy composition, estimated to be better than  $\pm 0.1\%$  CdTe.

In Figs. I-4 and I-5 are shown the absorption coefficient as a function of photon energy at 300 and 20 K for HgCdTe samples with alloy compositions of 17.4 and 19.3 mole % CdTe, respectively. The alloy composition was determined by the photon energy at which  $\alpha = 1000 \text{ cm}^{-1}$  at 300 K, as defined by Finkman and Nemirovsky.<sup>13</sup> The solid curves in Figs. I-4 and I-5 were calculated from the absorption coefficient expressions given by Blue<sup>12</sup> for the light-hole- and heavy-hole-to-conduction-band transitions, which are based upon the Kane theory and are valid in the limit of very small electron effective mass. The temperature dependence of  $E_g$  was calculated from Reference 13 and is in excellent agreement with our data. The dashed curve in Fig. I-4 is the exponential variation previously reported<sup>13</sup> for  $20 \text{ cm}^{-1} < \alpha < 1000 \text{ cm}^{-1}$ . This exponential absorption edge tail is temperature dependent and presumably due to phonon effects, which are not accounted for in the Kane theory. Above  $1000 \text{ cm}^{-1}$  this exponential behavior no longer holds, and our data show excellent agreement with the Kane theory. Bandfilling has been taken into account in all of the calculated curves and significantly improves the fit to the data both at 300 and 20 K. Absorption coefficients were measured on eight different samples (both n- and p-type) with alloy compositions between 17.4 and 20 mole % CdTe from four HgCdTe ingots, and all values of  $\alpha$  for  $1.2 E_g < h\nu < 0.3 \text{ eV}$  were in agreement with the Kane theory using a matrix element  $P = 7.5 \times 10^{-8} \text{ eV-cm}$ . This represents the first clear evidence of the accuracy of the Kane theory in describing the absorption in narrow-gap HgCdTe.

There are two implications with regard to detector performance that result from this absorption data. First, the relatively slow rise in absorption coefficient above the edge coupled with the strong dependence of lifetime (and minority electron diffusion length) with hole concentration<sup>14</sup> means that the cutoff wavelength of a shallow-junction n-p photodiode can be significantly shortened at moderate acceptor concentrations ( $10^{17} \text{ cm}^{-3}$ ). Second, in the case of a wide-bandwidth photodiode a trade-off between minimizing the reverse-bias tunneling current and maximizing the absorption coefficient results in an absorption length of  $\lambda/3$  for optimized photodiodes over the 3- to 36- $\mu\text{m}$  region.

D. L. Spears  
P. E. Duffy

#### C. CHEMICAL ETCHING OF CLEAVED FACETS OF THE GaInAsP/InP DOUBLE HETEROSTRUCTURE

The thickness of the GaInAsP active layer, which is generally 0.1 to 0.5  $\mu\text{m}$ , is an important parameter in GaInAsP/InP double heterostructure lasers.<sup>15-19</sup> For an accurate measurement it is necessary to delineate the active layer in the cleaved facets by chemical etching. Perhaps the most commonly used etchant is the aqueous solution of KOH and  $\text{K}_3\text{Fe}(\text{CN})_6$ , which preferentially etches the GaInAsP active layer.<sup>15,17,19</sup> However, there exists the possibility of over-etch (i.e., some etching of the InP cladding layer), which can result in an apparent active layer thickness which is greater than the actual value. We have found in this work that considerable

TABLE I-1 ETCHING SOLUTIONS USED IN THIS WORK AND THEIR RATES OF OVER-ETCH			
Solution	[ $K_3Fe(CN)_6$ ]	[KOH]	Increase of Apparent Active Layer Thickness
1	0.030 M	1.5 M	8.4 Å/s
2	0.0076	1.5	4.0
3	0.076	1.5	16.0
4	0.030	3.0	36.5

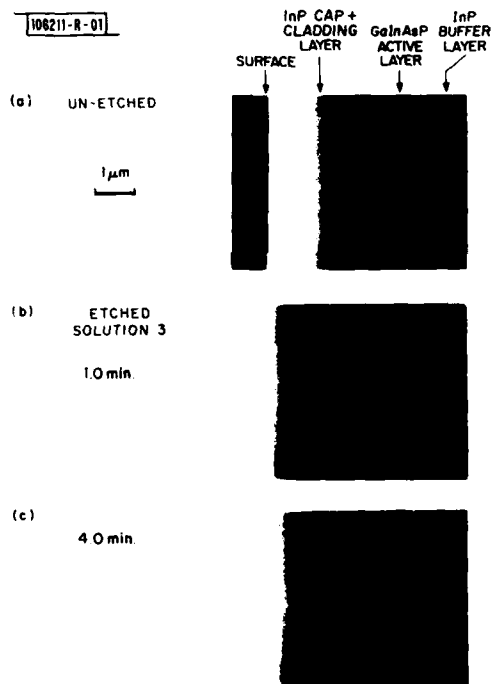


Fig. I-6. SEM micrographs of cleaved edges of an unetched sample and two etched ones. These samples were cleaved from the same LPE wafer.

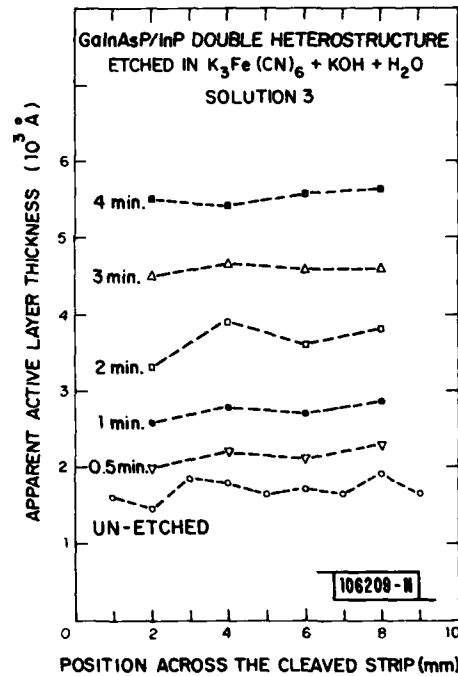


Fig. I-7. Apparent active layer thicknesses measured at various positions across a series of cleaved strips which have been etched for different lengths of time.

over-etch can indeed occur for the commonly used etching conditions and have determined the conditions required to minimize over-etch.

The GaInAsP/InP wafer was prepared by sequential LPE growths of a Sn-doped InP buffer layer ( $n \cong 2 \times 10^{18} \text{ cm}^{-3}$ ), a nominally undoped GaInAsP active layer (with nearly exact lattice match to InP), a Zn-doped InP cladding layer ( $p \cong 2 \times 10^{17} \text{ cm}^{-3}$ ), and a more heavily Zn-doped InP cap layer ( $p \cong 3 \times 10^{18} \text{ cm}^{-3}$ ) on an (100) InP substrate (Sn-doped,  $n \cong 1.5 \times 10^{17} \text{ cm}^{-3}$ ). The active layer was  $0.18 \mu\text{m}$  thick; the thickness of the buffer layer and that of the sum of the cap plus cladding layer were both  $\sim 4 \mu\text{m}$ . Broad-area lasers fabricated from similar wafers have shown threshold current densities as low as  $0.9 \text{ kA/cm}^2$  with an emission wavelength of  $1.3 \mu\text{m}$ . The wafer was  $1.0 \times 1.5 \text{ cm}^2$  and was cleaved into some 20 strips for various etching tests. To prepare etching solutions, weighed amounts of KOH and  $\text{K}_3\text{Fe}(\text{CN})_6$  were first separately dissolved into deionized water to form solutions of known concentrations. The two solutions were then homogeneously mixed to form etching solutions. Four different etching solution compositions were used in this work, as shown in Table I-1. (The concentrations quoted in Table I-1 are those in the final mixture.)

Figure I-6 shows scanning electron microscope (SEM) micrographs of an unetched sample and two etched ones. It should be noted that the etched samples show apparent active layer thicknesses which are considerably greater than that of the unetched one, and yet the layer boundaries still remain very sharp (i.e., no direct evidence of over-etch). The apparent active layer thickness was measured with the SEM at various positions across the length of each cleaved strip. Figure I-7 shows the results of such measurement for a series of strips etched in Solution 3. The average of apparent active layer thicknesses of each strip was then plotted against etching time, as shown in Fig. I-8. Figure I-8 shows that for each etching solution the apparent

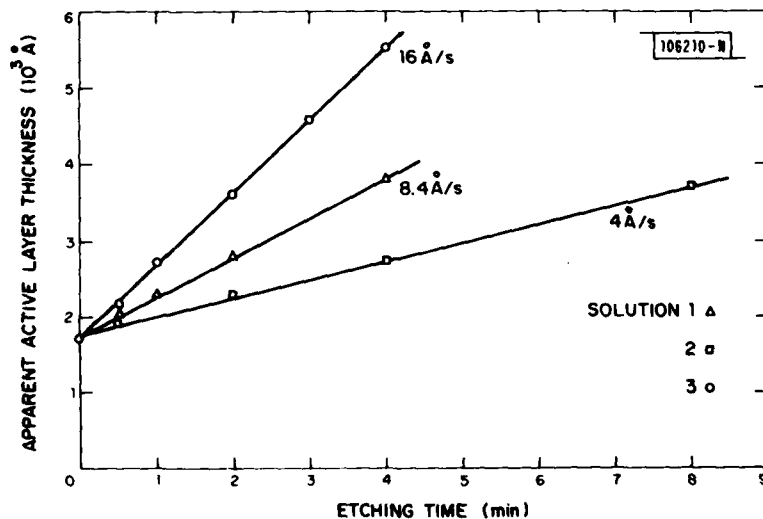


Fig. I-8. Apparent active layer thickness as a function of etching time for three different etching solution compositions.

active layer thickness increases linearly with etching time. The slopes are the rates of thickness increase as quoted in Table I-1.

It should be noted that rates of increase of apparent active layer thickness as high as 36.5 Å/s were obtained in the present investigation; yet the concentrations of  $K_3Fe(CN)_6$  and KOH used in this work were comparable with those quoted in the literature.<sup>20</sup> In view of these results, we feel that some of the previously published data concerning laser characteristics, which depend on active layer thickness measurement, e.g., the normalized threshold current densities, are open to question. (We found that none of the published work which employed chemical etching for active layer measurement specified the etching conditions.) Based on the present work, low etching solution concentrations and short etching times (<10 s) should be used in order to reduce the over-etch to negligible amounts.

Z. L. Liau      D. E. Mull  
T. A. Lind     J. N. Walpole  
L. Missagia

#### D. SUBSTRATE TRANSFER TECHNIQUE FOR LPE GROWTH

A new method has been demonstrated for preventing thermal etching, or decomposition, of InP substrates prior to liquid-phase-epitaxial (LPE) growth. With this method, the substrate is stored in the growth tube, but at room temperature, during the pregrowth bake and then is transferred to the LPE slider shortly before growth. This technique requires only a modest increase in apparatus complexity, and, for the most part, is straightforward in concept and use. There is one subtlety, however, which yields some information about a source of contamination in the LPE growth process, as discussed below.

Long-term baking of growth solutions is necessary to reduce the net donor concentration in LPE-grown InP and InGaAsP alloys below the  $1 \times 10^{16} \text{ cm}^{-3}$  level. Best results are obtained when the growth directly follows this baking, i.e., without opening the system to load a substrate. For growth of InP and InGaAsP alloys of moderate phosphorus content, thermal etching of the substrate during the pregrowth bake can be prevented by introducing a gaseous source of phosphorus, usually  $PH_3$ , into the growth tube atmosphere. However, for growth of alloys of low phosphorus content, and especially for InGaAs, the phosphorus in the atmosphere quickly contaminates the growth solution.

One approach to this problem is to localize the protective phosphorus-rich atmosphere to the well of the slider containing the substrate,<sup>21</sup> a method that is limited to short bake times by the difficulty of providing a gas tight well in an LPE boat. The technique we report here, of storing the substrate outside the hot zone of the furnace and then transferring it to the slider shortly before growth, is useful for indefinitely long bake times. For example, in a recent growth of InGaAs, the boat with growth and etch solutions was baked at 660°C for well over 100 hr. The substrate was transferred from its room-temperature environment within the growth tube to its normal protected position in the slider before a 30-min. pregrowth equilibration. Just prior to growth, it was slid to an open well for inspection through the transparent furnace, then slid under a pure In solution for a slight etchback,<sup>22</sup> and finally slid under the growth solution. As in all our growths with this technique, there was no visual evidence of thermal degradation of the substrate at the time of the inspection, and the morphology of the epitaxial growth was excellent.

During first growths using the substrate transfer technique, the piece of graphite which served as the substrate carrier was kept at room temperature during pregrowth bake and then moved into the hot zone for the transfer. Although the growth morphology in this situation was fine, the net donor concentration was a factor of 10 to 50 larger than the  $1 \times 10^{15} \text{ cm}^{-3}$  expected.

A modified procedure incorporating two substrate carriers was then tried. One carrier, as before, held the substrate at room temperature during the pregrowth bake, but the second carrier was kept in the hot zone of the furnace. To make the transfer, the baked carrier was moved out of the furnace and the substrate was moved into it. Then this carrier was moved back into the furnace and the transfer to the slider made. With this procedure, the expected  $1 \times 10^{15} \text{ cm}^{-3}$  net donor levels have been reproducibly obtained.

It seems clear from these experiments that gases given off during heating of the graphite after exposure to air contaminate the growth. The expected gases are  $\text{H}_2\text{O}$ ,  $\text{CO}$ , and  $\text{CO}_2$  (Ref. 23). The positive effect of  $\text{H}_2\text{O}$  at the fractional ppm level has been studied.<sup>24</sup> It is thought to convert Si in the growth solution to electrically inactive  $\text{SiO}_2$ . At levels somewhat in excess of 1 ppm the  $\text{H}_2\text{O}$  causes increased compensation, but an increase in net donor concentration has not been observed. The effect of  $\text{CO}$  and, especially,  $\text{CO}_2$  in oxidizing Si should be qualitatively similar to that of  $\text{H}_2\text{O}$ . We therefore conclude that some other gas or gases desorbed from the graphite during heating contaminate the LPE growth of InP and InGaAsP alloys. However, the details of this contamination process are not presently understood.

S. H. Groves  
M. C. Plonko

## REFERENCES

1. For review, see J. P. Donnelly, C. O. Bozler, and R. A. Murphy, *Circuits Mfg.* 18, 45 (1978).
2. J. C. Dymont, J. C. North, and L. A. D'Asaro, *J. Appl. Phys.* 44, 207, (1973).
3. E. Garmire, H. Stoll, A. Yariv, and R. G. Hunsperger, *Appl. Phys. Lett.* 21, 87 (1972).
4. J. P. Donnelly and C. E. Hurwitz, *Solid-State Electron.* 20, 727 (1977); J. P. Donnelly, to be published in *Nuclear Instrument and Methods*.
5. J. J. Hsieh, J. A. Rossi, and J. P. Donnelly, *Appl. Phys. Lett.* 28, 709 (1976).
6. B. O. Seraphin and H. E. Bennett, Vol. 3 of *Semiconductors and Semimetals* (Academic Press, New York, 1967).
7. R. E. Nahory and M. A. Pollack, *Electron. Lett.* 14, 727 (1978).
8. G. W. Iseler (unpublished).
9. M. Feng, T. H. Windhorn, M. M. Tashima, and G. E. Stillman, *Appl. Phys. Lett.* 32, 758 (1980).
10. R. H. Kingston, *Appl. Phys. Lett.* 34, 744, (1979).
11. F. J. Leonberger (unpublished).
12. M. D. Blue, *Phys. Rev.* 134, A226 (1964).
13. E. Finkman and Y. Nemirovsky, *J. Appl. Phys.* 50, 4356 (1979).
14. T. N. Casselman and P. E. Peterson, *Solid State Commun.* 33, 615 (1980).
15. J. J. Hsieh, J. A. Rossi, and J. P. Donnelly, *Appl. Phys. Lett.* 28, 709 (1976).
16. R. E. Nahory and M. A. Pollack, *Electron. Lett.* 14, 729 (1978).
17. Y. Itaya, Y. Suematsu, S. Katayama, K. Kishino, and S. Arai, *Jap. J. Appl. Phys.* 18, 1795 (1979).
18. S. Arai, Y. Suematsu, and Y. Itaya, *IEEE J. Quantum Electron.* QE-16, 197 (1980).
19. H. Kawaguchi, K. Takahei, Y. Toyoshima, H. Nagai, G. Iwane, *Electron. Lett.* 15, 669 (1979).
20. M. C. Hales, J. R. Knight, and C. W. Wilkins, *1970 Symposium on GaAs* (The Institute of Physics, London 1970), p. 50.
21. G. A. Antypas, *Appl. Lett.* 37, 64 (1980).
22. V. Wrick, G. J. Scilla, and L. F. Eastman, *Electron. Lett.* 12, 394 (1976).
23. A. R. Calawa, private communication.
24. S. H. Groves and M. C. Plonko, Chap. 1 in *Gallium Arsenide and Related Compounds (St. Louis) 1978* (The Institute of Physics, London, 1979), pp. 71-77, DDC AD-A072649/7.

## II. QUANTUM ELECTRONICS

### A. EFFECT OF TURBULENCE-INDUCED CORRELATION ON LIDAR MEASUREMENT ERRORS

Using a 10.6- $\mu\text{m}$  dual-laser differential-absorption LIDAR (DIAL) system, we have measured the short-term and long-term temporal correlation of the DIAL returns from topographic targets and have investigated the associated effect on the measurement error (standard deviation) of the time-averaged DIAL returns. Our results have been used to establish the accuracy of DIAL laser remote sensing measurements and to quantify the improvement expected through use of a dual-laser DIAL system compared with that of a single-laser system. This improvement is shown to be in good agreement with that predicted from a theory which considers the effect of partial temporal correlation due to atmospheric turbulence on DIAL measurement errors.

Our results were obtained using the dual-laser  $\text{CO}_2$  DIAL and data acquisition systems reported previously.<sup>1</sup> The DIAL system consists of two individually triggered mini-TEA  $\text{CO}_2$  lasers coupled to a common LIDAR optical system. Figure II-1 shows a time history of the amplitude of the LIDAR returns as a function of time. The temporal separation between the two LIDAR pulse-pairs was 35  $\mu\text{s}$  and the PRF of each laser was 5.4 Hz. The short- and long-term correlation of the two LIDAR returns is evident in Fig. II-1, which displays the role that atmospheric turbulence plays in these processes. The data corresponding to this figure were used to measure the standard deviation of each individual LIDAR return signal, X or Y, as well as that of (X/Y), on a pulse-to-pulse basis. The results are presented in Fig. II-2 and show the standard deviation of the returns from two different targets as a function of the number of pulses integrated. As seen in Fig. II-2, (1) the DIAL measurement error for the dual-laser values, (X/Y), is considerably less than that for either X or Y; (2) the measurement error decreases approximately as the square root of the number of pulses integrated, with some deviations noted at longer integration times; and (3) the returns from different targets have different statistical distributions.

We have also measured the cross-correlation coefficient,  $\rho_{\Delta t}$  of the two LIDAR returns as a function of the delay times.<sup>1</sup> Our results are shown in Fig. II-3 where it is seen that the correlation is high ( $\rho_{\Delta t} \approx 0.5-0.9$ ) at  $\Delta t = 35 \mu\text{s}$ , rapidly falls off to a value of 0.2 to 0.1 for  $\Delta t$  between 200 ms and 5 s, and is essentially zero for time delays greater than 5 to 10 s.

Our experimental results can be shown to be consistent with those predicted for the case of two nonindependent measurements of a nonstationary process. Using the general formalism for the propagation of errors<sup>2</sup> and applying this to the DIAL equation, one obtains for the overall measurement error (standard deviation) of the dual-laser DIAL system

$$\frac{\sigma_{\xi}^2}{(\xi)^2} = \frac{\sigma_x^2}{(X)^2} + \frac{\sigma_y^2}{(Y)^2} - 2\rho_{\Delta t} \frac{\sigma_x}{X} \frac{\sigma_y}{Y} \quad (\text{II-1})$$

where

$$\rho_{\Delta t} = \frac{\sigma_{xy}}{\sigma_x \sigma_y} \quad (\text{II-2})$$

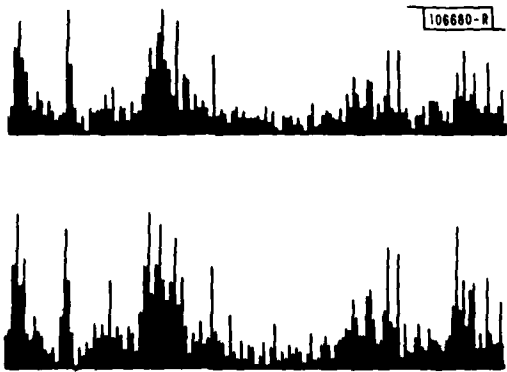
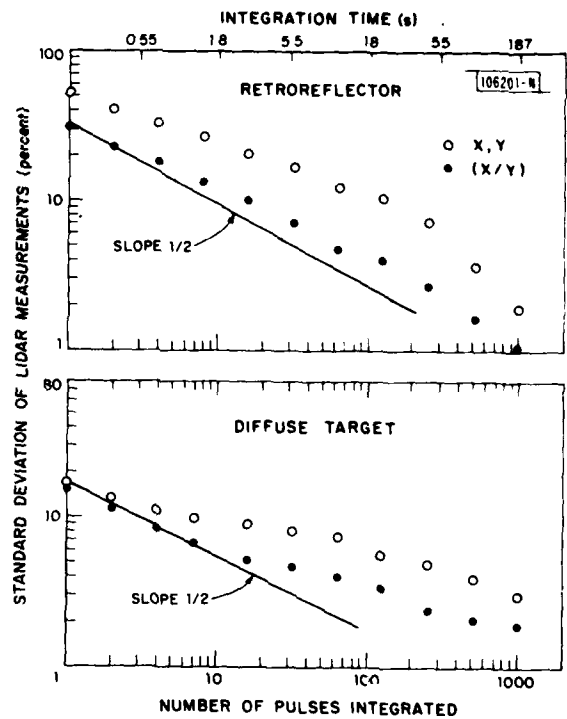


Fig. II-1. Time series display of pulsed LIDAR returns; upper trace for LIDAR 1, lower trace for LIDAR 2.

Fig. II-2. Measured standard deviation of single-laser ( $\sigma_x$ ) and dual-laser ( $\sigma_y$ ) LIDAR returns as a function of the number of pulses integrated.



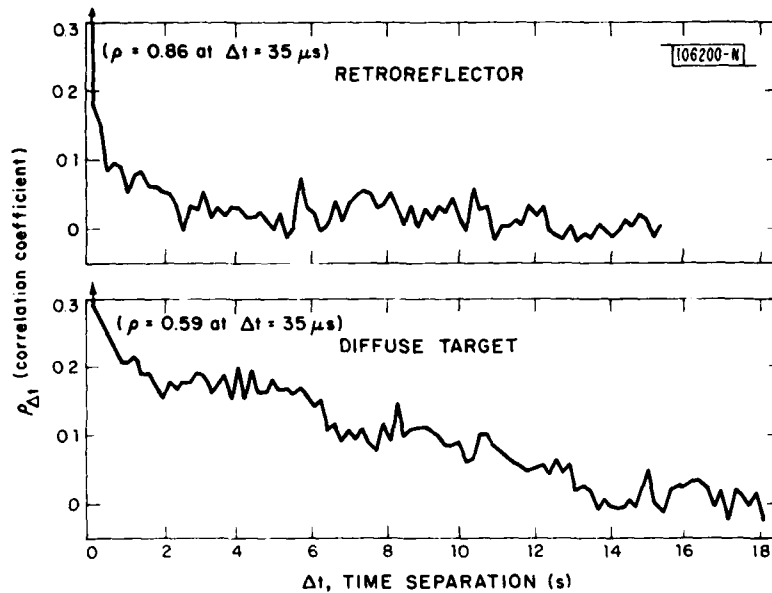


Fig. II-3. Cross-correlation coefficient,  $\rho_{\Delta t}$ , measured as a function of time separation of the two LIDAR returns.

is the correlation coefficient,  $\xi \equiv X/Y$ , and  $\sigma_{xy}$  is the covariance of  $X$  and  $Y$ .  $(\sigma_{\xi}/\bar{\xi})$ ,  $(\sigma_x/\bar{X})$ , and  $(\sigma_y/\bar{Y})$  are the standard deviations normalized to the mean value for  $\bar{\xi}$ ,  $\bar{X}$ , and  $\bar{Y}$ , respectively. For the case where  $\sigma_x = \sigma_y \equiv \sigma$ , and for  $\bar{\xi} = \bar{X} = \bar{Y} = 1$ , Eq. (II-1) may be written as

$$\sigma_{\xi}^2 = 2\sigma^2(1 - \rho_{\Delta t}) \quad (II-3)$$

Equations (II-1) and (-3) indicate that the effect of correlation ( $\rho_{\Delta t} > 0$ ) is to reduce the overall measurement error,  $\sigma_{\xi}/\bar{\xi}$ . In addition, the effect of signal processing is to operate either  $(1/N) \Sigma$  or  $(1/T) \int dt$  on Eq. (II-1), where  $N$  is the number of pulses integrated over a time period  $T$ . Under these conditions, any nonstationary term in Eq. (II-1), and in particular  $\rho_{\Delta t}$ , will cause deviations from the  $\sqrt{N}$  dependence.

Using the values from Figs. II-2 and II-3 of  $(\sigma_x/\bar{X}) = 0.545$  and  $0.1635$ , and  $\rho_{\Delta t} = 0.867$  and  $0.593$ , Eq. (II-1) yields  $(\sigma_{\xi}/\bar{\xi}) = 0.28$  and  $0.14$  for the retroreflector and diffuse target returns, respectively. These values are in good agreement with our measured values from Fig. II-2 of  $(\sigma_{\xi}/\bar{\xi}) = 0.312$  and  $0.151$ , respectively. In addition, the deviation from the  $\sqrt{N}$  dependence in Fig. II-2 is consistent with the temporal variation of  $\rho_{\Delta t}$  shown in Fig. II-3.

D. K. Killinger  
N. Menyuk

#### B. Ni:MgO LASER: HIGH AVERAGE POWER AND TUNING PROPERTIES

The Ni:MgO transition-metal laser has been operated at up to 10.3 W CW output in a  $TEM_{00}$  mode with a slope quantum efficiency of 57 percent when pumped with a 1.06- $\mu\text{m}$  Nd:YAG laser. This device produced tunable output in two wavelength regions around 1.31 and 1.38  $\mu\text{m}$ .

A schematic diagram of the Ni:MgO laser is shown in Fig. II-4. The 1.85-cm-long laser crystal was conduction cooled to liquid-nitrogen temperature by a dewar designed to have a large area of contact between the cryogenic liquid and the copper cold finger. The birefringent tuning element was adjusted using a vacuum-tight rotary feedthrough. The optical pumping

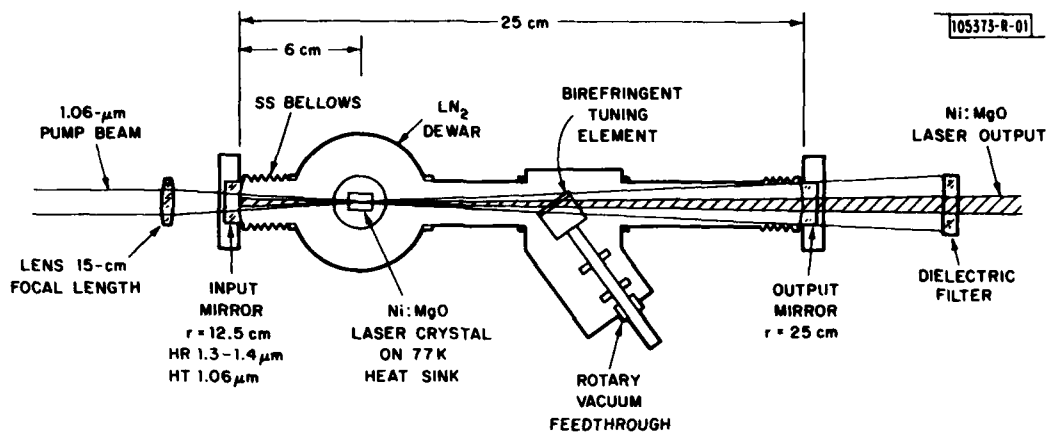


Fig. II-4. Schematic diagram of Ni:MgO laser.

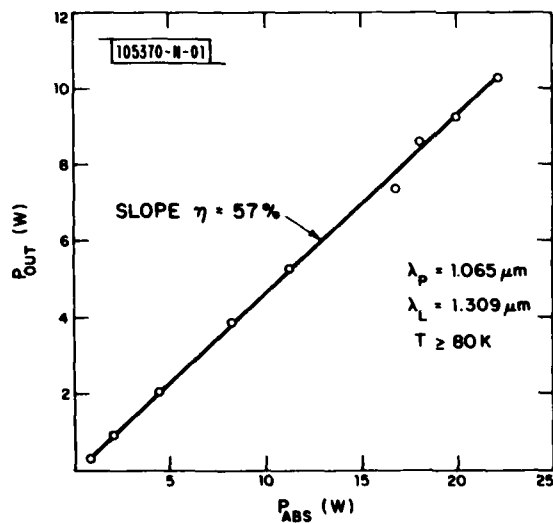


Fig. II-5. Ni:MgO laser output power vs absorbed input power for 5.3% output coupling.

geometry was such that all of the multi-transverse-mode output of the pump laser was focused into the  $TEM_{00}$ -mode volume (as determined by the cavity of Fig. II-4) in the Ni:MgO crystal. This gain-aperturing effect resulted in  $TEM_{00}$  output from the Ni:MgO laser at all pumping levels. The output power vs absorbed input power curve with a 5.3%-transmission output mirror and no tuning element is shown in Fig. II-5; the output wavelength was  $1.309 \mu\text{m}$ . The near-threshold behavior under several different operating conditions is shown in Fig. II-6. The lowest threshold was obtained with a 1.6%-transmission mirror at  $\sim 40 \text{ mW}$  of absorbed power. Insertion of the Brewster-angle tuning element resulted in a noticeable intracavity loss, with resultant increased threshold and reduced slope efficiency, presumably because of residual and pump-induced birefringence in the cubic MgO host crystal. The latter effect undoubtedly accounts for the gradual reduction in slope efficiency as the pump power is increased, as is evident for the input-output curve (Fig. II-6) with the tuning element in the cavity.

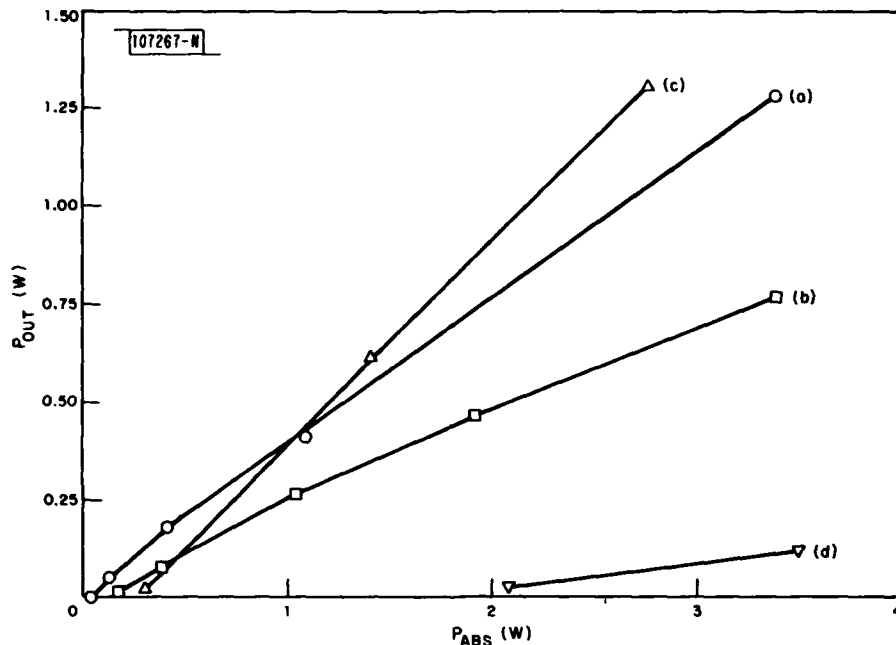


Fig. II-6. Near-threshold input-output behavior for Ni:MgO lasers (a) output coupling 1.6 percent, no tuning element; (b) output coupling 1.6 percent, tuning element set to  $1.309 \mu\text{m}$ ; (c) output coupling 5.3 percent, no tuning element; (d) output coupling 1.6 percent, tuning element set to  $1.38 \mu\text{m}$ .

Tuning of the Ni:MgO laser was carried out at a pumping level of 5 W absorbed power. Oscillation was observed not only on the relatively pronounced peak of the fluorescence curve<sup>3</sup> around  $1.31 \mu\text{m}$  but also on a secondary peak around  $1.38 \mu\text{m}$ . Tuning around  $1.31 \mu\text{m}$  was not continuous, however; though laser operation ranged from  $1.305$  to  $1.317 \mu\text{m}$ , there were intermediate wavelengths where oscillation could not be obtained. Peak output occurred at  $1.309 \mu\text{m}$ . Continuous tunability was achieved from  $1.376$  to  $1.387 \mu\text{m}$ , and a maximum output of  $0.25 \text{ W}$  was observed at an absorbed pump power of  $6.5 \text{ W}$ .

Further study is required to explain several inconsistencies in the behavior of the Ni:MgO laser. From the ratio of slope efficiencies obtained with the two different output couplings, one

calculates a cavity round-trip loss (excluding the output mirror) of 1.1 percent. The loss is not consistent with either the ratio of thresholds observed with the two mirrors or the absolute slope efficiencies measured. Possible explanations for these problems may involve either excessive scattering loss in one of the mirrors or an intrinsic property of the Ni:MgO laser medium. The lack of continuous tunability around the 1.31- $\mu\text{m}$  fluorescence peak is also unexpected and may be due to the interaction between the birefringent tuning element and the birefringence of the Ni:MgO crystal or the effect of injected  $^4\text{F}_{3/2} \rightarrow ^4\text{I}_{13/2}$  fluorescence (around 1.32  $\mu\text{m}$ ) from the Nd:YAG pump laser.

P. F. Moulton  
A. Mooradian

### C. LASER PHOTOCHEMICAL MICROALLOYING FOR ETCHING OF ALUMINUM THIN FILMS

It has been previously<sup>4</sup> shown that UV laser microphotochemical reactions can be used to generate high-resolution doping patterns on semiconductor surfaces. By a similar technique, Al films have been changed in composition by first producing Zn in a photochemical reaction and then alloying the two metals via local heating. The objective of the process is to alter a specific physical property, namely the metal's corrosion resistance, in order to predispose a small area of an Al film to subsequent etching by chemical reaction. Since small impurity levels have dramatic effects on surface reactivities, this approach may have applicability to maskless high-resolution etching for microfabrication. The process occurs at relatively low temperatures, well below the Al melting point. The primary motivation for using a laser to control this reaction is to make use of the high spatial coherence of a laser beam to localize the reaction to micrometer dimensions. The nonthermal, photochemical component of the process has also been shown to be fundamentally useful as a means of controlling material transport to a localized reaction region on a surface.

Zn was chosen as a dopant for the present study because of the high miscibility of Al and Zn and because of the rapid diffusion of Zn in Al at moderate temperatures. A further motivation for this choice was the possibility of beneficial Zn reduction reactions with the  $\text{Al}_2\text{O}_3$  native oxide on the Al surface.

For the present experiments, the output of a frequency-doubled CW Ar-ion laser was used to photodissociate  $\text{Zn}(\text{CH}_3)_2$  vapor which was held at a pressure of 20 to 200 Torr in a 2-cm-path-length gas cell. Operating alone, this beam produces a well-localized Zn surface deposit in the manner described previously for photodeposition of other metals. For the present experiments, however, the 514.5-nm fundamental output from the Ar-ion laser (typically 2 W) was used to incorporate the Zn in the Al film by surface heating. The samples were electron-beam-evaporated Al films of 200 to 5000  $\text{\AA}$  thickness on Pyrex substrates used after several days exposure to air in order to simulate normal oxidized surfaces. The coaxial UV and visible beams were focused on the substrate with a 7.5-cm focal-length, single-element, LiF lens. The substrates were translated in the laser focus by a 0.2- $\mu\text{m}/\text{step}$  stepping motor. Substrates were raster scanned to obtain areas of several square millimeters for diagnostics.

After irradiation, the samples were given a 1- to 2-min. rinse in a 15%-aqueous acetic acid solution to remove the microalloyed regions of the film. The result of this procedure was found to be relatively insensitive to exact conditions; despite 50-percent variations in the rinse duration or acid concentration, substantially the same film area was dissolved. The rate

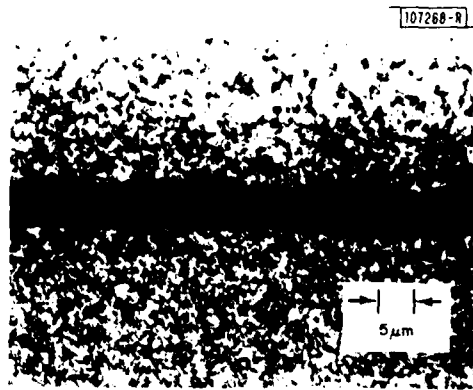
of dissolution of untreated Al films was determined in an independent measurement to be  $\sim 0.1 \text{ \AA}/\text{min}$ . at  $23^\circ\text{C}$ .

A brief study showed that the microalloyed regions could also be selectively removed in a  $\text{BCl}_3$  RF plasma, although the differential in rate between the alloyed and untreated regions appeared to be less marked than for the wet etch. This is not surprising since this particular plasma is an efficient etch for unalloyed Al, and no attempt was made to optimize conditions in the plasma to maximize the rate differential.

A series of qualitative tests was also made to help to elucidate the laser alloying step. The gas  $\text{Cd}(\text{CH}_3)_2$  was substituted for  $\text{Zn}(\text{CH}_3)_2$  in order to compare results with metals (Zn and Cd) of vastly different solubilities in Al, but very similar chemical reactivity. In particular, both Cd and Zn are easily dissolved in dilute acetic acid. Although Cd surface deposits were readily produced, and these deposits were visibly redistributed by the high-intensity beam, no effects of microalloying or differential etching were seen.

In the CW experiment, alloying occurs by solid-state diffusion of the texture, which extends laterally over many beam diameters. The edge irregularities shown in Fig. II-7 are much larger than the initial Al grain size, and may result from inhomogeneities in the alloy from phase segregation on cooling. Despite this lateral diffusion, microalloyed-enhanced etching has resulted in 5- to 6- $\mu\text{m}$  resolution, showing its applicability for severing aluminum conductors in integrated circuits.

Fig. II-7. Optical micrograph of a 2000- $\text{\AA}$ -thick Al film following laser microalloying and an acetic acid rinse.



We have thus demonstrated a laser photochemical/thermal microalloying reaction which can predispose small areas of Al films to subsequent removal by etching. The process has been shown to be capable of rapidly producing alloys of greatly increased chemical reactivity at moderate peak temperatures and should be applicable to etching of other conducting and semi-conducting materials. In the particular application examined here we have shown that a low-temperature, relatively benign process may be used to disconnect aluminum conductors. The low-temperature aspect of the process reduces both the accidental doping of a semiconductor substrate or production of undesired debris, problems which are encountered in laser-blowoff disconnect techniques.

D. J. Ehrlich  
R. M. Osgood, Jr.  
T. F. Deutsch

#### D. MEASUREMENT OF ADSORBED MOLECULAR FILMS BY REFLECTOMETRY

Several recent experiments have shown the importance of adsorbed molecular films in controlling the rate and resolution of laser photochemical processing. In fact, photodissociation of adsorbed films alone has been used in the recently developed technique of UV laser pre-nucleation. To measure many of the important characteristics of these films, such as their pressure and temperature dependence, requires development of the appropriate diagnostic techniques. Optical diagnostics must be used because the relatively high-pressure gas ambient above the film precludes the use of electron- or ion-beam probes.

We have developed an optical diagnostic technique which is based on the change in interference from a thin-film structure after adsorption of a molecular layer. The technique has a simple optical path so that it can be used in a variety of small gas cells; in addition it can, in principle, have a fast response time and be spectrally sensitive so that both transient and spectral data can be collected.

It is usually difficult to detect a thin transparent film of approximately one monolayer by measuring the change in local reflectivity of a portion of a substrate. If the substrate is simply a window of transparent material (e.g., glass), suitably shaped to separate the reflection from its outer surface (Fig. II-8), its initial coefficient of reflection, i.e., ratio of reflected to incident amplitudes, is real with a  $0^\circ$  or  $180^\circ$  phase shift. To first order, the effect of a very thin film of thickness,  $d$ , ( $d \ll \lambda$ ) consists only in adding a phase shift, proportional to  $d$ , to

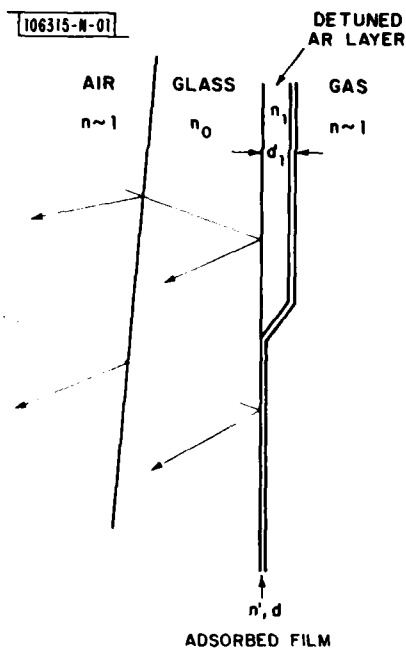


Fig. II-8. Reflection at a surface covered by an adsorbed film, for an uncoated substrate (bottom) and in the presence of an AR coating (top).

the "bare" surface reflectivity,  $R_0$ , and such a thin film is not detectable by reflectance measurements. Simple application of the Fresnel relations at the two interfaces shows that for  $d \ll \lambda$ , the phase shift  $\phi$  is given by

$$\phi = (2\pi d n' / \lambda) (1/n' - n') 2n_0 / (n_0^2 - 1) \quad (\text{II-4})$$

where  $n_0$  and  $n'$  are the substrate and adsorbed-film refractive indices, respectively.

If instead of a bare substrate we use one which has been coated with a preliminary thin layer (top portion Fig. II-8), the addition of an adsorbed film can cause a marked change in the reflectance, depending on the parameters of the initial layer. The most interesting case is that of an antireflecting (AR) structure, such as a single low-index layer close to a quarter wave in thickness, neglecting, for simplicity, multiple reflections since the reflectivities are small.

For an AR layer which is exactly  $\lambda/4$  in thickness, the fields reflected from the front and back surface are exactly opposite in phase, and as in the case of an uncoated substrate, the addition of a very thin adsorbed film has no first-order effect on the amplitude of the reflection coefficient. However, if the AR layer is close to but not exactly tuned for minimum reflectivity, it can be shown that the adsorbed film will give a signal linearly proportional to its thickness. Under optimum conditions which can be achieved in the optical region, an approximate expression for the fractional change in reflectivity  $\Delta R/R_0$  due to the adsorbed film is

$$\Delta R/R_0 = \frac{1}{\sqrt{2R_0}} \left( \frac{1}{n'} - n' \right) \frac{2\pi n'}{\lambda} d \quad (\text{II-5})$$

Assuming, for example,  $\lambda = 6328 \text{ \AA}$ ,  $d = 5 \text{ \AA}$ ,  $n' = 1.5$ , and  $R_0 = 0.005$ , the presence of the adsorbed film changes the reflected intensity by 6 percent (whether  $R$  increases or decreases depends on the direction in which the AR layer is detuned).

The technique described has been implemented in a variety of ways; a simple arrangement which is being employed in the study of surface adsorption from organometallic gases is sketched in Fig. II-9. Using a plano-convex lens for a window is particularly convenient, since it

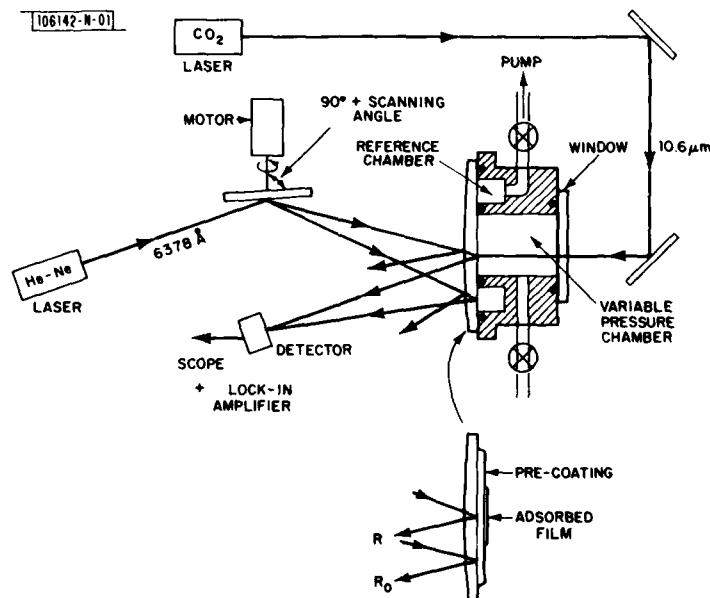


Fig. II-9. Experimental setup for measuring the thickness of adsorbed films of organometallic gases.

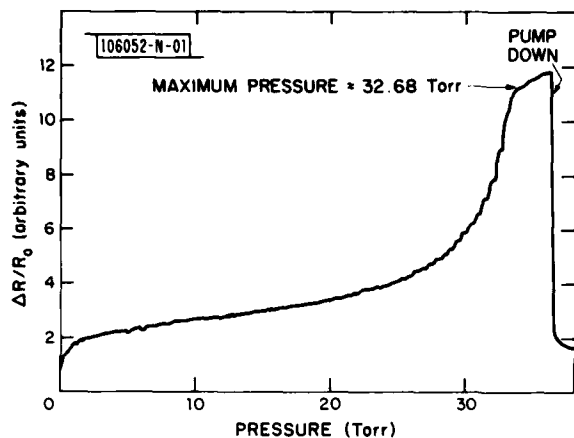


Fig. II-10. Adsorption isotherm for  $\text{Cd}(\text{CH}_3)_2$  on  $\text{MgF}_2$ -coated glass.

displaces the unwanted reflection and focuses the scanning beam onto a small-area detector. Scanning the beam position allows averaging over microscopic spatial inhomogeneities on the surface and references the reflectivity to that of an unexposed portion of the substrate. The  $\text{CO}_2$  laser beam, which enters from the back window of the cell, permits a controlled heating of the substrate for observing the effects of temperature variation on adsorption. Figure II-10 gives a preliminary set of data for dimethylcadmium vapor which shows the relative change in reflection,  $\Delta R/R_0$ , of the substrate as a function of gas pressure. Since according to Eq. (II-5),  $\Delta R/R_0$  is proportional to film thickness or coverage, these data give the adsorption isotherm (i.e., adsorbed thickness vs pressure at constant temperature) for dimethylcadmium vapor on  $\text{MgF}_2$ . We are currently examining the applicability of these interference techniques to measuring adsorption onto thin, optically lossy semiconductor layers and to spectroscopy of adsorbed films.

V. Daneu  
D. J. Ehrlich  
R. M. Osgood, Jr.

#### REFERENCES

1. Solid State Research Report, Lincoln Laboratory, M.I.T. (1980:4), p. 13.
2. G. E. P. Box and G. M. Jenkins, Time Series Analysis (Holden-Day, San Francisco, 1970).
3. Solid State Research Report, Lincoln Laboratory, M.I.T. (1978:1), p. 20, DDC-AD-A056715/6.
4. D. J. Ehrlich, R. M. Osgood, Jr. and T. F. Deutsch, Appl. Phys. Lett. 36, 698 (1980).

### III. MATERIALS RESEARCH

#### A. LATERAL EPITAXY BY SEEDED SOLIDIFICATION FOR GROWTH OF SINGLE-CRYSTAL Si FILMS ON INSULATORS

Composite structures consisting of single-crystal Si films on insulating substrates are of great interest for many device applications. The growth of such Si films on single-crystal sapphire substrates by vapor-phase epitaxy<sup>1</sup> is a well-established technology, but the high defect density in the Si films and the high dielectric constant of sapphire limit device performance. As an alternative to silicon-on-sapphire technology, we are investigating a technique for preparing single-crystal Si films over thin insulating layers formed on single-crystal Si substrates. After formation of such an insulating layer, narrow stripes are opened to expose the Si substrate, and a film of amorphous or polycrystalline Si is deposited over the entire surface. The Si film is melted and frozen in such a manner that solidification seeded by the Si substrate initially occurs within each stripe opening and then proceeds laterally over the adjacent insulating layer. This process, which we call the LESS technique (lateral epitaxy by seeded solidification), can yield a continuous single-crystal Si film over the insulator.

In previous studies of this process, single-crystal Si films have been obtained over SiO<sub>2</sub> layers by melting polycrystalline Si films with a pulsed ruby laser<sup>2</sup> or scanned CW Ar laser,<sup>3</sup> but the distance of single-crystal overgrowth was limited to 2 and 30 μm, respectively. We have employed a different heating technique. By using two graphite strip-heaters, continuous single-crystal Si films have consistently been grown over SiO<sub>2</sub> layers with stripe openings located 50 μm apart. In preliminary experiments we have also obtained such films over SiO<sub>2</sub> layers with openings 500 μm apart and have observed growth of single-crystal Si extending as far as 4 mm over Si<sub>3</sub>N<sub>4</sub>.

For our experiments, single-crystal Si wafers 5 cm in diameter were cleaned and then masked with an insulating layer 0.2 μm thick of either SiO<sub>2</sub> formed by thermal oxidation or Si<sub>3</sub>N<sub>4</sub> prepared by chemical vapor deposition (CVD). Stripes 3.5 μm wide, perpendicular to the <110> direction, were opened in the masking layer by standard photolithographic techniques. An amorphous Si film 0.8 to 1.0 μm thick was deposited in a CVD reactor at 610°C to produce the structure shown schematically in the lower part of Fig. III-1. Most wafers were capped with a CVD SiO<sub>2</sub> layer about 2 μm thick. Finally, several rectangular samples with dimensions of about 1 × 2 cm were cut from each wafer.

The upper part of Fig. III-1 is a schematic diagram showing the configuration used for the experiments, which were performed in an Ar ambient. The sample was placed on a graphite strip-heater with the Si film facing up, and a narrow, movable graphite strip-heater was positioned about 2 mm above one end of the sample. The lower graphite strip was resistively heated to 1100 to 1300°C in about 20 s. During this time, the Si film was converted from amorphous to finely polycrystalline. The upper strip was then rapidly heated by applying power at a level of about 1 kW. Due to the additional heating of the sample by radiation from this strip, in 20 to 40 s the Si film and the upper surface of the Si substrate were melted in a narrow zone located below it. The strip was then manually moved over the sample at a velocity (about 0.5 cm/s) that was slow enough for the molten zone to traverse the sample at the same rate. When the strip and molten zone reached the far end of the sample, the power to both heaters was switched off. The upper heater was usually moved in the direction parallel to the openings in the growth mask.

103068-N-02

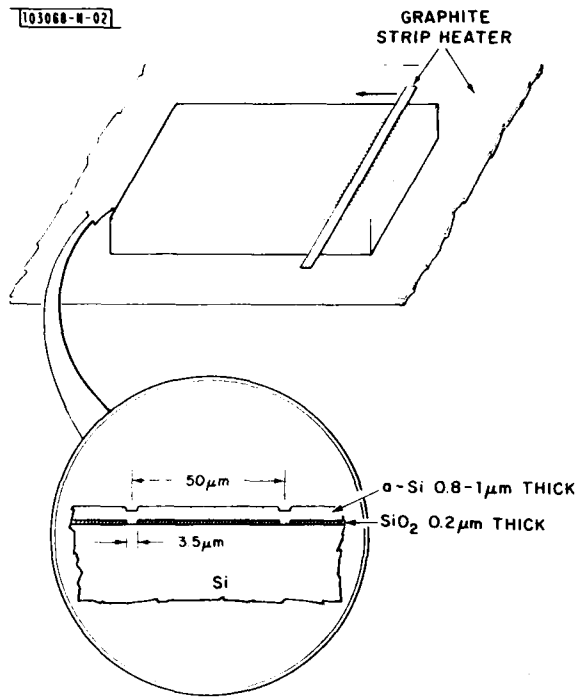
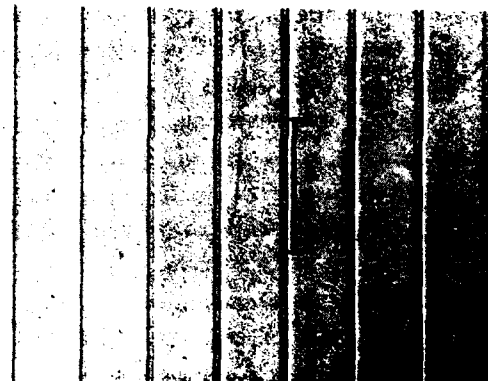


Fig. III-1. Schematic diagram showing the configuration used for accomplishing lateral epitaxy by seeded solidification (LESS) technique. A cross-sectional view of a typical sample before treatment is shown in expanded form.

103730-B-02



(a)

Fig. III-2. (a) Optical micrograph of a single-crystal Si film obtained by using the LESS technique of Fig. III-1. (b) RHEED pattern for a similar film.



(b)

Most of the experiments were performed on  $\langle 100 \rangle$  Si substrates masked with  $\text{SiO}_2$ . Unless otherwise specified, the results described here were obtained for such samples with stripe openings spaced  $50 \mu\text{m}$  apart. In the few cases where the Si film was not capped, the results appeared to be essentially the same as those for films capped with  $\text{SiO}_2$ . Only results for capped samples are reported here. To prepare these samples for characterization, the  $\text{SiO}_2$  cap was removed by etching with HF.

In experiments where the upper strip-heater was moved parallel to the stripe openings in the insulating mask, at any instant the molten zone cut across all these openings. Along the trailing edge of the zone, solidification began within each opening. Growth within the opening was followed by lateral growth over the insulating layer on both sides, which continued until the growth fronts met the fronts originating from the adjacent openings. When the openings were  $50 \mu\text{m}$  apart, this process yielded single-crystal films in which few crystal defects were revealed by etching. Between the openings, these films were smooth except for some surface features formed midway between adjacent openings, at the intersections between growth fronts. Figure III-2(a) is an optical interference micrograph of the as-solidified surface of such a film. The parallel stripes show that the depressions in the film surface located over the stripe openings in the  $\text{SiO}_2$  were retained during melting and solidification.

Figure III-2(b) is a reflection high-energy electron diffraction (RHEED) pattern obtained for another typical Si film crystallized in the same manner. The sharp Kikuchi lines in this pattern indicate that the film is of good crystalline quality. This finding is confirmed by the results of Rutherford backscattering measurements on the same film. The data for one such measurement are shown in Fig. III-3, where the open and closed circles show the backscattering spectra obtained when the beam was incident in a random crystallographic direction and in the  $\langle 100 \rangle$  channeling direction, respectively. The minimum channeling yield ( $\chi_{\text{min}}$ ) is about 5.4 percent, only slightly higher than the value of 4 percent obtained for bulk single-crystal Si.

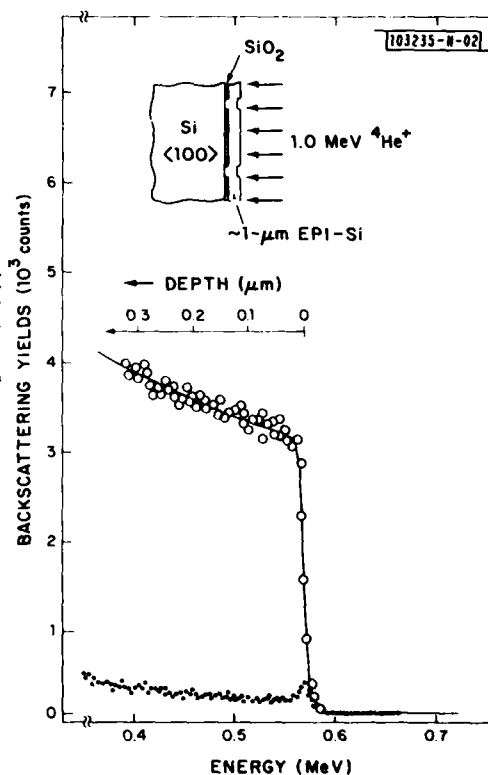


Fig. III-3.  $^4\text{He}^+$  ion backscattering spectra for a LESS Si film. The open and closed circles show the spectra obtained when the beam was incident in a random direction and in the  $\langle 100 \rangle$  channeling direction, respectively.

In a number of preliminary experiments where the upper strip-heater was moved parallel to the stripe openings in the growth mask, as described above, the LESS technique was successfully applied to other types of samples. In these experiments, continuous single-crystal Si films were grown over  $\text{SiO}_2$  or  $\text{Si}_3\text{N}_4$  masks with openings  $500\ \mu\text{m}$  apart on  $\langle 100 \rangle$  Si substrates, and over  $\text{SiO}_2$  masks with openings  $50\ \mu\text{m}$  apart on  $\langle 111 \rangle$  substrates. The results obtained with  $\text{Si}_3\text{N}_4$  masks are especially promising, since single-crystal growth was observed in some areas for distances up to 4 mm beyond the stripe openings.

In a few of the LESS experiments on samples incorporating  $\text{SiO}_2$  growth masks with stripe openings  $50\ \mu\text{m}$  apart on  $\langle 100 \rangle$  Si substrates, the upper strip-heater was moved in the direction perpendicular to the openings. In these experiments, single-crystal films were grown over the  $\text{SiO}_2$  by seeded lateral solidification associated with the formation of a molten zone parallel to the openings. Solidification between two adjacent openings took place by the motion of a single growth front that originated within one of the openings and moved in the same direction as the moving strip. Therefore surface features were not formed midway between the two openings.

As a promising method for preparing large-area, high-quality, single-crystal Si films on insulating layers, the LESS technique may provide an improved alternative to silicon-on-sapphire technology. In addition, this technique should permit the fabrication of devices incorporating multiple isolated semiconductor layers. Furthermore, the LESS technique may make it possible to grow single-crystal Si films on reusable Si substrates, since this technique produces the same basic structure as the one used in the CLEFT process.<sup>4</sup> Finally, it is quite likely that the LESS technique can be applied to other semiconductors, in particular GaAs and InP.

J. C. C. Fan  
M. W. Geis  
B-Y. Tsaur

#### B. HETEROEPITAXY OF VACUUM-EVAPORATED Ge FILMS ON SINGLE-CRYSTAL Si

The growth of heteroepitaxial Ge films on single-crystal Si substrates has been the subject of many investigations undertaken to elucidate the properties of Ge-Si heterojunctions.<sup>5</sup> However, it is difficult to prepare Ge films of good crystal quality because Ge has a larger lattice constant (by  $\sim 4$  percent) and thermal expansion coefficient (by about a factor of 2) than Si.

Following our recent demonstration that efficient GaAs solar cells can be fabricated on single-crystal Ge substrates,<sup>6</sup> we prepared heteroepitaxial films of both  $\text{Ge}_{1-x}\text{Si}_x$  alloys<sup>7</sup> and Ge (Ref. 8) on single-crystal Si, with the objective of developing a technique for providing low-cost substrates for efficient thin-film GaAs cells. Both types of films were obtained by heat treatment of  $\langle 100 \rangle$  Si substrates that had been coated with amorphous Ge by vacuum evaporation. The  $\text{Ge}_{1-x}\text{Si}_x$  films were prepared by transient heating to  $\sim 1000^\circ\text{C}$  to produce melting and alloying, while the Ge films were produced by heating to  $\sim 700^\circ\text{C}$  to achieve solid-phase epitaxy (SPE).

We have now developed a one-step technique for preparing heteroepitaxial Ge films on Si by deposition of vacuum-evaporated Ge on heated Si substrates. This technique yields mirror-smooth films that are even better in crystal quality than our earlier  $\text{Ge}_{1-x}\text{Si}_x$  and Ge films on Si.

The Si substrates were commercial wafers with  $\langle 100 \rangle$  and  $\langle 111 \rangle$  orientations. They were cleaned with  $5\text{H}_2\text{O}:\text{NH}_4\text{OH}:\text{H}_2\text{O}_2$  solution, rinsed in  $\text{H}_2\text{O}$ , and cleaned with  $6\text{H}_2\text{O}:\text{HCl}:\text{H}_2\text{O}_2$  solution. Each substrate was given a final rinse in dilute ( $\sim 10\%$ ) HF immediately before being

loaded into an oil-diffusion-pumped vacuum system. The substrate was mounted with tungsten clips on a graphite strip that could be heated by passage of AC current. Temperature was controlled by manually adjusting the current and monitored by a thermocouple embedded in the strip. The Ge source was placed in a boron nitride crucible and evaporated with a conventional e-gun. In each experiment, the substrate was heated in about 1 min. to a temperature in the range of 350 to 750°C, a film  $\sim 1500 \text{ \AA}$  thick was deposited at a rate of  $\sim 10 \text{ \AA/s}$ , and the sample was then rapidly cooled to room temperature.

Scanning electron microscope (SEM) observations show that films deposited at substrate temperatures ( $T_s$ ) of 550°C or below are mirror smooth, while those deposited at higher  $T_s$  have rough surfaces. Figures III-4(a) and III-4(b) are the SEM micrographs and RHEED patterns for films deposited on  $\langle 100 \rangle$  Si at  $T_s = 550$  and 650°C, respectively. The (011) RHEED

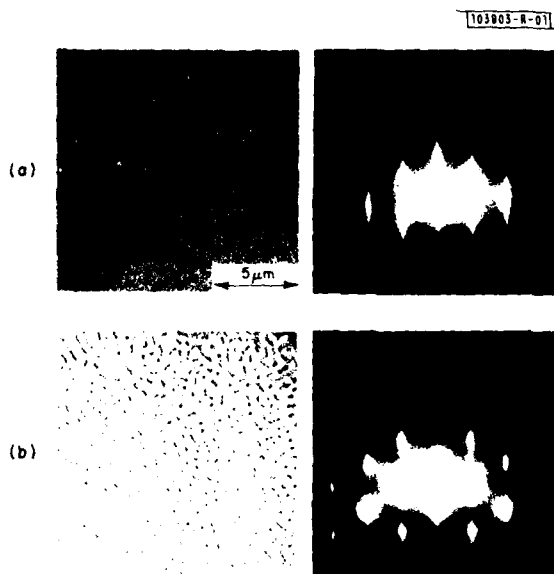


Fig. III-4. SEM micrographs and corresponding RHEED patterns for heteroepitaxial Ge films prepared by vacuum deposition on  $\langle 100 \rangle$  Si at (a)  $T_s = 550^\circ\text{C}$ , (b)  $T_s = 650^\circ\text{C}$ .

pattern of Fig. III-4(a) shows strong elongation of Laue reflections toward the bottom edge of the pattern, indicating a smooth surface. In contrast, the film prepared at  $T_s = 650^\circ\text{C}$  gives a spot pattern [Fig. III-4(b)] with less streaking, as expected for a rough surface, and with faint traces of twin diffraction spots. The RHEED patterns indicate that all the Ge films are epitaxial, even for  $T_s$  as low as 350°C. The roughness of the films deposited at high  $T_s$  values may have been due to oxidation of the substrates or some other contamination.<sup>9</sup>

The crystallographic alignment of the Ge films with respect to their substrates was determined by using an x-ray diffractometer to measure the intensity as a function of angle for the diffraction lines of selected low-index planes. The misalignment angle between a given plane in the film and the same plane in the substrate is designated by  $\theta$  for planes parallel to the

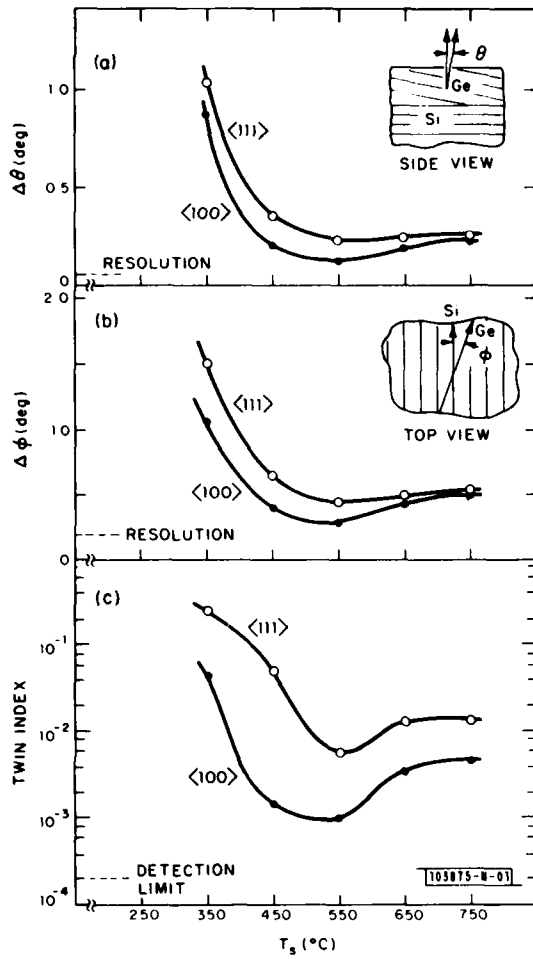


Fig. III-5. Crystallographic parameters (a)  $\Delta\theta$ , (b)  $\Delta\phi$ , and (c) TI (see text) as a function of substrate temperature ( $T_S$ ) for heteroepitaxial Ge films deposited on  $\langle 100 \rangle$  and  $\langle 111 \rangle$  Si substrates.

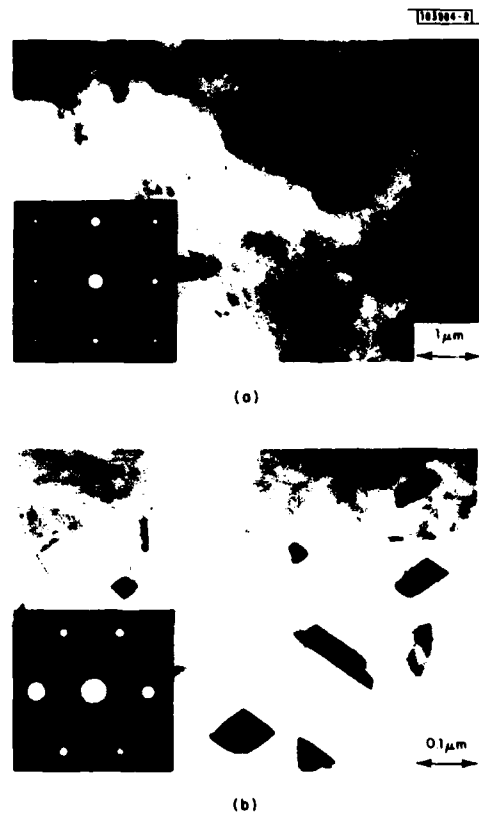


Fig. III-6. TEM micrographs and electron diffraction patterns for a heteroepitaxial Ge film deposited on  $\langle 100 \rangle$  Si at  $T_S = 550^\circ\text{C}$ . (a) Inclined dislocations and  $(100)$  diffraction pattern, (b) twins and  $(411)$  diffraction pattern.

substrate surface and by  $\varphi$  for planes perpendicular to the surface. For the angular positions of the peak intensities of the diffraction lines there is no detectable misalignment (i.e.,  $\theta_{\text{peak}}$  and  $\varphi_{\text{peak}}$  were zero within experimental error). However, there is a significant degree of misorientation within the Ge films, since the widths of their diffraction lines exceed the instrumental resolution. Let the half-width at half-maximum be represented by  $\Delta\theta$  or  $\Delta\varphi$ , respectively. The measured values of these parameters for a number of Ge films are plotted against  $T_s$  in Figs. III-5(a) and III-5(b), respectively. Two major trends are apparent. First, the degree of misorientation is less for films on  $\langle 100 \rangle$ Si than for those on  $\langle 111 \rangle$ Si. Second, with increasing  $T_s$  the values of  $\Delta\theta$  and  $\Delta\varphi$  initially decrease rapidly, reach a minimum at  $T_s = 550^\circ\text{C}$ , and then increase slightly.

An experimental procedure described previously<sup>7</sup> was used to determine the peak intensities of the (311) diffraction lines for the twinned and epitaxial regions of each film. The ratio of these intensities, which we call the twin index (TI), is a measure of the microtwin density. Our detection limit for TI is  $\sim 2 \times 10^{-4}$ , corresponding to a value of  $\sim 6 \times 10^{-4}$  for the volume fraction of twins. The measured values of TI are plotted against  $T_s$  in Fig. III-5(c), which shows that this parameter exhibits the same type of dependence on substrate orientation and temperature as  $\Delta\theta$  and  $\Delta\varphi$ . Thus both misorientation and twinning were minimized by deposition on  $\langle 100 \rangle$ Si substrates at  $550^\circ\text{C}$ . The lowest values obtained for  $\Delta\theta$ ,  $\Delta\varphi$ , and TI are  $0.12^\circ$ ,  $0.28^\circ$ , and  $10^{-3}$ , respectively, which are all better than the values of  $0.25^\circ$ ,  $0.60^\circ$ , and  $10^{-2}$  measured for our best Ge films prepared by SPE.

Growth from the vapor phase generally begins with the formation of discrete nuclei that subsequently grow together to form a continuous film. Misorientation in epitaxial films on single-crystal substrates may arise because the nuclei do not all have the same orientation. As the surface mobility of the deposited atoms increases, the degree to which the nuclei conform to the orientation of the substrate increases, and the degree of misorientation in the films is expected to decrease.<sup>10</sup> For the Ge films, the marked reduction in misorientation and twin density as  $T_s$  is increased from  $350$  to  $550^\circ\text{C}$  can be attributed to the increase in surface mobility with increasing temperature. The observation that the misorientation is less for films on  $\langle 100 \rangle$ Si substrates than for those on  $\langle 111 \rangle$ Si substrates suggests that the surface mobility of Ge atoms is higher on the (100) surface.<sup>11</sup>

As mentioned above, it is difficult to prepare high-quality epitaxial Ge films on Si because of the large mismatch in lattice constant and thermal expansion coefficient. The former mismatch leads to the formation of misfit dislocations, and the latter frequently causes cracking.<sup>12</sup> Microcracks were not detected in our vacuum-deposited Ge films, presumably because the films were too thin for cracking to occur. The mechanical stress arising during cooling was probably released by plastic deformation, which results in the creation of dislocations as well as motion of dislocations already present. Examination of the films by TEM revealed a dense network of misfit dislocations near the Ge-Si interface and some inclined dislocations propagating up toward the Ge surface. The dislocations exhibit extensive interactions, which presumably resulted from the stress-induced motions. Figure III-6(a) shows a TEM micrograph and (100) diffraction pattern for the near-surface region of a Ge film deposited on  $\langle 100 \rangle$ Si at  $T_s = 550^\circ\text{C}$ . The inclined dislocations, which are nearly perpendicular to the film surface, have a density of the order of  $10^8$  lines/cm<sup>2</sup>. Twin lamellae are also present in the film, as shown in the TEM micrograph of Fig. III-6(b).

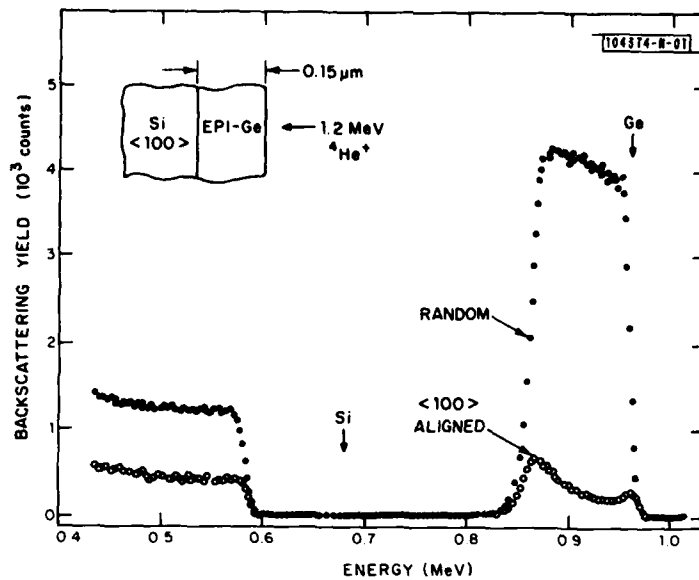


Fig. III-7.  $^4\text{He}^+$  ion channeling spectrum for a heteroepitaxial Ge film deposited on  $\langle 100 \rangle$  Si at  $T_s = 550^\circ\text{C}$ .

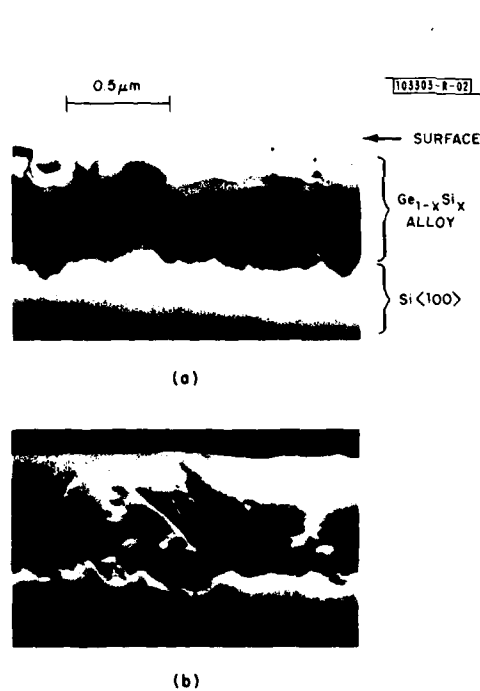


Fig. III-8. (a) Bright-field and (b) dark-field TEM micrographs of a cross section through a  $\text{Ge}_{1-x}\text{Si}_x/\text{Si}$  sample prepared by transient heating.



Fig. III-9. Projection-view TEM micrographs taken at different locations on a foil prepared by thinning down from the sample of Fig. III-8 from the substrate side. The foil thicknesses are (a) 0.2, (b) 0.45, and (c) 0.6  $\mu\text{m}$ .

Ion channeling measurements with 1.2-MeV  $^4\text{He}^+$  ions have been made on several Ge films. Figure III-7 shows the results for one of the best films, which was deposited on  $\langle 100 \rangle$  Si at  $T_s = 550^\circ\text{C}$ . The minimum surface yield is about 4.5 percent, with the yield increasing to 15 percent near the interface. These results, again, are superior to those obtained for our best SPE Ge films.<sup>8</sup>

B-Y. Tsaur    J. C. C. Fan  
M. W. Geis    R. P. Gale

### C. CHARACTERIZATION OF HETEROEPITAXIAL $\text{Ge}_{1-x}\text{Si}_x$ FILMS PRODUCED BY TRANSIENT MELTING

As noted in the preceding section, we have recently prepared heteroepitaxial  $\text{Ge}_{1-x}\text{Si}_x$  alloy films by transient heating of Ge-coated Si single-crystal substrates.<sup>7</sup> These films were characterized primarily by x-ray diffraction and reflection high-energy electron diffraction. Our characterization of the films has now been extended by using transmission electron microscopy and ion channeling to make a detailed study of crystal perfection. The results of this study indicate that dislocations are the principal defects.

The procedure used for preparing heteroepitaxial  $\text{Ge}_{1-x}\text{Si}_x$  alloys has been described previously.<sup>7</sup> Briefly, an amorphous Ge film 0.5  $\mu\text{m}$  thick is deposited by e-beam evaporation on a single-crystal  $\langle 100 \rangle$  Si substrate. The sample is placed on a graphite strip-heater which is then heated to a peak temperature of 950 to 1000 $^\circ\text{C}$  in  $\sim 10$  s and subsequently cooled to room temperature at a rate of 5 to 10 $^\circ\text{C}/\text{s}$ . When the Ge melts, it dissolves a thin layer of the Si substrate to form a molten alloy that crystallizes epitaxially on the substrate during cooling. Auger spectroscopy measurements have shown that the  $\text{Ge}_{1-x}\text{Si}_x$  films formed in this way consist of an upper region with approximately uniform composition and a lower one in which the Ge content gradually decreases to zero at the interface.<sup>7</sup>

The experimental results reported here were obtained for a sample with a  $\text{Ge}_{1-x}\text{Si}_x$  film in which the composition of the uniform region was  $\text{Ge}_{0.72}\text{Si}_{0.28}$ . Figures III-8(a) and III-8(b), respectively, are bright-field and dark-field TEM micrographs of a cross section through the sample. The interface between the film and substrate is seen to be very irregular, with height variations of 0.1 to 0.2  $\mu\text{m}$ . The region of the film just above the interface has a high density of dislocations, while the remainder has a much lower dislocation density although it contains some inclined dislocations that originate in the interfacial region and extend toward the surface. There is a rather smooth, well-defined boundary between the regions of high and low dislocation density, which probably correspond to the regions of graded and uniform alloy composition, respectively.

To obtain quantitative data on dislocation density, a portion of the sample was thinned down from the substrate side to form a thin foil for TEM examination in the projection view. Figures III-9(a), III-9(b), and III-9(c) are bright-field micrographs of this foil taken at three different locations, where the foil thickness is estimated from extinction fringe measurements to be 0.2, 0.45, and 0.6  $\mu\text{m}$ , respectively. From Figs. III-9(a) and III-9(b), the total projected dislocation line length per unit area of the  $\text{Ge}_{1-x}\text{Si}_x$  film is estimated to be  $3.6 \times 10^5$  and  $1.2 \times 10^6 \text{ cm}^{-1}$ , respectively. The dislocation line length per unit volume is about twice as great for the portion of the film lying between 0.2 and 0.45  $\mu\text{m}$  below the surface as it is for the portion between the surface and a depth of 0.2  $\mu\text{m}$ . Both portions lie within the region of low dislocation density. At the location of the micrograph shown in Fig. III-9(c) the foil extends to the interfacial region between the alloy film and the Si substrate. Because of the dense

dislocation network in this region, areas of the TEM image are almost opaque, precluding a reliable estimate of the overall dislocation density. Presumably the dislocations in the interfacial region are misfit dislocations<sup>13</sup> that result from the lattice mismatch between the  $\text{Ge}_{1-x}\text{Si}_x$  alloy and Si.

To complement the TEM study, we also investigated the dislocation distribution by means of Rutherford backscattering experiments. In these experiments, which were performed before the film was thinned for TEM examination, backscattering spectra of  $^4\text{He}^+$  ions with energies of 0.75 to 2.0 MeV were measured for random incidence and for incidence in the  $\langle 100 \rangle$  axial channeling direction. The 2.0-MeV spectra are shown in Fig. III-10. The random spectrum

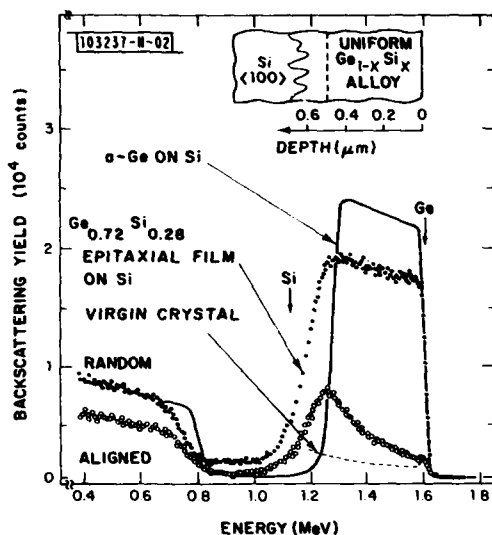


Fig. III-10. Random and  $\langle 100 \rangle$  axial channelled backscattering spectra obtained with  $^4\text{He}^+$  ions for the sample of Fig. III-8 before and after transient heating. The dashed curve is the simulated  $\langle 100 \rangle$  channeling spectrum for a virgin  $\text{Ge}_{0.72}\text{Si}_{0.28}$  crystal.

obtained for the initial amorphous-Ge/Si sample is represented by the solid line, while the random and channeling spectra measured after formation of the  $\text{Ge}_{1-x}\text{Si}_x$  film are represented by closed and open circles, respectively. Comparison of the random spectra obtained before and after heating shows that the region of uniform composition adjacent to the surface extends to a depth of about 0.5  $\mu\text{m}$ .

To evaluate the dislocation density in the alloy film as a function of depth, we have analyzed the channeling spectrum by using the method of Picraux and coworkers,<sup>14,15</sup> who found that dislocations produce enhanced dechanneling by distortion of the lattice plane with little direct backscattering. On the assumption that dechanneling is additive, for negligible direct scattering the relationship between the channeling yield  $\chi_D$  of a disordered crystal at depth  $z$  and the yield  $\chi_V$  of a virgin crystal at the same depth is given by the expression<sup>14</sup>

$$\int_0^z n_D(z') dz' = -\frac{1}{\lambda} \ln \left( \frac{1 - \chi_D(z)}{1 - \chi_V(z)} \right) \quad (\text{III-1})$$

where  $n_D(z')$  is the density of defects at  $z'$  with a dechanneling cross section  $\lambda$ . If the defects are dislocations, the integral on the left side of Eq. (III-1) gives the total projected length of dislocation lines per unit area,  $N_D(z)$ , for the portion of the film between the surface and  $z$ . In this case the appropriate cross section<sup>16</sup> for the  $\text{Ge}_{0.72}\text{Si}_{0.28}$  film is

$$\lambda_a(\text{\AA}) \approx 21 E^{1/2}$$

where  $E$  is the energy of the incident ions in MeV.

In order to use Eq. (III-1) for determining  $N_D(z)$  from the channeling data for the  $\text{Ge}_{0.72}\text{Si}_{0.28}$  film, it is necessary to evaluate  $\chi_V(z)$  by comparing the channeling spectrum for a virgin crystal with the random spectrum measured for this composition. For each value of  $E$  used in the experiments, we have therefore calculated a virgin channeling spectrum by measuring the channeling spectra for  $\langle 100 \rangle$  single-crystal wafers of Ge and Si, then taking an appropriately weighted linear average. The simulated channeling spectrum obtained in this manner for  $E = 2.0$  MeV is shown by the dashed line in Fig. III-10. For this spectrum, the minimum value of  $\chi_V$  is close to 4 percent, compared with the minimum value of 8 percent measured for  $\chi_D$  of the  $\text{Ge}_{0.72}\text{Si}_{0.28}$  film.

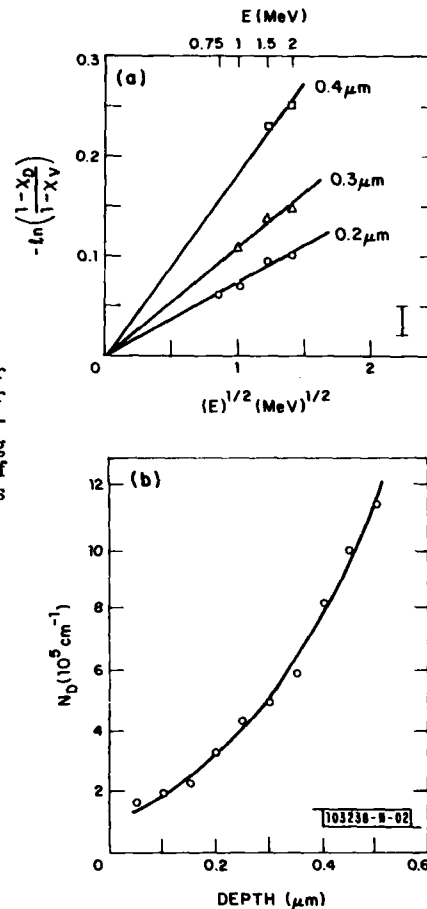


Fig. III-11. (a) Dechanneling parameter vs square root of  $^4\text{He}^+$  ion energy for three film depths. The error bar indicates the uncertainty due to counting statistics. (b) Total projected length of dislocation lines per unit area ( $N_D$ ) vs depth.

If the defects responsible for dechanneling are dislocations, the logarithmic term on the right side of Eq. (III-1) will be equal to  $(-\lambda_a N_D)$ . Due to the energy dependence of  $\lambda_a$ , for a fixed value of  $z$  this logarithmic term (called the dechanneling parameter) will be proportional to  $E^{1/2}$ . To test the applicability of Eq. (III-1) to the alloy film, we have plotted the measured values of the dechanneling parameter as a function of  $E^{1/2}$  for  $z = 0.2, 0.3,$  and  $0.4 \mu\text{m}$ , as shown in Fig. III-11(a). In each case, the data fit a straight line through the origin, as predicted. We

have therefore employed Eq. (III-1) to determine  $N_D(z)$  for the alloy film from the channeling data for 2-MeV ions. The values obtained for  $N_D$  are plotted against depth in Fig. III-11(b). The values at 0.2 and 0.45  $\mu\text{m}$  are  $3 \times 10^5$  and  $9.5 \times 10^5 \text{ cm}^{-1}$ , respectively, in good agreement with the values of  $3.6 \times 10^5$  and  $1.2 \times 10^6 \text{ cm}^{-1}$  found by TEM examination. From Eq. (III-1), the dislocation line length per unit volume,  $n_D$ , is the slope of the  $N_D$  curve in Fig. III-11(b). The values of  $n_D$  obtained in this manner increase from  $5 \times 10^9 \text{ cm}^{-2}$  near the surface of the film to  $4 \times 10^{10} \text{ cm}^{-2}$  at  $z = 0.5 \mu\text{m}$ .

B. Y. Tsaur  
J. C. C. Fan

#### REFERENCES

1. For example, S. S. Lau, S. Matteson, J. W. Mayer, P. Revesz, J. Gyulai, J. Roth, T. W. Sigmon, and T. Cass, *Appl. Phys. Lett.* **34**, 76 (1979); W. E. Ham, M. S. Abrahams, C. J. Buicchi, and J. Blane, *J. Electrochem. Soc.* **124**, 634 (1977).
2. M. Tamura, H. Tamura, and T. Tokuyama, *Jpn. J. Appl. Phys.* **19**, 123 (1980).
3. H. W. Lam, R. F. Pinizzotto, and A. F. Fasch, Jr., Abstract 481, The Electrochemical Society Extended Abstracts, Hollywood, Florida, October 5-10, 1980, p. 1198.
4. R. W. McClelland, C. O. Bozler, and J. C. C. Fan, *Appl. Phys. Lett.* **37**, 560 (1980).
5. See for example, A. G. Milnes and D. L. Feucht, *Heterojunctions and Metal-Semiconductor Junctions* (Academic Press, New York, 1972), Chap. 9.
6. J. C. C. Fan, G. W. Turner, R. P. Gale, and C. O. Bozler, Proc. Fourteenth IEEE Photovoltaic Specialists Conference - 1980, San Diego, California, 7-10 January 1980, pp. 1102-1105, DTIC AD-A090668.
7. J. C. C. Fan, R. P. Gale, F. M. Davis, and G. H. Foley, *Appl. Phys. Lett.* **37**, 1024 (1980).
8. B-Y. Tsaur, J. C. C. Fan, and R. P. Gale, *Appl. Phys. Lett.* (in press).
9. G. O. Krause, *Phys. Stat. Sol. (a)* **2**, 901 (1970).
10. See, for example, J. A. Venables and G. I. Price in *Epitaxial Growth*, J. W. Matthews, Ed. (Academic Press, New York, 1975), Chap. 4.
11. I. R. Weisberg, *J. Appl. Phys.* **38**, 4537 (1967).
12. J. Pfeifer, I. Varga, and B. Szentpali, *Thin Solid Films* **11**, 59 (1972).
13. J. H. van der Merwe, *J. Appl. Phys.* **34**, 117 (1963).
14. S. T. Picraux, E. Rimini, G. Foti, and S. U. Campisano, *Phys. Rev. B* **18**, 2078 (1978).
15. S. T. Picraux, D. M. Follstaedt, P. Baeri, S. U. Campisano, G. Foti, and E. Rimini, *Rad. Effects* **49**, 75 (1980).
16. Y. Quere, *Phys. Status Solidi A* **30**, 713 (1968).

## IV. MICROELECTRONICS

### A. CHARGE-COUPLED DEVICES: SAW TIME-INTEGRATING CORRELATOR WITH CCD READOUT

We have earlier<sup>1,2</sup> described a time-integrating correlator in which the multiplication and integration of many samples of two wideband surface-acoustic-wave (SAW) inputs take place in a charge-coupled device (CCD). We have also described a scheme using a second CCD chip as an analog delay line for cancellation of fixed-pattern noise which improved the dynamic range of this device to 40 from 20 dB (Ref. 3). This scheme has now been used in the evaluation of device performance for the correlation of 20-MHz-bandwidth spread-spectrum signals buried in band-limited Gaussian noise.

Figure IV-1 shows the CCD output after integrating for 200  $\mu$ s. Figure IV-1(a) is the full 3.5- $\mu$ s correlation window available in the CCD, and Fig. IV-1(b) is an expanded view of the correlation peak. The excellent linearity of the correlator is demonstrated by attenuating the input signal by 20 dB (Fig. IV-2) and noting that the correlation output is almost exactly 20 dB smaller than the peak in Fig. IV-1.

The signal-processing gain of this device should be less than  $10 \log (200 \mu\text{s} \times 20 \text{ MHz}) = 36$  dB. We have achieved a signal-processing gain in excess of 30 dB as illustrated in Fig. IV-3, where a correlation peak well above the output noise is obtained with an input signal-to-noise ratio of -30 dB. A processing gain so close to the theoretical maximum was achieved by reducing the device noise to a level below the noise at the output contributed by the Gaussian noise introduced at the input.

The noise floor of the device as shown in Fig. IV-4 is about 3 mV peak-to-peak, which corresponds to 0.5 mV rms. The correlation peak in Fig. IV-1 is 120 mV, yielding a dynamic range of  $20 \log (120/0.5) = 48$  dB.

We have operated this device with integration times up to 10 ms, which indicates that even higher processing gains could be achieved if the device noise could be further reduced. The residual noise, as shown in Fig. IV-4, was determined to be thermal noise in the CCD. It

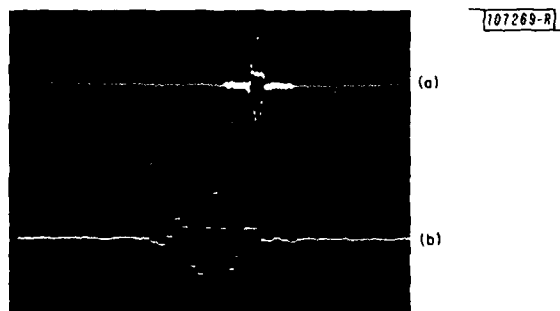
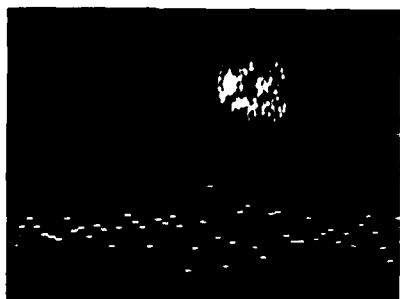


Fig. IV-1. (a) Correlator output for phase-encoded signals with 20-MHz bandwidth on an input carrier frequency of 103 MHz. (b) Expanded view of correlation peak. Signal and noise power are both 24 dBm; 100 mV/division.



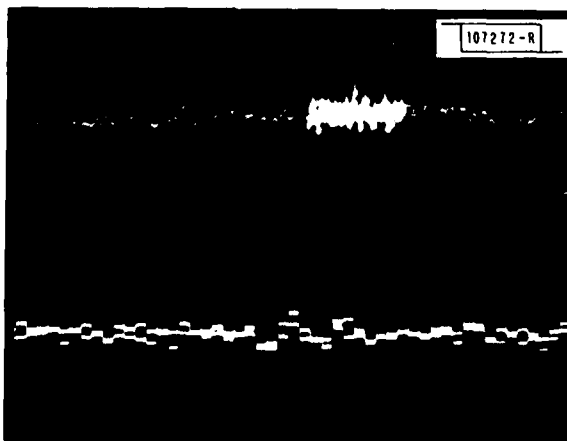
107270-R

Fig. IV-2. Correlator output with signal attenuated 20 dB and oscilloscope gain increased 20 dB. The input signal-to-noise ratio is -20 dB.



107271-R

Fig. IV-3. Correlator output with an input signal-to-noise ratio of -30 dB.



107272-R

Fig. IV-4. Correlator output with no external noise. The input signal is -16 dBm, 43 dB below the 1-dB compression point of the SAW delay line; 5 mV/division.

should be possible to reduce this noise another 10 dB or so by using the low-noise CCD design techniques developed for low-light-level imaging devices.<sup>4</sup> A dynamic range of 58 dB would support a processing gain of 48 dB, which would require a 3-ms integration time for 20-MHz bandwidth signals. This integration time is well within the capability of the current device.

D. L. Smythe

## B. CHARGE-COUPLED DEVICES: IMAGERS

The goal of the CCD imager work for the GEODSS (Ground-based Electro-Optical Deep Space Surveillance) Program is a focal-plane mosaic consisting of five 100- × 400-element CCD imager chips mounted on a hybrid substrate. In the past year, we have assembled three such 5-chip focal planes in which the chips are mounted with positional accuracies of 3 to 6  $\mu\text{m}$ . In this report we review the procedures we have developed for assembling these focal planes.

The multi-chip focal plane described here was developed for the Space Surveillance Group to be used in an advanced MTI (moving-target indicator) sensor system for satellite surveillance. The system concept, described in Fig. IV-5, uses a column of TDI (time-delay and integration) CCD imagers. The sensor is mounted on the focal plane of a telescope, and the telescope is scanned continuously across the sky. For proper TDI operation, the columns of the CCDs are aligned parallel to the star-image motion, and the CCD clock rate is adjusted to synchronize charge-packet motion to the image motion. The chips are equally spaced in the scan direction so that the image transit time,  $T$ , which is the time for the image to travel between the same pixel row on two adjacent chips, is the same for all pairs of adjacent chips. The video signals from each chip are delayed by an amount shown in Fig. IV-5 and analyzed by the signal processor. Under these conditions the video signals from a star would appear simultaneously on all the inputs to the processor, and signals from an object moving with respect to the star background would not. Thus moving objects can be distinguished by the processor from the star background.

A photograph of a 5-chip focal plane is shown in Fig. IV-6. The substrate design allows for three columns with five devices per column to allow wide scan coverage, but the current program goal is to demonstrate system performance with a single column. The substrate is a 5.3- × 5.3-cm, polished alumina blank with two levels of aluminum metallization isolated by a layer of  $\text{SiO}_2$ . The fabrication procedures for the substrate have been described in a previous report.<sup>5</sup> Components on the substrate other than the CCDs include an emitter-follower circuit for each CCD, decoupling capacitors for critical DC lines, and back-to-back Zener diodes for gate protection.

The CCD chips must be mounted on the focal plane with a high degree of positional accuracy in order for the MTI processing to be effective. In a previous report,<sup>6</sup> some initial results of high-precision chip placement were described. Here we will describe further details of the procedure and results on recently assembled focal planes. The precision placement of the chips is performed using a coordinate measuring machine, which is an instrument normally used for dimensional measurements of machined parts. This instrument has been modified for our purpose by mounting a vacuum collet (to hold the chips) and a microscope on the measuring arm. The location of this arm in the x-y (horizontal) plane is displayed on digital readout to an accuracy of approximately 3  $\mu\text{m}$ . Figure IV-7 is a photograph showing a multichip substrate, the vacuum collet, and a portion of the microscope. A chip ready for mounting can be seen on the micrometer-controlled x-y positioner. The chip is abutted to three locating pins to establish its initial location. In order to measure its starting coordinates, the operator views the chip through the

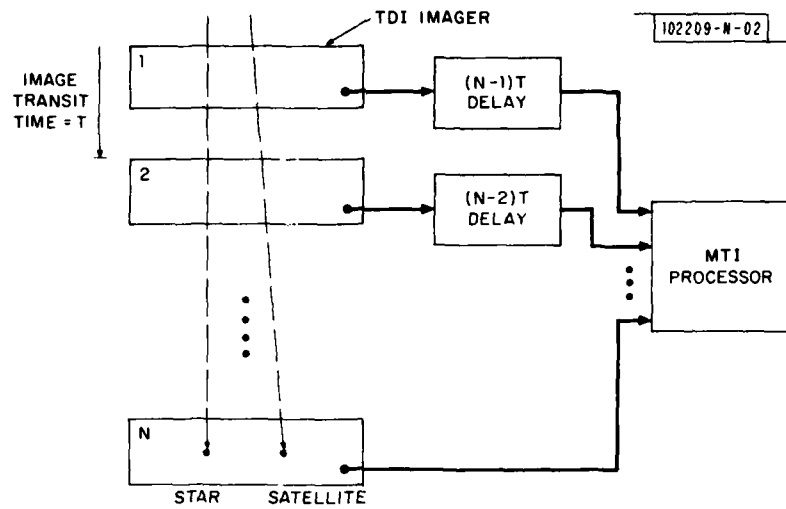


Fig. IV-5. MTI system concept using multiple TDI CCD imagers. System is to be used for detection of satellites against a star background.

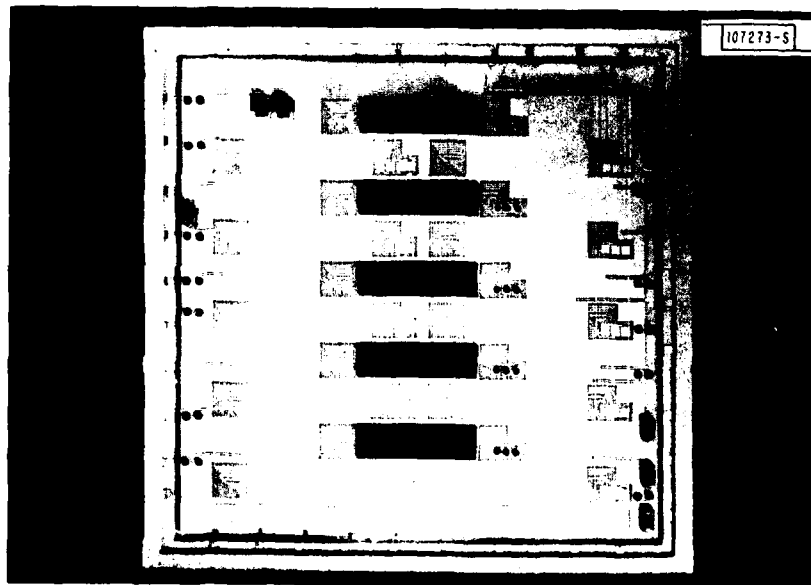


Fig. IV-6. Photograph of a 5-chip CCD hybrid sensor.

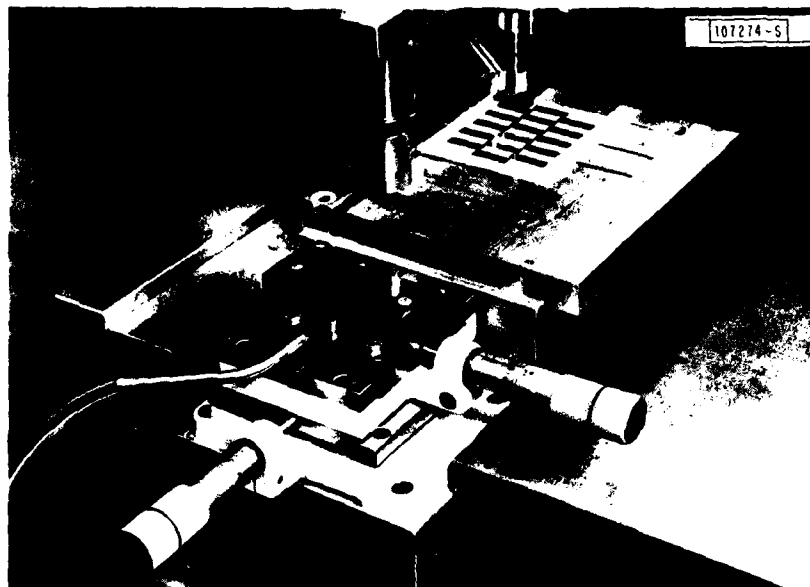


Fig. IV-7. Photograph of the system used for precision mounting of the imager chips on a substrate.

microscope and registers a hairline in the eyepiece with alignment marks on the chip. The x-y positioner may then be adjusted to bring the coordinates of each chip to a common starting location. This is seldom necessary, however, because the chips have been cut from the wafer by a precision diamond saw with careful attention to achieving a given spacing between the chip edges and the alignment marks. The chip is then picked up by the collet, moved to its intended location, and attached by means of a quick-setting adhesive.

The accuracy of the chip placement is measured optically using a Nikon Profile Projector whose x-y stage has been equipped with digital micrometers. These micrometers have a resolution of  $1.27 \mu\text{m}$  (0.00005 in.). The measurement accuracy of this instrument was determined by comparing our measurements on a test pattern with those of the Bureau of Standards, and the results show an accuracy within the micrometer resolution over distances used in measuring the focal plane.

In measuring the chip locations we are concerned with x, y, and angular displacements. The difference in y-coordinates at the right and left edges of the chip determines the angular displacement error. For all the chips, this difference has been measured to be within the  $1.27\text{-}\mu\text{m}$  resolution of the micrometer; this demonstrates a rotational error of less than 0.1 mrad or 0.006 deg.

The x- and y-positional errors are determined by measurements of x- and y-alignment marks on each chip relative to chip number 1 (the chips are numbered 1 through 5 starting at the top of the column). The x- and y-alignment marks are created by the masking layers which determine the pixel locations, namely, channel stop for the x-location and first polysilicon for the y-location. To help visualize the measured errors, we have plotted in Fig. IV-8 the results of the x- and y-measurements for a recent focal-plane imager. Ideally the y-location of each

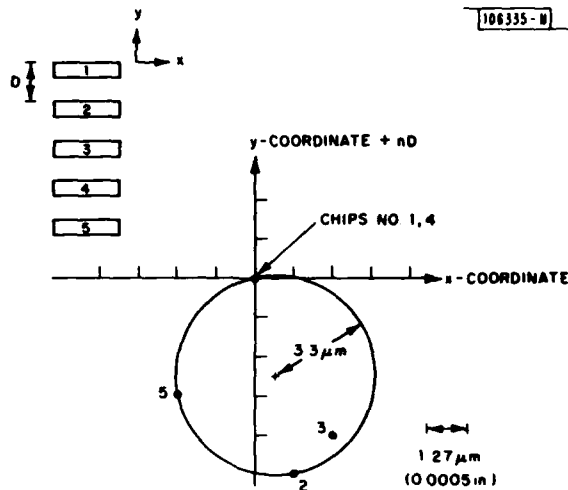


Fig. IV-8. Results of position measurements of five CCD chips on a focal-plane imager. The measurement resolution is  $1.27 \mu\text{m}$  ( $0.00005 \text{ in.}$ ).

chip differs from the chip above it by  $0.360 \text{ in.}$  Therefore, we add  $0.360(n-1)$  to the  $y$ -measurement of chip  $n$  to obtain the plot of Fig. IV-8. We then interpret each point in the figure as the location of a pixel on that chip relative to its intended location with respect to chip 1.

The true positional accuracy, however, is not based on any one chip as the standard but rather on the relative positions of the chips. On that basis we draw the smallest circle which encompasses the data points, and conclude that the radius of this circle is the maximum positional error of any pixel of the focal plane. For the data in Fig. IV-8 this is  $3.3 \mu\text{m}$ , and for two other focal planes the results are  $6.3$  and  $3.6 \mu\text{m}$ . These values are small in comparison with the CCD pixel size of  $30 \times 30 \mu\text{m}$ , and are well within the requirements of the MTI system.

P. J. Daniels  
B. E. Burke  
W. H. McGonagle

#### C. COOLED LOW-NOISE GaAs MONOLITHIC MIXERS AT 110 GHz

In a previous report,<sup>7</sup> we described the fabrication of a GaAs monolithic-integrated-circuit mixer module which had an uncooled double-sideband (DSB) mixer noise temperature of  $339 \text{ K}$  and a conversion loss of  $3.8 \text{ dB}$  at  $110 \text{ GHz}$ . Considerable reduction in system noise temperature is expected when cooling mixers<sup>8,9</sup> to liquid-nitrogen temperature, and this monolithic mixer module has shown a DSB mixer noise temperature of  $50 \text{ K}$  and conversion loss of  $4.5 \text{ dB}$  when cooled to  $77 \text{ K}$ . We believe this is the lowest noise temperature ever reported for any mixer at  $110 \text{ GHz}$ .

The mixer module, mounted in the end of a waveguide horn, is attached to a liquid-nitrogen cold finger inside a vacuum dewar. Low-loss beam optics and a quasi-optical diplexer are used to combine signal and local-oscillator energy into a single beam, and an off-axis parabolic mirror is used to focus the beam energy through a low-loss quartz window in the dewar wall

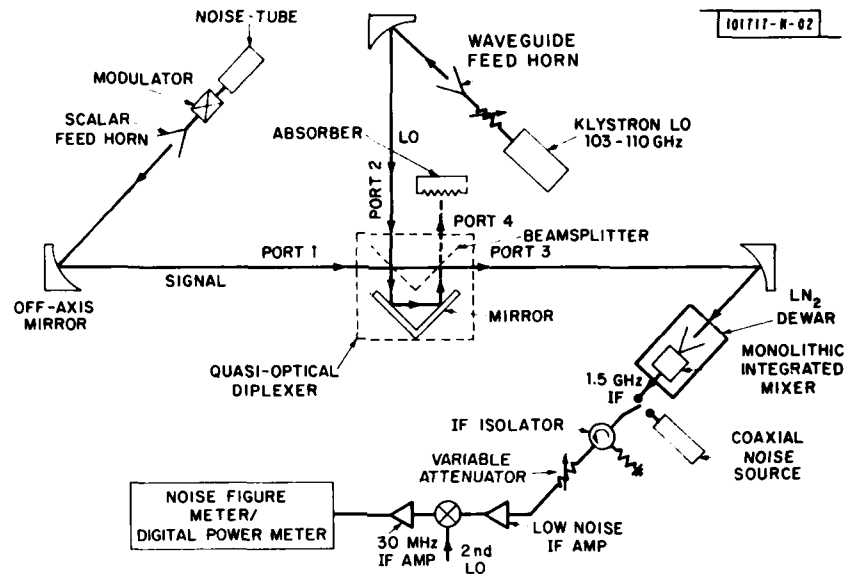


Fig. IV-9. Quasi-optical receiver for noise figure and conversion loss measurements.

into the waveguide horn (Fig. IV-9). In the noise measurement, the output of a calibrated noise tube is coupled through a ferrite modulator and scalar feed horn to produce a quasi-optical Gaussian beam of noise energy at port 1 of the diplexer. Switching the noise energy beam on and off allows one to measure the system Y-factor directly by a digital power meter at the output of the 30-MHz IF amplifier. Measurements of the system Y-factor as a function of IF noise figure are made by inserting attenuators between the IF isolator and the low-noise IF amplifier. This allows calculation of both the DSB mixer noise temperature and conversion loss. The noise tube is calibrated against room temperature and 77 K absorber loads, which are inserted into the signal path at port 1 of the diplexer in place of the noise-tube energy beam.

Several monolithic mixer modules have been cooled to 77 K and have shown DSB mixer noise temperatures in the range 50 to 200 K and conversion losses of 4.0 to 5.0 dB. Mixer performance appears to depend on material quality, the presence of epitaxial material which has not been converted to high resistivity, and module thickness. The effects of these and other parameters on mixer performance are being investigated. The mixers are rugged and can be cycled between room and liquid-nitrogen temperatures repeatedly with no change in characteristics. The mixers have an inherently large RF bandwidth and the potential for low-cost mass production, and they should be scalable to higher frequencies.

B. J. Clifton      W. J. Piacentini  
G. D. Alley        I. H. Mroczkowski  
R. A. Murphy      W. Macropoulos

#### D. A MODEL FOR THE LATERAL EPITAXIAL OVERGROWTH OF SILICON ON $\text{SiO}_2$

The growth of epitaxial Si on amorphous substrates has become a phenomenon of scientific and technological importance. Recently we reported<sup>10</sup> the lateral growth of up to 5.5  $\mu\text{m}$  of single-crystal Si over the edge of a thin ( $<0.03 \mu\text{m}$ )  $\text{SiO}_2$  bar structure on a single-crystal silicon substrate using the reduction of  $\text{SiH}_4$  in  $\text{H}_2$ . For identical deposition conditions (e.g., temperature,  $\text{SiH}_4$  partial pressure, etc.), the extent of lateral growth was found to be strongly dependent

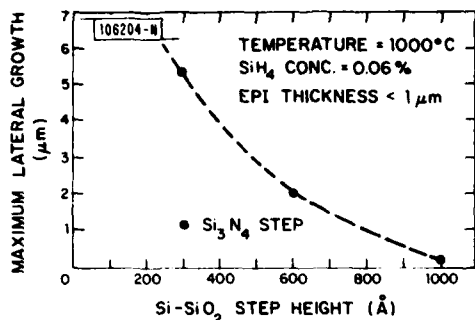


Fig. IV-10. Maximum lateral growth vs Si-SiO<sub>2</sub> step height.

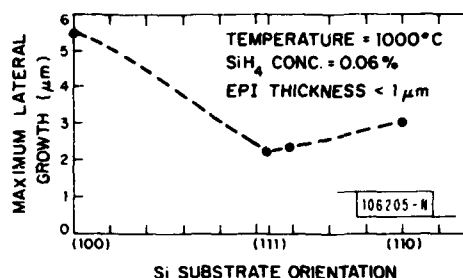


Fig. IV-11. Maximum lateral growth vs Si-substrate orientation.

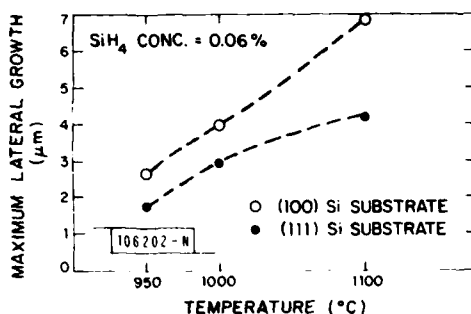


Fig. IV-12. Maximum lateral growth vs epitaxial growth temperature.

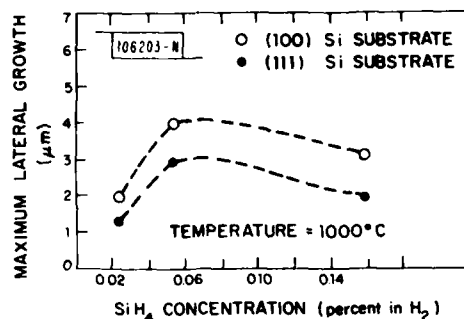


Fig. IV-13. Maximum lateral growth vs SiH<sub>4</sub> concentration.

on both the Si-SiO<sub>2</sub> step height (SiO<sub>2</sub> bar thickness) and the Si substrate orientation (as shown in Figs. IV-10 and -11).

In recent experiments we have determined the dependence of the lateral growth on temperature and SiH<sub>4</sub> concentration. These results are shown in Figs. IV-12 and -13 and can be explained by the differences in the heterogeneous nucleation of Si on the two substrate materials, amorphous SiO<sub>2</sub> and single-crystal Si. A surprising observation is that the lateral-to-vertical growth ratio can be made significantly larger than one – as high as nine or ten for a recessed oxide – when both lateral and vertical growth directions are (100). This result is clear from the data of Figs. IV-10 and -11, where the epitaxial thickness can be easily determined. Conversely, this ratio can be made less than one by significantly decreasing the exposed Si-to-SiO<sub>2</sub> surface ratio (all other conditions being equal).

The explanation for these phenomena is based on a consideration of the adsorption of SiH<sub>4</sub> at the substrate surface. According to Bloem,<sup>11</sup> surface reactions at relatively high temperatures (>900°C) are sufficiently rapid so that epitaxial growth rates are controlled by gas-phase diffusion of the Si-source gas to and from the substrate surface. The driving force for epitaxial growth under these conditions is the difference in the SiH<sub>4</sub> partial pressure in the bulk of the gas and at the growing surface. Nucleation and subsequent epitaxial growth on the Si substrate begin almost immediately in the presence of SiH<sub>4</sub>. However, there is an incubation period for Si nucleation on the SiO<sub>2</sub> surface. Thus SiH<sub>4</sub> in the gas phase will be strongly depleted above the

Si surface but not above the  $\text{SiO}_2$  surface. If the growing Si layer reaches the upper edge of the  $\text{SiO}_2$  surface before nucleation has commenced on this surface, a large partial pressure gradient in a lateral direction across the wafer from the  $\text{SiO}_2$  toward the growing Si area will be created and lateral growth will proceed.

If this lateral gradient is in excess of the partial pressure gradient in the vertical direction, one would expect to observe a lateral-to-vertical growth ratio greater than one. Additionally, once polysilicon nucleation on the  $\text{SiO}_2$  surface commences, the level of  $\text{SiH}_4$  in the gas phase above the  $\text{SiO}_2$  surface drops, nearly eliminating the lateral partial-pressure gradient and ultimately the lateral growth. Therefore, in order to maximize the lateral-to-vertical-growth ratio one needs to select the temperature,  $\text{SiH}_4$  partial pressure, etc., which result in the largest lateral-partial-pressure gradient of  $\text{SiH}_4$  and the longest incubation period.

D. D. Rathman  
D. J. Silversmith  
J. A. Burns (Group 23)

#### E. PROPERTIES OF W-GaAs SCHOTTKY BARRIERS AFTER HIGH-TEMPERATURE ANNEAL

The properties of tungsten films deposited on GaAs have been determined as a function of annealing temperature in the range 500 to 850°C. The dependence of sheet resistance on annealing temperature and the results of Auger analyses will be discussed, and electrical measurements made on Schottky barriers formed from these annealed tungsten films on n-type epitaxial GaAs will be analyzed.

The samples for measuring the sheet resistance of annealed tungsten films were prepared by depositing a 300-Å-thick film of tungsten using electron-beam evaporation on a semi-insulating GaAs substrate. Sections of this substrate were annealed for 20 min. inside a GaAs epitaxial reactor with a palladium-purified hydrogen atmosphere at temperatures from 150° to 850°C. In Fig. IV-14, the sheet resistance vs annealing temperature is plotted. The lowest sheet resistance ( $10.5 \Omega/\square$ ) is obtained for an anneal at 750°C and is only 3.5 times the theoretical lower limit calculated by correcting the bulk resistivity for the increased resistance due to surface scattering. For anneals above 750°C, the resistivity begins to increase and becomes too large for our measuring instrumentation after an 850°C anneal. Since the resistivity of tungsten films on oxidized silicon wafers continues to decrease for anneals above 800°C,<sup>12,13</sup> a reaction between the tungsten and gallium arsenide is occurring. The Auger analysis reported below confirms this reaction for anneals of 800° and 850°C.

Samples for Auger analysis were prepared as above. A comparison of an as-deposited 300-Å-tungsten film on GaAs with a tungsten film on GaAs annealed at 550°C is shown in Fig. IV-15. The Auger electron spectroscopy (AES) profile of the as-deposited tungsten indicates a significant amount of oxygen incorporated during evaporation. The AES profile of the tungsten film annealed at 550°C shows that the oxygen has diffused out of the tungsten to a level below the detection limits of Auger analysis. This decrease in the oxygen concentration is one of the factors contributing to the decreasing resistance seen in Fig. IV-14. The tungsten signal in the GaAs for the 550°C annealed tungsten film has the same profile as the tungsten signal for the unannealed tungsten film, indicating no diffusion within the limits of the Auger analysis.

The AES profiles of tungsten films annealed from 550° to 750°C are identical. However, at 800°C there appears to be some interdiffusion between the tungsten and GaAs as shown in

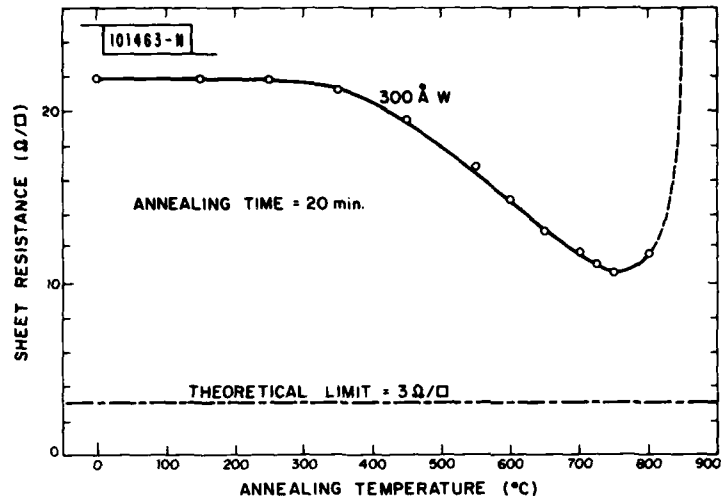


Fig. IV-14. Sheet resistance of 300-Å-W film for various annealing temperatures.

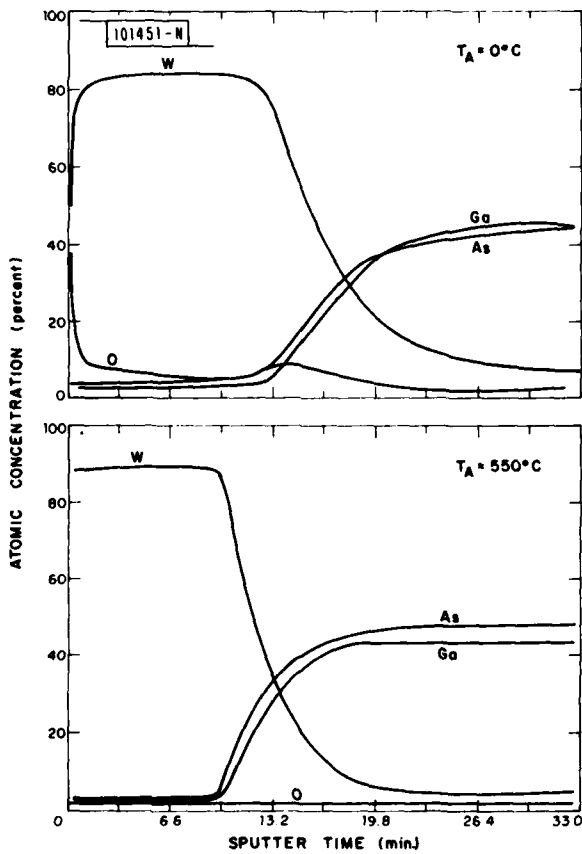


Fig. IV-15. AES profile of tungsten on GaAs.

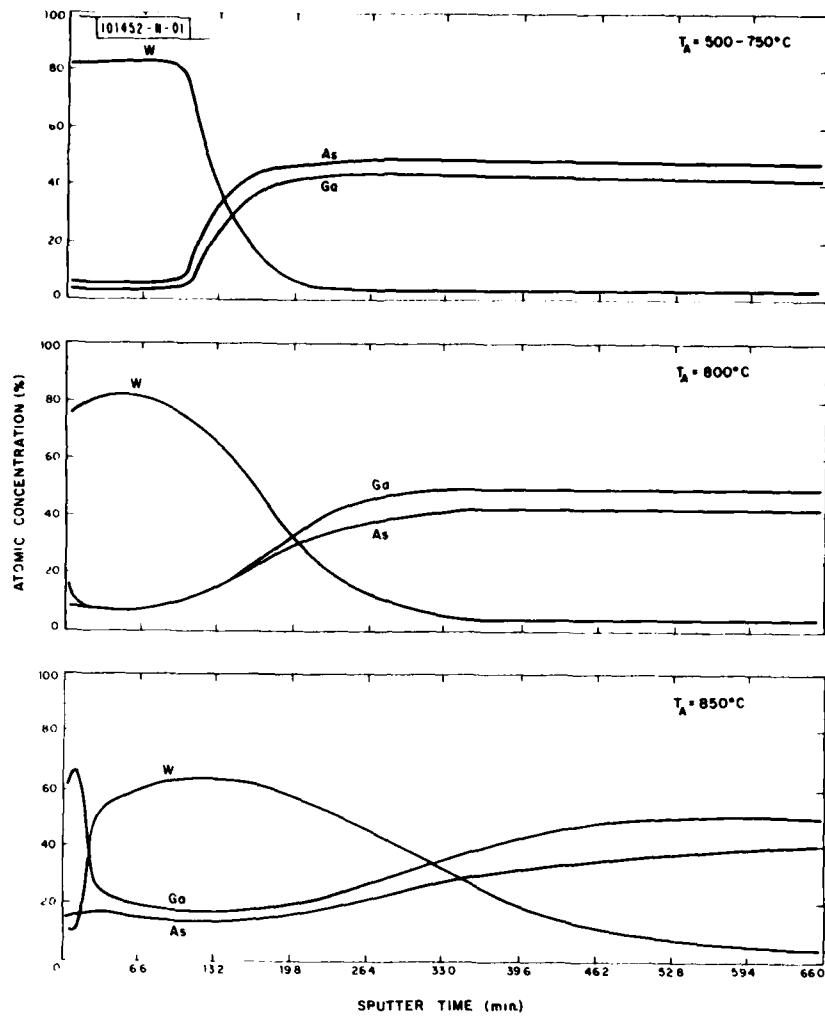


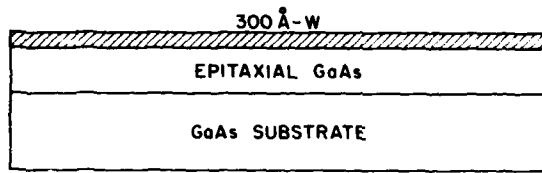
Fig. IV-16. AES profiles of annealed tungsten and GaAs.

Fig. IV-16. This corresponds to the rise in the sheet resistance after annealing the tungsten film at  $800^\circ\text{C}$ . After annealing the tungsten film at  $850^\circ\text{C}$ , there is complete interdiffusion of the gallium arsenide and tungsten, and no metal-semiconductor interface.

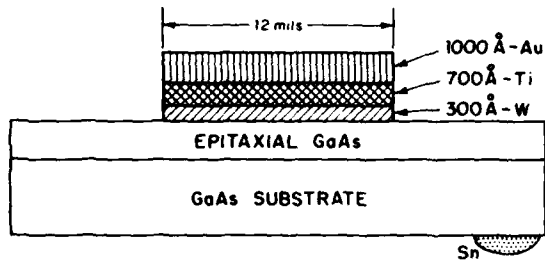
Samples for measuring the electrical properties of W-GaAs Schottky barriers were prepared by first growing n-type epitaxial layers with a doping concentration from  $5 \times 10^{15} \text{ cm}^{-3}$  to  $2 \times 10^{17} \text{ cm}^{-3}$  on Si-doped,  $n^+$  substrates. A  $300\text{-\AA}$ -thick tungsten film was then electron beam evaporated on the epitaxial layers and annealed. The annealed sample had tungsten covering the surface of the epitaxial layer as shown in Fig. IV-17(a). The anneals were 20 min. in duration over the temperature range  $550^\circ$  to  $850^\circ\text{C}$ . After annealing, a titanium/gold/titanium composite film was sputtered over the tungsten film, and the gold, titanium, and tungsten were etched, leaving the 12-mil discs shown in Fig. IV-17(b). The ohmic contact was made by alloying tin spheres to the  $n^+$ -substrate.

The average ideality factor for each sample annealed in the temperature range  $550^\circ$  to  $800^\circ\text{C}$  is shown in Fig. IV-18. The dashed curves below  $400^\circ\text{C}$  are flat because the ideality factor of

101462-N-01



(a)



(b)

Fig. IV-17. Structures for annealing and electrical measurements: (a) anneal structure and (b) electrical measurement structure.

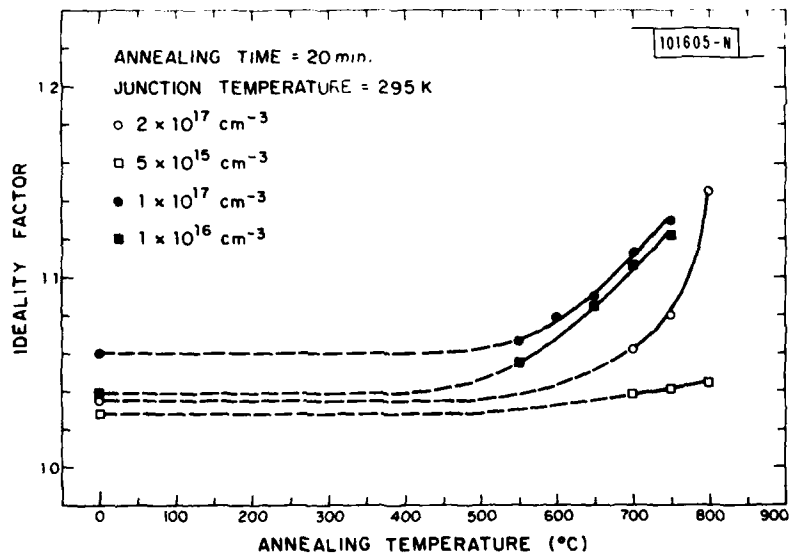


Fig. IV-18. Ideality factor of W-GaAs Schottky barriers for various annealing temperatures.

W-GaAs Schottky barriers is independent of the annealing temperature for anneals of 400°C or lower.<sup>14,15,16</sup> The dashed curves for anneals above 400° are smooth transitions to the first data point.

Although the ideality factor is expected to be higher for heavier doped n-type epitaxial layers, this is not the case for our data. We believe this to be caused by the tungsten film represented by the solid circles and solid squares having a higher as-deposited sheet resistance than the tungsten film represented by open circles and open squares. This higher resistance indicates more impurities in the tungsten film. The ideality factors on the  $5 \times 10^{15} \text{ cm}^{-3}$  layer are the lowest to be reported for any metal annealed at these temperatures on GaAs.

The equations used to calculate the barrier height from I-V data for Schottky barriers on GaAs are given by thermionic-emission theory.<sup>17</sup> According to this theory

$$J = J_s (e^{qV/kT} - 1)$$

and

$$J_s = AT^2 e^{-q\phi/kT}$$

where  $J$  is the current density,  $V$  is the voltage across the junction,  $k$  is the Boltzmann constant,  $T$  is the temperature of the junction,  $\phi$  is the barrier height, and  $A$  is the Richardson constant. By calculating  $J_s$  for various temperatures and then plotting  $\log(J_s/T^2)$  vs  $1/T$ , the barrier height can be calculated from the slope. This plot for a W-GaAs Schottky barrier is shown in Fig. IV-19. The barrier height calculated was 0.756 eV, giving a calculated Richardson constant of  $15.2 \text{ A/cm}^2\text{-K}^2$ .

The calculated I-V barrier heights of the W-GaAs Schottky barriers for all of the epitaxial layers using the calculated Richardson constant are plotted in Fig. IV-20. The explanation of the dashed curves in Fig. IV-20 is identical with that for the dashed curves in Fig. IV-18. Also, the barrier is expected to be lower for heavier doped n-type GaAs, but the lower resistivity tungsten film yields higher barriers, consistent with the ideality factor measurements of Fig. IV-18.

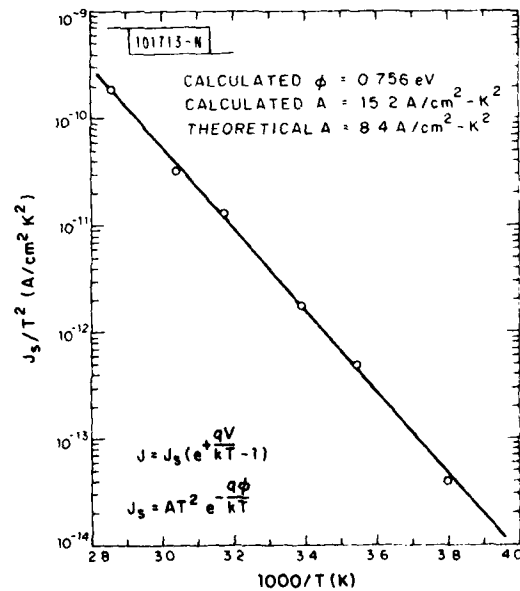


Fig. IV-19. Calculation of  $\phi$  and  $A$  from I-V-T measurements.

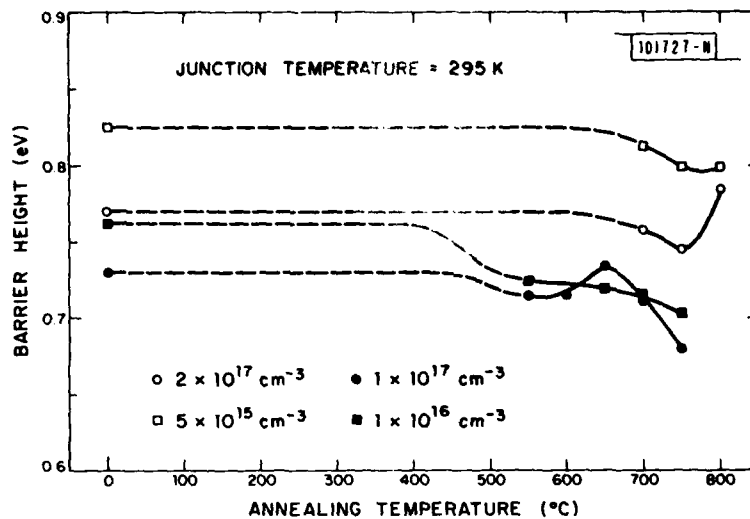


Fig. IV-20. I-V barrier heights of W-GaAs diodes for various annealing temperatures.

Thus we expect that higher quality tungsten will produce a better Schottky barrier. These barrier heights are comparable with the barrier heights obtained for Ti-W Schottky barriers,<sup>18</sup> and they are greater than any other metal on GaAs annealed at these temperatures.<sup>19</sup>

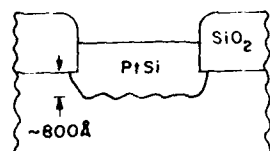
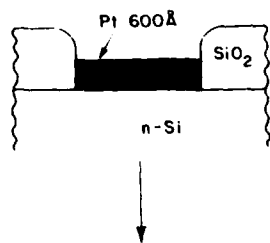
K. B. Nichols  
C. O. Bozler

#### F. SHALLOW PtSi-Si SCHOTTKY-BARRIER CONTACTS FORMED BY A NEW TECHNIQUE

Considerable attention has recently been directed toward the formation of shallow silicide contacts<sup>20</sup> in order to achieve the reduction in device dimensions (both laterally and vertically) required for large-scale integration. Conventionally, PtSi-Si contacts are formed by depositing a Pt film on the Si substrate through openings in a SiO<sub>2</sub> mask, then heating to produce a layer of PtSi by the reaction between the film and the substrate [Fig. IV-21(a)]. The desired thickness of the PtSi layer, typically over 500 Å, determines the thickness of the Pt film used and consequently the depth of the contact, since the thicknesses of PtSi formed and Si consumed are respectively ~1.98 and ~1.32 times the thickness of the Pt film. Here we describe the I-V characteristics of shallow PtSi-Si Schottky-barrier contacts formed by a new technique<sup>21</sup> that permits the contact depth to be selected independently of the thickness of the PtSi layer. In this technique a series of thin alternating layers of Pt and Si are deposited on the Si substrate. Each Si layer is made nominally 1.32 times as thick as the Pt layer above it, so that the depth of the contact formed on heating is determined by the thickness of the first Pt layer, while the thickness of the PtSi layer is determined by the total thickness of all the Pt layers [Fig. IV-21(b)].

Schottky-barrier contacts were formed by both the new and conventional techniques on 3-Ω-cm n-type, (100)Si substrates with 1200-Å-thick, thermal SiO<sub>2</sub> on the front and an n<sup>+</sup> layer on the back for ohmic contact. A multi-hearth evaporation system with a single e-gun was used to deposit Pt and Si layers through 43-mil (~1.1 mm) holes etched in the thermal SiO<sub>2</sub>. To prepare contacts by the new technique, a Pt layer ~150 Å thick and four pairs of alternating Si layers (~132 Å thick) and Pt layers (~100 Å thick) were deposited without breaking the vacuum. For

(a) CONVENTIONAL TECHNIQUE



(b) NEW TECHNIQUE

ALTERNATING Pt-Si LAYERS

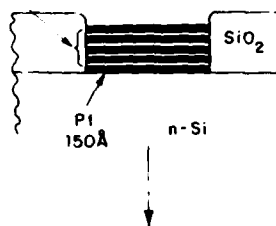
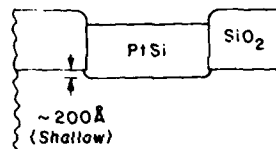
ANNEALING  
500°C, 30 MIN

Fig. IV-21. Schematic diagram showing (a) PtSi-Si Schottky-barrier contact formed by conventional technique and (b) shallow PtSi-Si contact formed by a new technique.

conventional contacts, a single Pt film  $\sim 600 \text{ \AA}$  thick was used. The Pt-Si or Pt layers outside the windows were removed by lift-off techniques, and residual photoresist was removed by cleaning the wafers in an  $\text{O}_2$  plasma. The wafers were heat treated at  $500^\circ\text{C}$  for 30 min. in a purified  $\text{H}_2$  ambient to form the PtSi contacts. Back ohmic contact was made by using Cr/Au metallization.

The depth of the shallow PtSi-Si contacts that have been formed by the new technique is about  $200 \text{ \AA}$ , and the thickness of the PtSi layer is about  $1100 \text{ \AA}$ . For the contacts made by the conventional technique, the depth is about  $800 \text{ \AA}$  and the PtSi thickness is about  $1200 \text{ \AA}$ .

Figure IV-22 shows the I-V characteristics of 5 shallow-contact Schottky-barrier diodes selected randomly from 60 diodes fabricated by the new technique on 1 wafer. The five diodes have identical forward characteristics, which follow the expression  $I_F = I_s \exp(qV/nkT)$  over 5 to 6 orders of magnitude with  $I_s \approx 3 \times 10^{-10} \text{ A}$  and  $n = 1.02$ . The barrier height,  $\phi_B$ , is found to be  $0.87 \text{ eV}$ , in agreement with previous results.<sup>22</sup> The reverse characteristics of the diodes are similar but not completely identical. The reverse current is of the order of  $10 \text{ nA}$  at  $-10 \text{ V}$ . For comparison, the reverse current calculated from thermionic emission theory,<sup>23</sup> including the effect due to image-force lowering, is shown by the dashed curve in Fig. IV-22. The measured values of  $I_R$  are higher than the theoretical ones; the difference is probably due to edge leakage, which generally occurs in planar Schottky diodes without a guard ring. The breakdown voltages measured at  $I_R = 1 \text{ mA}$  are in the range of  $-72$  to  $-75 \text{ V}$ .

The I-V characteristics of five randomly selected diodes fabricated by the conventional technique are shown in Fig. IV-23. The forward characteristics are almost the same as those of the shallow-contact diodes made by the new technique. However, the reverse characteristics of the conventional diodes are considerably worse than those shown in Fig. IV-22. At a given voltage, the values of  $I_R$  are generally about an order of magnitude higher than those of the shallow-contact diodes, and the range of these values is appreciably wider. Furthermore, the breakdown

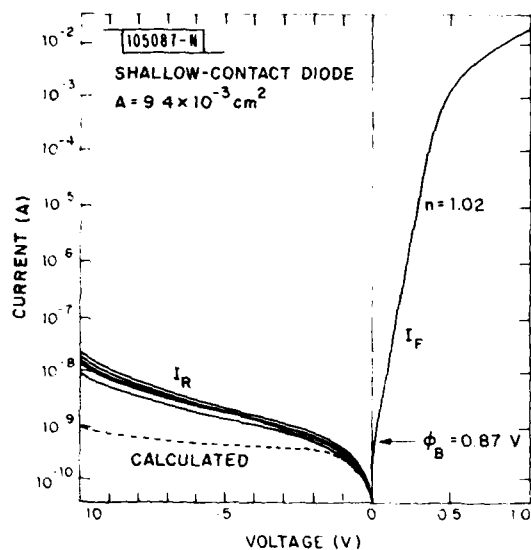


Fig. IV-22. I-V characteristics of shallow-contact Schottky-barrier diodes fabricated by new technique. The dashed curve is the calculated reverse I-V characteristic for ideal Schottky diodes.

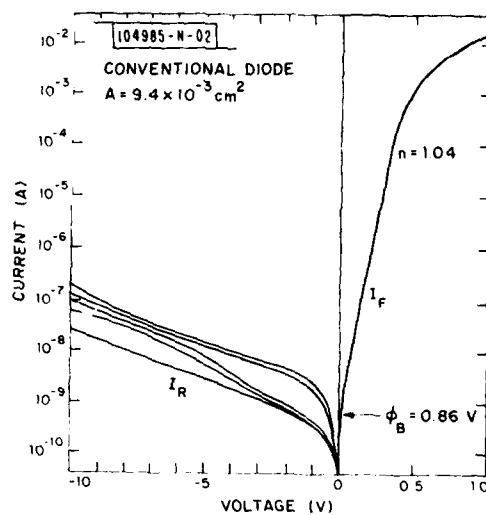


Fig. IV-23. I-V characteristic of Schottky-barrier diodes fabricated by conventional technique.

voltages, which range from  $-30$  to  $-50$  V at  $I_R = 1$  mA, are markedly lower and more scattered than those of the shallow-contact diodes.

The differences observed between the reverse characteristics of the two types of diodes can be attributed to differences in the structure of the PtSi-Si interface. In an earlier investigation<sup>21</sup> it was found by Rutherford backscattering and cross-sectional transmission electron microscopy that this interface is quite smooth for the shallow contacts produced by the new technique but quite irregular for the deeper ones produced by the conventional technique. At sharp points located along such an irregular interface, the decrease in the radius of curvature is expected to cause an increase in the local electric field.<sup>24</sup> The consequent image-force lowering and field-induced (or dipolar-charge) barrier lowering effects<sup>23</sup> will result in increased values of  $I_R$ , and the diodes will also exhibit soft breakdown characteristics. In addition, the variation in these effects due to changes in the details of the interface structure will make the reverse characteristics less reproducible from diode to diode than in the case of the shallow-contact diodes.

B-Y. Tsaur            R. W. Ralston  
D. J. Silversmith    R. W. Mountain

## REFERENCES

1. Solid State Research Report, Lincoln Laboratory, M.I.T. (1979:1), pp. 51-53, DDC AD-A073152/1.
2. Ibid. (1980:1), pp. 32-33, DTIC AD-A089822.
3. Ibid. (1980:3), pp. 40-43, DTIC AD-A094075.
4. Ibid. (1978:4), pp. 38-41, DDC AD-A068563/6.
5. Ibid. (1977:2), pp. 50-53, DDC AD-A044795.
6. Ibid. (1976:2), pp. 47-48, DDC AD-A030861/9.
7. Ibid. (1980:3), pp. 43-44, DTIC AD-A094075.
8. G. C. Messenger, IRE Trans. Microwave Theory Tech MTT-5, 62 (1957).
9. S. Weinreb and A. R. Kerr, IEEE J. Solid-State Circuits SC-8, 58 (1973).
10. D. D. Rathman, D. J. Silversmith, J. A. Burns and C. O. Bozler, Recent News, Paper 699, J. Electrochem. Soc. 127, 501C (1980); Solid State Research Report, Lincoln Laboratory, M.I.T. (1980:3), p. 44-47, DTIC AD-A094075.
11. J. Bloem and L. J. Giling, in Current Topics in Materials Science, Vol. 1, edited by E. Kaldis (North-Holland, New York, 1978), p. 147.
12. A. K. Sinha, T. E. Smith, T. T. Sheng, and N. N. Axelrod, J. Vac. Sci. Technol. 10, 436 (1973).
13. T. T. Sheng, R. B. Marcus, F. Alexander, and W. A. Reed, Thin Solid Films 14, 289 (1972).
14. A. K. Sinha and J. M. Poate, Appl. Phys. Lett. 23, 666 (1973).
15. A. K. Sinha and J. M. Poate, Jap. J. Appl. Phys., Suppl. 2, pt. 1, 841 (1974).
16. A. K. Sinha, Appl. Phys. Lett. 26, 171 (1975).
17. E. H. Rhoderick, Metal-Semiconductor Contacts (Clarendon Press, Oxford, 1978), pp. 78-95.
18. E. Kohn (unpublished).
19. H. J. Hovel and C. Lanza, Device Research Conference, Cornell University, June 1980.
20. K. N. Tu, W. N. Hammer, and J. O. Olowalafe, J. Appl. Phys. 51, 1663 (1980).
21. B-Y. Tsaur, D. J. Silversmith, R. W. Mountain, L. S. Hung, S. S. Lau, and T. T. Sheng, submitted to J. Appl. Phys.
22. M. P. Lepselter and S. M. Sze, Bell Syst. Tech. J. 47, 196 (1967).
23. S. M. Sze, Physics of Semiconductor Devices (Wiley-Interscience, New York, 1969), Chap. 8.
24. S. M. Sze and G. Gibbons, Solid-State Electron. 9, 831 (1966).

## V. ANALOG DEVICE TECHNOLOGY

### A. MNOS/CCD NONVOLATILE ANALOG MEMORY

In this report we describe the design, fabrication, and operation of an MNOS/CCD memory capable of nonvolatile storage of sampled analog data. By extending the signal storage times of existing analog devices by orders of magnitude, this device obviates the need for A/D conversion and digital storage and thus should find numerous applications in analog signal processing devices.

In recent experimental reports,<sup>1</sup> Withers *et al.* have described the writing and retention of analog signals in discrete MNOS capacitors fabricated on n-type silicon. After a reset state was established by majority carrier tunneling, a controlled number of minority carriers was injected into the depletion layer; these carriers tunneled to nitride traps and in turn induced shifts in the flatband voltage proportional to the minority carrier charge. Linear voltage windows of 12 V were observed, and logarithmic decay toward the virgin flatband voltage proceeded at rates as low as 400 mV per decade of storage time over a 9-V window. Analog signals could be stored linearly over a dynamic range of 40 dB for 30 h. Similar results have since been obtained on p-type silicon, and a quantitative theoretical model has been constructed which satisfactorily describes the linear writing process.<sup>2</sup>

By incorporating this linear writing technique in a structure superficially similar to a previous MNOS/CCD binary memory,<sup>3</sup> we have for the first time exploited the analog input/output capabilities of the CCD and the analog nature of MNOS storage to form a fully analog non-volatile memory.

A photomicrograph of the MNOS/CCD memory is shown in Fig. V-1, and a parallel cross section of one cell is illustrated in Fig. V-2. Figure V-3 shows the charge-transfer operations. Analog charge packets are metered into the 32-period, 4-phase surface-n-channel CCD by the potential equilibration technique.<sup>4</sup> The nitride traps of the memory sites have been previously reset by majority carrier tunneling (Fig. V-3, top), and the subsequent application of the write voltage to the memory gate deep-depletes the underlying silicon. The CCD clocks are stopped with the 32 input samples in the  $\phi 1$  wells, and a parallel transfer is made to the MNOS memory sites, adjacent to the  $\phi 1$  wells (Fig. V-3, middle). Self-induced tunneling of the minority carrier packets then ensues as described in Reference 1.

In order to read the stored samples, the holding wells adjacent to the memory sites are first filled with charge from the parallel diffusion. With appropriate bias on the memory gate, a portion of each holding-well charge packet spills over the corresponding memory site into the previously emptied CCD  $\phi 1$  well (Fig. V-3, bottom). These charge packets now in the  $\phi 1$  wells reflect the threshold voltages of the memory sites and are clocked serially out of the CCD channel. The output structure is a floating diffusion with on-chip reset and electrometer MOSFETs; these are operated as a gated integrator<sup>5</sup> and are used with an external correlated double-sampling circuit.<sup>6</sup>

Device fabrication utilizes a LOCOS process for self-aligned channel stops. A dual-dielectric gate structure (700 Å  $\text{SiO}_2$ /600 Å  $\text{Si}_3\text{N}_4$ ) is used for the CCD (illustrated in Fig. V-4) and the MOSFETs, and a thermally processed 25-Å  $\text{SiO}_2$ /600-Å LPCVD  $\text{Si}_3\text{N}_4$  gate is used for the memory sites. Double-level metallization (doped poly-Si and aluminum) is used to form alternated CCD gates and the memory read/write structure. The processing sequence utilizes eight mask steps.

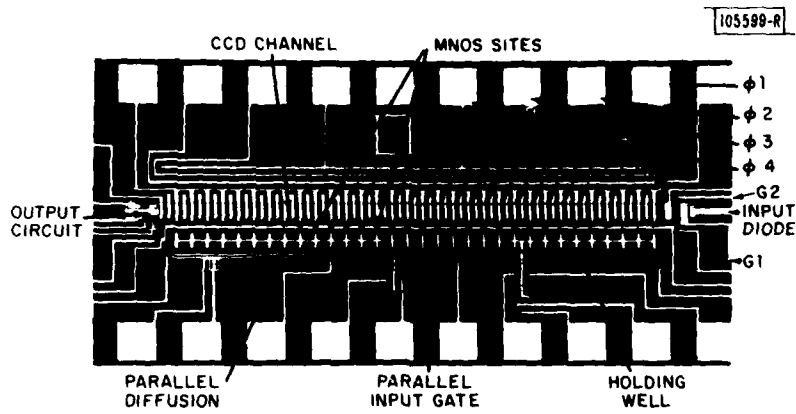


Fig. V-1. Photomicrograph of the MNOS/CCD analog memory.

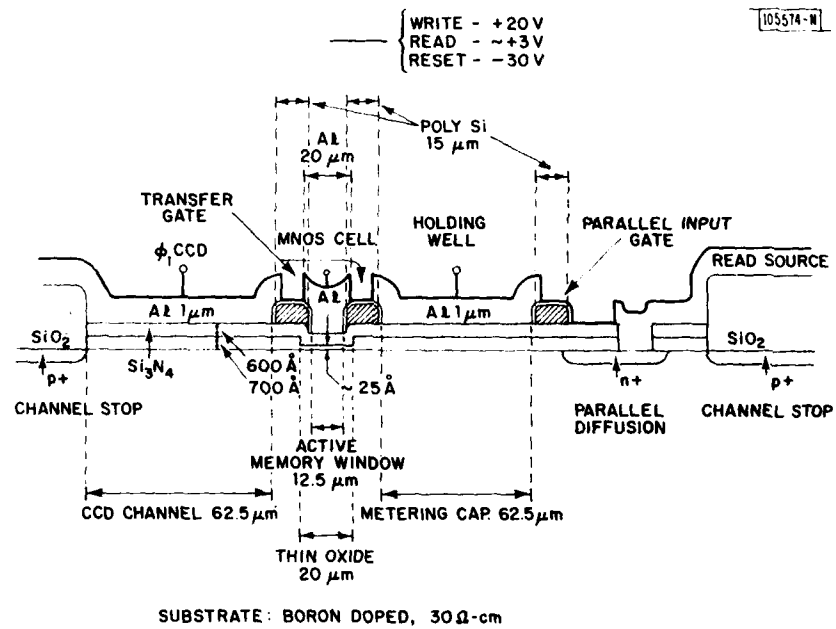


Fig. V-2. Cross section of one memory cell through the CCD  $\phi 1$  well, MNOS memory site, and holding well.

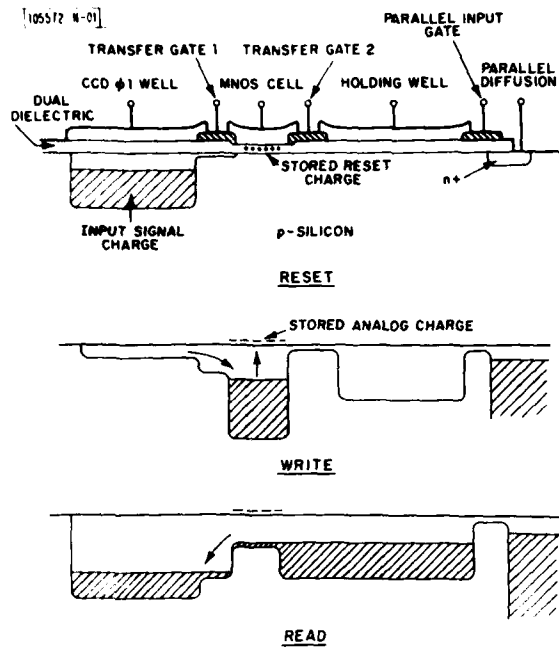


Fig. V-3. Charge-transfer operations of the MNOS/CCD showing one cross section through a memory site and the adjacent CCD  $\phi_1$  well. Upper cross section: State of the memory after the reset and with the 32 input samples in the CCD  $\phi_1$  wells. Center cross section: With the write voltage applied to the memory gate and the first transfer gate opened, the input signal charge spills into the memory site. Self-induced tunneling ensues. Lower cross section: The holding wells have been uniformly filled from the parallel diffusion. With the memory gate biased to the read voltage and the second transfer gate opened, an amount of charge flows into the CCD  $\phi_1$  well which reflects the amount of charge trapped in the nitride. These output samples are clocked out serially.

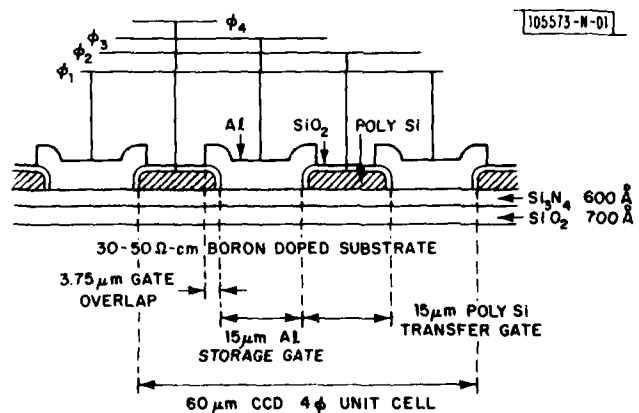


Fig. V-4. Cross section through the serial CCD channel.

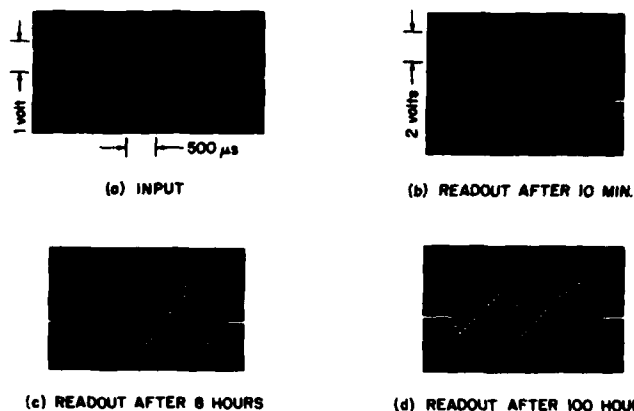


Fig. V-5. Performance of the analog memory in storing an asymmetric triangular wave. Sampling interval is  $80 \mu\text{s}$  for both input and output. (a) Input to second input gate; 1 V/division. (b) Nondestructive readout of stored samples 10 min. after writing; 2 V/division. Readouts are made continuously at 3-ms intervals. (c) Readout after 8 h; 2 V/division. (d) Readout after 100 h; 2 V/division.

Results obtained from the first batch of wafers indicate that nonvolatile analog memory is indeed feasible. Serial operation of the CCD demonstrates linear throughput over a range of greater than 6 V at the output node and a charge transfer inefficiency of  $\epsilon = 1.1 \times 10^{-4}$  with a 14-percent fat zero. Operation of the nonvolatile memory is exhibited in Fig. V-5. An asymmetric triangle [Fig. V-5(a)] is applied to the CCD second input gate<sup>4</sup> and sampled at an  $80\text{-}\mu\text{s}$  rate. The 32 samples are transferred to the MNOS sites and stored by, in this example, a +25-V, 5-ms write pulse. Interrogation is commenced immediately and repeated every 3 ms. Figure V-5(b) shows the (approximately)  $2 \times 10^5$ th readout, 10 min. after writing. Subsequent readouts at 8 h and 100 h are also shown.

The linear nature of the writing process is evident; it is also clear that, although the stored waveform has in 100 h decayed to 60 percent of its initial (10-s) amplitude, linearity has not been affected.

The largest source of error in the readout is fixed-pattern noise. The zero-to-peak rms deviation from linearity is 35 mV, indicating a linear dynamic range approaching 33 dB in this example.

The analog MNOS/CCD memory is not competitive with digital arrays for bulk data storage. This new technology should, however, find numerous applications when integrated with devices for which A/D conversion is cumbersome, such as CCD and SAW/CCD analog signal processors. Currently envisioned is an analog/analog correlator using the MNOS sites for direct storage of the reference signal.

R. S. Withers  
D. J. Silversmith  
R. W. Mountain

## B. HIGH-PERFORMANCE ELASTIC CONVOLVER WITH PARABOLIC HORNS

In this report details are presented on the design and performance of an improved version of the elastic convolver described by Becker and Hurlburt in an earlier report.<sup>7</sup> The important

features to be described are (1) the use of parabolically tapered horns to compress the SAW beamwidth to a single-symmetrical-mode waveguide in order to achieve smooth frequency response (less than  $\pm 0.5$  dB ripple), (2) the use of a dual-track convolver structure to achieve greater than 45 dB self-convolution suppression, and (3) the use of thin metallization (50 Å chromium and 500 Å aluminum) on the horn and waveguide regions to provide low ( $\pm 35^\circ$ ) phase distortion.

### 1. Parabolic Horns

Parabolically tapered horns have been used in integrated optical devices to couple the light from planar optical waveguides (wide aperture) to channel waveguides (narrow aperture) and vice versa.<sup>8,9</sup> A similar horn design can be used in the elastic convolver for the beamwidth compression of SAWs.<sup>7</sup> The two basic requirements of this acoustic horn are to provide a low-loss transition (i.e., the lowest order local normal mode of the horn must propagate through the structure without cumulative power transfer to higher order local normal modes) and to introduce no excessive ripple for wideband operation. If a constant taper is employed, i.e., the linearly tapered horn, the mode coupling problem will be more severe at the wider portion because the propagation constants  $\beta_i$  of the local normal modes are more closely spaced, and as a consequence a horn with sufficiently gradual taper for low mode coupling is longer than necessary. The criterion employed in our horn design is to maintain a constant but small coupling between the fundamental and second symmetrical modes over the entire structure based on the coupled-mode theory, and this results in a horn of minimum length with approximately parabolic shape. It can be shown that this criterion is approximated by maintaining a constant ratio  $\alpha$  between the horn taper angle and the diffraction spreading of the fundamental mode which would occur if the waveguide ended. An analogous interpretation is that the horn taper angle should be proportional to the ray angle of the fundamental mode by a factor  $\alpha$ . For values of  $\alpha \leq 1$ , energy transfer from the fundamental mode to the second symmetrical mode is restricted to below -26 dB. If the ray optics interpretation is employed, the horn design rule can be easily formulated as

$$\frac{dW}{dL} = \frac{2\alpha\kappa_0}{\eta_s\beta_0}$$

where

W is the width of horn,

L is the length of horn,

$\alpha$  is the proportionality factor, typically less than or equal to 1,

$\eta_s$  is the anisotropy factor of SAW propagating on Y-cut LiNbO<sub>3</sub> with shorted surface,

$\beta_0$  is the propagation constant of the fundamental mode,

$\kappa_0 = \eta_s (K_s^2 - \beta_0^2)^{1/2}$ , is the transverse wave number of the fundamental mode, and

$K_s$  is the wavenumber of the planar SAW on YZ-LiNbO<sub>3</sub> with shorted surface.

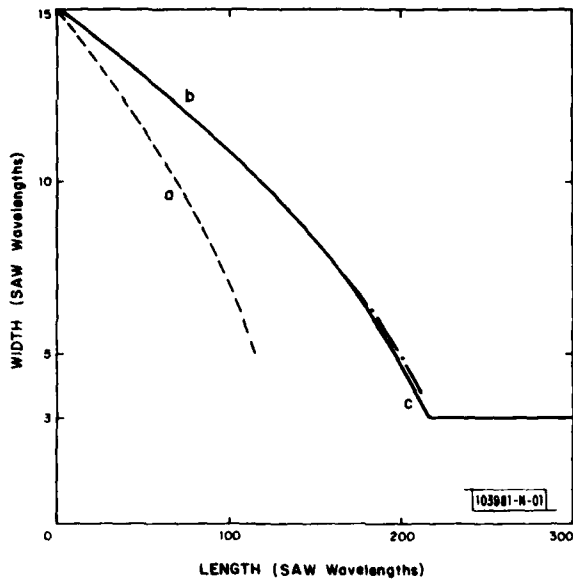


Fig. V-6. Theoretical design curves of parabolic-tapered horns for beamwidth compression on YZ-LiNbO<sub>3</sub>: (a) isotropic, coupled-mode theory; (b) anisotropic, coupled-mode theory; (c) anisotropic, ray optics approximation.

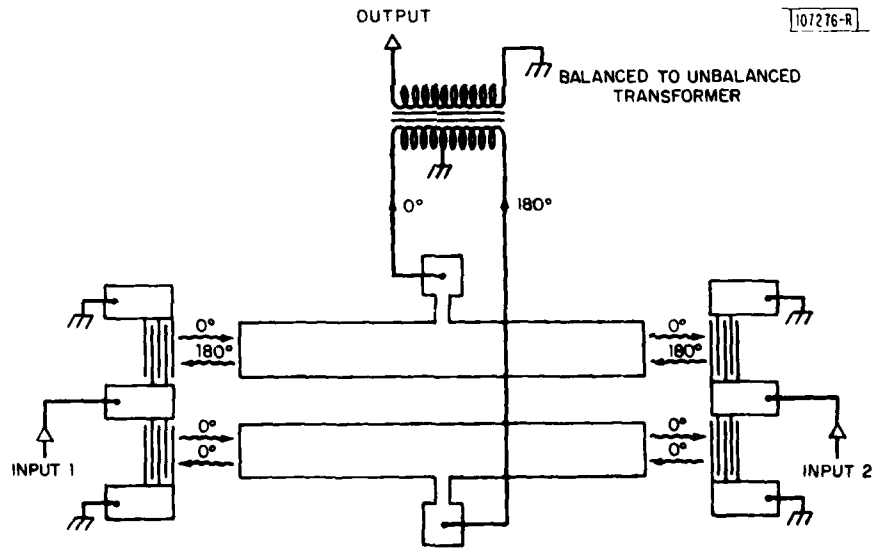


Fig. V-7. Schematic diagram of the dual-track convolver structure for self-convolution suppression.

Notice that the anisotropy of the SAW propagating on Y-cut  $\text{LiNbO}_3$  is included in Eq. (V-1) with a parabolic approximation for the anisotropy.<sup>10</sup> Figure V-6 shows the theoretical design curves of the horn, width vs length, on YZ- $\text{LiNbO}_3$  for the cases of (a) coupled-mode theory with isotropic approximation, (b) coupled-mode theory with parabolically approximated anisotropy, and (c) ray optics approximation [Eq. (V-1)] with parabolically approximated anisotropy. Both the horn width and length in these curves are normalized against the SAW wavelength and all three curves are plotted for  $\alpha = 1$ . Note that the effect of anisotropy is very important, as it produces the large discrepancy between curves (a) and (b), while the ray optics approximation described by Eq. (V-1) [curve (c)], which we actually employed in our design, matches very well with the more exact coupled-mode theory derivation [curve (b)].

It is also important to point out that because of the nearly parabolic horn shape, the horn length for cases of interest is essentially determined by its input aperture; for example, halving the original input aperture reduces the required length of horn by about a factor of 4. As will become clear in the following discussion, the use of a dual-track convolver for self-convolution suppression has the side benefit of allowing smaller apertures and thus substantially shorter horns.

## 2. Self-Convolution Suppression

Self-convolution due to the reflection of the SAW by the opposite transducer is the major output spurious signal existing in the convolver. In order to fully utilize the processing gain provided by the convolver under any circumstances, the self-convolution level should be suppressed by a factor greater than the device time-bandwidth product. Among the numerous solutions to this problem, the scheme shown schematically in Fig. V-7, employing a dual-track convolver structure with a pair of electrically orthogonal transducers, is found to be most satisfactory because of its simplicity and wide-bandwidth capability. Morgan *et al.* of the University of Edinburgh independently proposed the same scheme in 1972.<sup>11</sup> The principle of this self-convolution suppression can be simply described as follows: the SAWs excited by transducer No. 1 are in phase (symmetrical) in the two-track convolver, while the SAWs excited by transducer No. 2 are  $180^\circ$  out of phase (antisymmetrical), such that the two convolver outputs are  $180^\circ$  out of phase and can be combined by taking the difference between the two tracks with a balanced-to-unbalanced transformer. When the SAWs with symmetrical wavefronts excited by transducer No. 1 reach transducer No. 2, transducer No. 2 will not receive nor regeneratively reflect any power because of the antisymmetrical nature of the polarity arrangement of the electrodes. Similarly, the wavefronts excited by transducer No. 2 are orthogonal to, and decoupled from, transducer No. 1.

## 3. Phase Distortion

Phase distortion of an elastic convolver is mainly due to the SAW propagation dispersion, which in turn can arise from material dispersion (i.e., mass loading) and/or geometrical waveguide dispersion (i.e., electrical loading). Because these two factors normally introduce dispersion of opposite signs, it is possible to have them compensate one another by a proper combination of waveguide width and metal thickness.

## 4. Elastic Convolver Performance

The current design of the elastic convolver based on the principles described in previous sections is shown schematically in Fig. V-8. It employs a dual-track structure with a pair of

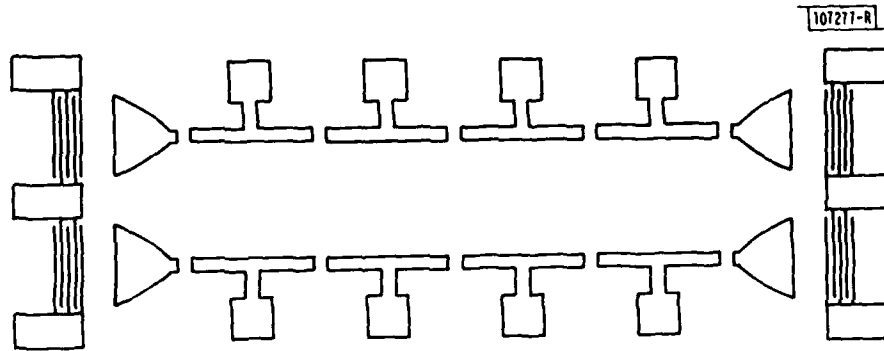


Fig. V-8. Schematic diagram of the 4-ary dual-track elastic convolver with parabolic beamwidth compressor.

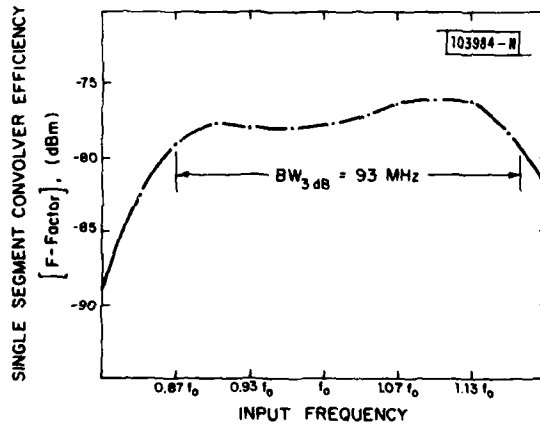


Fig. V-9. Single-section-output frequency response of the 4-ary dual-track elastic convolver.

orthogonal transducers, a combination which results in self-convolution levels more than 45 dB below the main output. The device has a time-bandwidth product of 930. The combined aperture of the dual transducer is 33 wavelengths and the waveguides are 3 wavelengths wide. Each parabolic-horn beamwidth compressor is  $\sim 1 \mu\text{s}$  in length with a compression ratio of 5.5. The metallization used both in horn and waveguide regions is 50-Å Cr/500-Å Al. The outputs are segmented into four center-tapped sections. These four sections are connected through a series of balanced-to-unbalanced transformers and hybrids for the purpose of decoding the 4-ary signals. This coding scheme is a generalization of the more familiar 2-ary or differential-phase-shifted-keyed (DPSK) signaling.

The convolution efficiency across the frequency band of a single segment is plotted in Fig. V-9. As is common, the efficiency is given as an F-factor, defined as  $F = 10 \log (P_{\text{out}}/P_1 P_2)$ , where  $P_1$  and  $P_2$  are the input powers and  $P_{\text{out}}$  is the output power level. An F-factor of -78 dBm for a single segment is observed, and an F-factor of -74 dBm from four combined outputs can be expected provided the combining circuitry introduces no more than 2-dB insertion loss. Note that there are no noticeable ripples in the output frequency response, hence no substantial mode competition is occurring in the SAW waveguide structure.

Figure V-10 shows the interaction uniformity of one output section and of all the four output sections combined. The amplitude fluctuates by less than  $\pm 0.5$  dB except for the dip at the center. This notch is due to capacitive loading of the output by the bond pad of each center tap.

Plotted in Fig. V-11 is the self-convolution suppression vs input frequency. The device shows a suppression of greater than 45 dB over the entire passband.

Phase deviation from linear of the convolver is plotted in Fig. V-12, and a phase distortion of less than  $\pm 35^\circ$  is observed. In a system which uses minimum-shifted-keying (MSK) waveforms, phase distortion of this magnitude causes only 0.5 dB in implementation loss and is acceptable for most system applications. Device characteristics are summarized in Table V-1.

## 5. Summary

Design principles for an elastic convolver incorporating a parabolic-horn beamwidth compressor and a dual-track self-convolution-suppression technique have been presented. This design procedure was employed to produce a high performance 4-ary elastic convolver with a time-bandwidth product of 930. The device demonstrates a dynamic range greater than 60 dB (for 23 dBm input powers), self-convolution suppression exceeding 45 dB and acceptably low phase distortion.

I. Yao

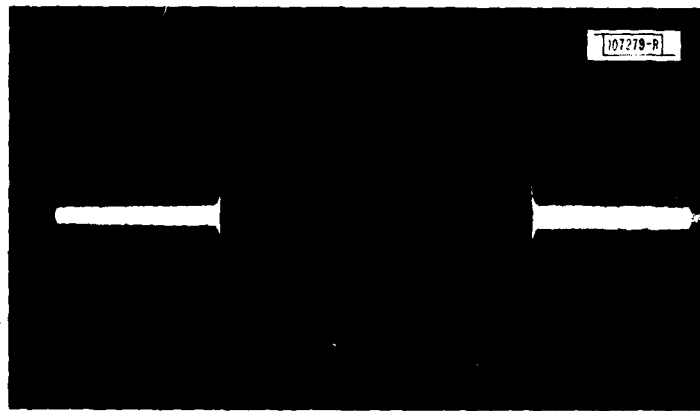
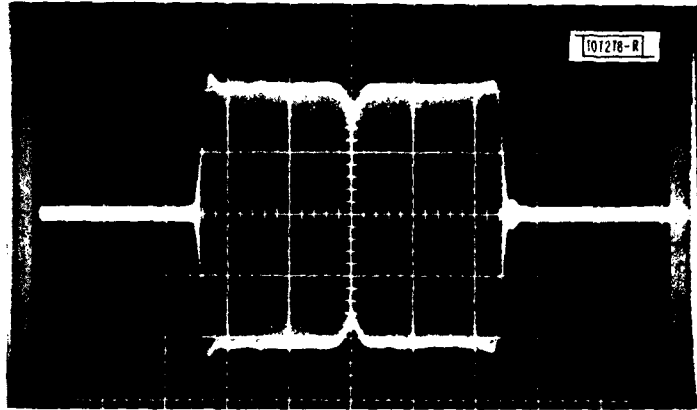


Fig. V-10. Interaction uniformity of the dual-track elastic convolver:  
(a) single section, (b) four sections combined.

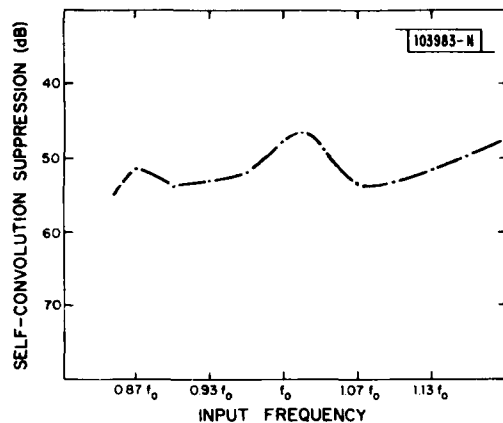


Fig. V-11. Self-convolution suppression of the 4-ary dual-track elastic convolver.

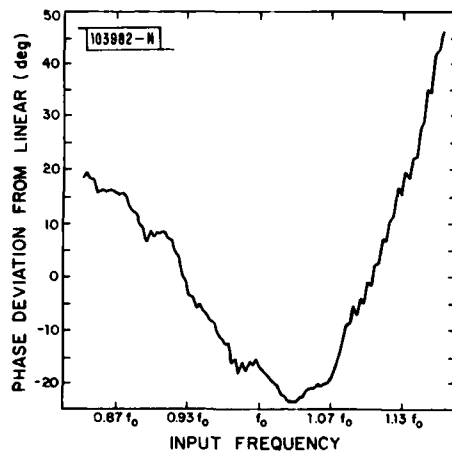


Fig. V-12. Single-section-output phase distortion of the 4-ary dual-track elastic convolver.

TABLE V-1 CHARACTERISTICS OF DUAL-TRACK ELASTIC CONVOLVER	
Time-Bandwidth Product	930
F-Factor	
Single Segment	-78 dBm
Sum	-74 dBm (expected)
Interaction Uniformity	$\pm 0.5$ dB
Maximum Output Power <sup>1</sup>	-28 dBm
Dynamic Range <sup>2</sup>	63 dB
Self-Convolution Suppression	>46 dB
Phase Distortion	$\pm 35^\circ$
1. With maximum input powers at +23 dBm	
2. Above thermal noise floor	

#### REFERENCES

1. R.S. Withers, R. W. Ralston, and E. Stern, "Nonvolatile Analog Memory in MNOS Capacitors," IEEE Electron Device Letters EDL-1, 42 (1980); [Solid State Research Report, Lincoln Laboratory, M.I.T. (1979:2), pp. 70-76, DDC AD-A078676/4].
2. R.S. Withers, R. W. Ralston, and E. Stern, "Analog Memory in MNOS Devices: Model and Experiments," 1980 Device Research Conference, Ithaca, New York, June 1980; [Solid State Research Report, Lincoln Laboratory, M.I.T. (1980:3), pp. 49-53, DTIC AD-A094075].
3. M. H. White, D. R. Lampe, J. L. Fagan, F. J. Kub, and D. A. Barth, "A Nonvolatile Charge-Addressed Memory (NOVCAM) Cell," IEEE J. Solid-State Circuits SC-10, 281 (1975).
4. C. H. Sequin and A. M. Mohsen, "Linearity of Electrical Charge Injection Into Charge Coupled Devices," IEEE J. Solid-State Circuits SC-10, 81 (1975).
5. W. F. Kosonocky and J. E. Carnes, "Two Phase Charge Coupled Devices with Overlapping Polysilicon and Aluminum Gates," RCA Review 34, 164 (1973).
6. M. H. White, D. R. Lampe, F. C. Blaha, and I. A. Mack, "Characterization of Surface Channel CCD Image Arrays at Low Light Levels," IEEE J. Solid-State Circuits SC-9, 1 (1974).
7. R. A. Becker and D. H. Hurlburt, "Wideband LiNbO<sub>3</sub> Elastic Convolver with Parabolic Horns," 1979 Ultrasonics Symposium Proceedings, (New York, IEEE, 1979), pp. 729-731; [Solid State Research Report, Lincoln Laboratory, M.I.T. (1979:4), pp. 73-74, DDC AD-A084271/6].
8. W. K. Burns, A. F. Milton, and A. B. Lee, "Optical Waveguide Parabolic Coupling Horns," Appl. Phys. Lett. 30, 29 (1977).
9. A. F. Milton and W. K. Burns, "Mode Coupling in Optical Waveguide Horns," IEEE J. Quantum Electron. QE-13, 828 (1977).
10. P. Defranould and C. Maerfeld, "A SAW Planar Piezoelectric Convolver," Proc. IEEE 64, 748 (1976).
11. D. P. Morgan, private communication.

UNCLASSIFIED

SECURITY CLASSIFICATION OF THIS PAGE (When Data Entered)

REPORT DOCUMENTATION PAGE		READ INSTRUCTIONS BEFORE COMPLETING FORM
1. REPORT NUMBER ESD-TR-81-7	2. GOVT ACCESSION NO. <i>AD-A103 887</i>	3. RECIPIENT'S CATALOG NUMBER
4. TITLE (and Subtitle)  Solid State Research  <i>TNGY</i>		5. TYPE OF REPORT & PERIOD COVERED Quarterly Technical Summary 1 November - 31 January 1981
		6. PERFORMING ORG. REPORT NUMBER <i>TR 1981:1</i>
7. AUTHOR(s)  Alan L. McWhorter		8. CONTRACT OR GRANT NUMBER(s)  F19628-80-C-0002 ✓
9. PERFORMING ORGANIZATION NAME AND ADDRESS Lincoln Laboratory, M.I.T. P.O. Box 73 Lexington, MA 02173		10. PROGRAM ELEMENT, PROJECT, TASK AREA & WORK UNIT NUMBERS  Program Element No. 63250F Project No. 649L
11. CONTROLLING OFFICE NAME AND ADDRESS Air Force Systems Command, USAF Andrews AFB Washington, DC 20331		12. REPORT DATE 15 February 1981
14. MONITORING AGENCY NAME & ADDRESS (if different from Controlling Office)  Electronic Systems Division Hanscom AFB Bedford, MA 01731		13. NUMBER OF PAGES 84
		15. SECURITY CLASS. (of this report)  Unclassified
16. DISTRIBUTION STATEMENT (of this Report)  Approved for public release; distribution unlimited.		15a. DECLASSIFICATION DOWNGRADING SCHEDULE
17. DISTRIBUTION STATEMENT (of the abstract entered in Block 20, if different from Report)		
18. SUPPLEMENTARY NOTES  None		
19. KEY WORDS (Continue on reverse side if necessary and identify by block number)		
solid state devices	photodiode devices	infrared imaging
quantum electronics	lasers	surface-wave transducers
materials research	laser spectroscopy	charge-coupled devices
microelectronics	imaging arrays	acoustoelectric devices
analog device technology	signal processing	
20. ABSTRACT (Continue on reverse side if necessary and identify by block number)		
<p>This report covers in detail the solid state research work of the Solid State Division at Lincoln Laboratory for the period 1 November 1980 through 31 January 1981. The topics covered are Solid State Device Research, Quantum Electronics, Materials Research, Microelectronics, and Analog Device Technology. Funding is primarily provided by the Air Force, with additional support provided by the Army, DARPA, Navy, NASA, NSF, and DOE.</p>		

DD FORM 1473 EDITION OF 1 NOV 65 IS OBSOLETE  
1 JAN 73

UNCLASSIFIED

SECURITY CLASSIFICATION OF THIS PAGE (When Data Entered)